Diffraction Management by using Coherent Control Fields in Optical Media

A thesis

by

Onkar Nath Verma

Submitted in partial fulfillment of the requirements

for the award of the degree of

Doctor of Philosophy

Department of Physics
Indian Institute of Technology Guwahati
Guwahati 781039, India

October 2014

Diffraction Management by using Coherent Control Fields in Optical Media

Onkar Nath Verma

A thesis
submitted for the degree of
Doctor of Philosophy

Supervisor:
Dr. Tarak Nath Dey

Department of Physics
Indian Institute of Technology Guwahati
Guwahati 781039, India

October 2014

Declaration

The work contained in the thesis entitled "*Diffraction management by using coherent control fields in optical media*" has been carried out by me under the supervision of Dr. Tarak Nath Dey at Department of Physics, Indian Institute of Technology Guwahati. This work has not been submitted elsewhere for the award of any degree.

(Onkar Nath Verma) Date:
Roll No: 09612130
Department of Physics
Indian Institute of Technology Guwahati
Guwahati - 781039
Assam, India.

Certificate

This is to certify that the work contained in the thesis entitled "*Diffraction management by using coherent control fields in optical media*" submitted by Mr. Onkar Nath Verma in the partial fulfillment of the requirement for the award of the degree of Doctor of Philosophy in Department of Physics, Indian Institute of Technology Guwahati, is a record of the candidate's own work carried out by him under my supervision and guidance. The matter embodied in this report has not been submitted in part or full to any other university or institute for the award of any degree.

Dr. Tarak Nath Dey
Associate Professor
Department of Physics
Indian Institute of Technology Guwahati
Guwahati - 781039
Assam, India.

Date:

Dedicated

to

my family

Acknowledgements

First and foremost, I would like to thank my thesis supervisor, ***Dr. Tarak Nath Dey****, for his active and patient guidance throughout my research period. I deeply influenced by his immense knowledge, enthusiasm and hard work towards science and research. I must offer my profound gratitude to him for his generosity to accept me as his pupil. In early of my research period, he has guided me through a crisis of confidence when I felt that I had nothing to contribute. Starting right from the research proposal in the beginning of my Ph.D. till the process of writing thesis, his guidance and motivational help brought me a higher level of thinking and led me to finish my thesis step by step successfully. We started many rounds of discussion on various topics which helped me to improve my basics of Quantum Optics and an improvement of thesis work as well. He always managed to supervise me with a smile and guided me towards the correct path. We shared a great understanding. I am blessed and deeply honored to join him as his first Ph.D. student.*

I sincerely acknowledge my doctoral committee members, Dr. Amarendra K. Sarma, Dr. Dilip Pal and Dr. Lal Mohan Kundu for their consistent support and invaluable advice during my review seminars. They contributed much discussion in the new methods and formulation of problems associated with my research work throughout which no doubt, improved the quality of research work. Moreover, I am thankful to doctoral committee chairman, Dr. Amarendra K. Sarma who helped me through the crucial stages of my journey and mentored me with his specific depth of knowledge. I thank him for allowing me to audit his elaborated course on Quantum Optics which helped me to make my research work quite smooth.

I take immense pleasure to express my sincere and deep sense of gratitude to former and present Department Heads Physics for providing an appropriate working environment and remarkable numerical facilities. I extend lot many thanks to all the faculty members of the Department who supported me in several ways during my research tenure. Various comparative courses and computational techniques taught by them during my course work helped me to pursue my research work smoothly. I want to make a special mention of Mr. Basab Purakayasthya along with all staff members of the department for their professional support.

I take this opportunity to sincerely acknowledge the "Ministry of Human Resource Development" (MHRD), Government of India, for providing financial assistance in the form of Research Fellowship which supported me to perform my research work comfortably.

The research in my dissertation could not have been done without assistance and support of many people. I am indebted to all my friends for providing a stimulating and fun filled environment. I extend my thanks to all my seniors for their valuable suggestions from their research experiences. A very special thanks to all my lab-mates for the great moments we have shared starting from chatting to fruitful discussions. My thanks go in particular to Mr. Sandeep Sharma for his support during the course of my work. I admire his distinguished helping nature.

Its my fortune to gratefully acknowledge my beloved friend Nisha (would-be Dr. Nisha Shankhwar). She deserves a special mention here for her unconditional support and generous care during the inevitable ups and downs. She has been a great friend who is unbelievably understanding and very cooperative. I am always grateful to her for creating a pleasant atmosphere during the hard times. I would also like to acknowledge her wonderful family, whom love and support motivated me to remain focused towards achieving various milestones of my journey. Her friendship is one of the most precious gifts I got in my life. I doubt that I will ever be able to convey my appreciation fully, but I owe her my eternal gratitude.

I owe my deepest gratitude towards my parents, my mother Smt. Kanti Verma and father Shri Jiya Lal Verma who dreamed me to be at this place and put all their efforts to make this dream true. Their true love and support has always been my strength. Their extreme hard work in the field of agriculture has been a great inspiration for my life. I am grateful to them for allowing me to pursue my Ph.D, and to dedicate the rest of my life in the cultivation of the science. I take this moment to express my never ending love and respect towards my brother Mr. Pawan Verma and sister-in-law Mrs. Suman Verma for their blessings. I express my love and affection to their lovely children Raj and Pallavi. Their presence makes me to see colorful perspective of life. I thank to my younger brother Samar Verma for all those friendly and cheerful moments, we shared together.

At this moment of accomplishment, I pay homage to my elder brother, Late. Mr. Hiralal Verma. His unflinching courage and conviction will always inspire me. I wish his soul rests in peace.

I wish and pray for the blessings of my grandparents who, had always been my guiding star throughout the journey of my life. My whole effort of this research work is a tribute to my grand parents.

Above all, I praise God, the almighty, merciful and passionate, for providing me this opportunity and granting me the capability to proceed successfully. I remain thankful to almighty for the mental strength given me to face the adverse situations.

I dedicate this page to everybody who was important to the successful realization of this thesis.

Onkar Nath Verma

Abstract

Optical diffraction of laser beam from finite size of conventional optical devices imposes a fundamental limitation for the creation and detection of subwavelength images. Such optical systems can not focus laser beam onto an area smaller than about a square of the wavelength. In this thesis, we utilize different quantum interference effects to control the diffraction and overcome the diffraction-limit. The quantum interference phenomena include coherent population trapping (CPT), electromagnetically induced transparency (EIT), double dark resonances (DDR) and active Raman gain (ARG).

The quantum optical phenomena result in dramatic modification of the absorptive and dispersive properties of an atomic vapor. We exploit these strongly modified optical properties of coherent media to control the diffraction via spatially dependent coherent fields. The spatial modulation in the dispersion is used to write a waveguide (antiwaveguide) by using a laser beam for confining or focusing (defocusing) of another laser beam in an atomic vapor. Also by suitably tailoring the absorption (or gain) and dispersion of the medium along the transverse direction, we predict a possibility of transferring the diffraction-limited information from one light wave to another light wave beyond the diffraction-limit.

Based on CPT and EIT in a three-level atomic system, we study the possibility of cloning of arbitrary images encoded in the spatial profile of a control beam onto a probe beam. We consider both weak probe field and probe field with strength comparable to the control field, and discuss the differences of beam propagation in the weak and strong field limits. Interestingly, we find that feature size of cloned probe field is reduced by a factor of two as compared to that of the original control field structure.

Further, we use quantum interference effects induced by DDR in a four-level atomic system to improve the resolution of the cloned images. A high contrast atomic waveguide structure is formed inside the medium by using three coherent fields and an incoherent pump field. This waveguide enables us to imprint the Rayleigh- or Sparrow-limited control field images to a probe field with high resolution. We find that the feature size of the cloned image is four times smaller than the initial characteristic size of the control image. We also discuss that in the absence of incoherent pump field, the microwave field which connects the lower level metastable states of a four-level system can switch on/off the probe beam propagation inside the medium .

Next, we propose an all-optical antiwaveguide mechanism for diffraction-free steering, splitting, and cloning of an optical beam. We use a spatially inhomogeneous pump beam to create an antiwaveguide structure in a Doppler broadened *N*-type four-level Raman gain medium for a copropagating weak probe beam. We find that an additional control field permits the propagation of probe beam through an otherwise gain medium without diffraction and instability. We also establish that an arbitrary image imprinted initially on pump beam can be cloned onto the transmission profile of the probe beam. Moreover, the resolution of cloned image is increased twice as compared to the initial resolution of pump image.

Preface

The present thesis work deals with control of laser beam diffraction by using coherent control fields in optical media. Our study shows an efficient transfer of any arbitrary information imprinted on the envelope of a laser beam to another copropagating laser beam beyond the diffraction-limit. The spatially dependent coherent fields are used to engineer the optical properties of coherent media in order to control the diffraction and surpass the diffraction-limit. The following chapters will be included in this thesis:

Chapter 1 reviews a full treatment of semiclassical theory of light-matter interaction. We begin with derivation of atomic Hamiltonian under electric dipole approximation. We next derive an effective Hamiltonian for a two-level and three-level atom separately under rotating wave approximation (RWA). We then obtain an expression for linear and nonlinear responses of a two-level and three-level atomic medium. These atomic responses have been used to describe their optical properties in terms of absorption and dispersion. Next, we proceed by deriving a self-consistent theory of the optical response of atomic medium by writing Maxwell's equations in an atomic medium. Further, Maxwell's wave equation has been reduced to paraxial wave equation in medium as well as in free-space. This chapter will end with a discussion on free-space standard solutions of paraxial Helmholtz equation.

Chapter 2 discusses how an arbitrary image encoded in the spatial profile of a control beam is mapped onto a probe beam with increased resolution. We have utilized the phenomena of electromagnetically induced transparency (EIT) and coherent population trapping (CPT) in three-level Λ-system to achieve the goal. We focus on two field intensity regimes of probe field. In one regime, the probe field is weaker than control field. On the other regime, both fields have comparable strength. Thus, we include the effect of linear as well as nonlinear response of the medium on the propagation dynamics for both probe and control fields.

Chapter 3 introduces a scheme for improvement of spatial resolution of a Rayleigh- or Sparrow-limited images. We have explored the sharp spectral features based on quantum interference effects induced by double dark resonances (DDR) in a four-level atomic system. The focus of this chapter is how resolution can be improved by several factors relative to an EIT system in the vicinity of these sharp features. We show that the application of an incoherent pump can give rise to high contrast spatial features of diffraction-limited images.

Chapter 4 describes an all-optical antiwaveguiding effects in a Doppler broadened active Raman gain (ARG) medium composed of N-type four-level ^{87}Rb atoms. We have utilized antiwaveguide mechanism to show beam steering, splitting, and cloning of an optical beam beyond the diffraction-limit. A spatially inhomogeneous pump beam has been used to create an antiwaveguide structure for a copropagating weak probe beam. Transverse modulated index of refraction and gain due to the spatially dependent pump beam hold the keys for steering, splitting and cloning of an optical beam. We show that how an extra control field permits the propagation of an optical beam through an otherwise gain medium without diffraction and instability.

Chapter 5 includes a brief summary of important findings for improving spatial resolution of diffraction-limited images by exploring different quantum optical phenomena.

Appendix A describes a numerical technique based on split-step Fourier method to solve the paraxial wave equations in optical media.

Contents

List of Figures

Chapter 1

Introduction

Diffraction phenomenon in optics is an inevitable subject which exhibits the wave nature of light discovered by C. Huygens and A. J. Fresnel in 17th century [1]. The origin of diffraction is that any wave envelope or image with finite size can be considered as a group of different plane-wave components. Each plane wave component acquires a unique phase shift during propagation either in free space or medium. The superposition of all plane wave components at any point in space with different phases leads paraxial spreading or diffraction. This also implies that wave envelope or an arbitrary image carried by a laser beam is subjected to diffraction and hence, it is distorted after propagating through medium or vacuum. Optical diffraction imposes a fundamental limitation to the creation, detection or transmission of images in traditional optics and determines the minimum size of an image. In 19th century Lord Rayleigh discovered the first theoretical limit on a spatial resolution of an optical system coined as Rayleigh criterion [2, 3]. Rayleigh's criterion states that two point sources of coherent light are said to be just resolved when the principal maximum of the Airy pattern generated from one point source matches with the first minimum of the other. The typical order of the Rayleigh limit is a value comparable to half of the wavelength ($\lambda/2$) of laser beam. This leads to restriction over focusing of a laser beam into a desired spot.

A glimpse through the history of development of optical diffraction criterion provides a wide area of theoretical and experimental research in various fields. Resolution enhancement or surpassing the diffraction limit is essential in various applications covering metrology, optical imaging, image processing, biological imaging, microscopy, and optical lithography.

A large number of theoretical and experimental research have been carried out for reducing diffraction and breaking the classical diffraction-limit. To reduce the diffraction spreading lots of attempt have been made. For instance, confining the light beam in a physical waveguide like an optical fiber was a successful effort upto a certain extent [4]. Optical fiber supports single-mode as well as multi-mode of light propagation. An optical fiber is a cylindrical waveguide made of a central core surrounded by a cladding layer. The light can be confined inside the narrow core by virtue of refractive index variation, where refractive index of the core is higher than that of the cladding. This causes light beam to obey the principle of total internal reflection and remain confined inside the core along the fiber axis without any further diffraction. However, the energy of the light beam in the fiber is not completely confined in the core region. A significant fraction of the injected energy travels into the cladding in the form of an evanescent wave. Other major losses in optical fiber are primarily due to scattering and absorption which causes reduction and attenuation in the intensity of the light beam. This loss in intensity and distortion due to dispersion puts restriction on information transmission by optical fiber which redirects to alternatives of optical fiber.

Guiding light through a nonlinear medium provides flexibility to overcome the fiber's limitations. Optical diffraction can be greatly suppressed, eliminated or even reversed by using light-matter interaction. The invention of laser in modern quantum optics and its interaction with matter provided a new way to control the optical properties by means of nonlinearity in the medium. In a nonlinear medium, optical properties such as absorption and dispersion are modified and enhanced to a great extent. More interestingly, the coherent medium with modified and improved optical properties can be used further to control the propagation of laser fields.

Numerous attempt have been made in order to elaborate light-guiding in all-optical processing. In this context, optical soliton has been introduced to overcome or reduce the loss in intensity and distortion occurring in optical fiber. Spatial optical solitons are stable solitary wave formed when the medium nonlinearity balances the diffraction-induced beam spreading [5, 6]. Spatial optical solitons have been found to play the major role because of their self-induced focusing and creating its own waveguide effect over a significant distances. The advantage of using spatial solitons is that they can propagate over longer distances without changing their shape. Optical solitons have huge information carrying capacity in optical communication systems as compared to optical fiber [7]. Much of the recent progress in this

area exploits the spatial bright [8] and dark [9] solitons to write a waveguide in a kerr nonlinear medium. Kerr nonlinearity takes place in a medium where variation in an index of refraction is proportional to the intensity of the laser field [5, 6, 10, 11]. Fuente *et al.* first experimentally demonstrated that a waveguide structure can be written by using a bright spatial soliton in bulk media [12]. In their experiment, an intense pump beam forming a solition is used for waveguiding a weak probe beam. Luther-Davies and co-workers have demonstrated that the dark soliton can also induce waveguides for guiding a probe beam in a nonlinear thermal media [13]. Their experiment showed that a pair of diverging dark solitons can form a "Y junction" that splits a single input beam into two independent guided beams. Moreover, they have optically produced such a waveguide that can be steered and used to produce an optical switchyard [14]. Formation of waveguide is also possible by using a spatial soliton in the bulk photorefractive material as reported by Morin and colleagues [15]. According to them, guiding efficiency can be enhanced using tapered waveguides.

In comparison with bulk nonlinear media, spatial solitons induced in atomic media has been utilized for waveguiding a weak probe beam. Bortman-Arbiv *et al.* have suggested spatial solitons based waveguiding in a medium composed of two-level atoms [16, 17]. They have shown that a strong pump beam which forms soliton, can create optical waveguiding effect for a co-propagating weak probe beam. They found that the transverse profile of the pump exhibits soliton like oscillations which gets mimic by transmitted probe beam profile. They have also predicted the importance of new four-wave mixing (FWM) process on the induced waveguide [18–20]. FWM is a nonlinear process arising where at least two different frequency components propagate together in a nonlinear medium and a new weak wave is generated. They studied the importance and effect of this weak beam on the waveguiding specially when the medium is optically thick.

Achieving a high intensity laser beam is a major concern to form a spatial soliton in conventional nonlinear medium [21]. Taking into account the equivalent incorporation of gaseous medium, recent developments introduce an all-optical waveguiding at low light intensities. An all-optical waveguide describes to an electromagnetically induced waveguide whose refractive index profile varies transversely by spatially dependent control beam. The physical significance of such induced waveguides is that their properties can be controlled by changing the properties of the control beam in order to fulfill some needs. Additionally, an all-optical waveguide can be created even by comparatively low power laser beams whose divergence is not very severe over a short propagation distance.

The interaction of laser field with atomic vapor media provides a remarkable changes in optical properties of medium as well as laser field propagation [22]. Laser field interacting with atoms in a vapor medium induces atomic transition. This atomic transition or excitation to different coherently coupled atomic levels leads to generation of atomic coherence between levels. The quantum interference between induced atomic coherences are essential to demonstrate many interesting quantum optical phenomena such as coherent population trapping (CPT) [23, 24], electromagnetically induced transparency (EIT) [25, 26], lasing without inversion (LWI) [27–30] and saturated absorption techniques [31, 32]. Quantum coherence and interference effects can give rise to dramatic enhancement of the refractive index without absorption [33–36]. The coherence effect of the stimulated Raman process has been explored to reduce the probe field attenuation or distortion resulting in an absorptive medium. The active Raman gain (ARG) schemes result in a gain spectrum by operating atoms in a stimulated Raman emission mode [37, 38]. The spatial variations of enhanced dispersive property of the medium can be utilized to control the diffraction spreading of laser beams. The exceptionally high efficiency of vapor medium through nonlinear interactions enhances its role in all-optical waveguiding [39, 40].

Most of the research in nonlinear optics is concentrated on electromagnetically induced transparency (EIT). In an EIT process, a strong control beam is used to reduce the absorption and enhance the refractive index of medium around the resonance of a co-propagating weak probe beam. Most importantly, a suitable spatial dependent profile of the control beam patterns a waveguide like structure by modulating refractive index in transverse directions. This special inhomogeneous character of refractive index leads to confinement of co-propagating weak probe beam. There are a large number of theoretical predictions and experimental realizations to accomplish all-optical waveguiding in EIT medium. Moseley *et al.* have theoretically suggested and experimentally verified electromagnetically induced focusing and defocusing of probe beam in EIT medium [41, 42]. The diffraction-limited beam propagation was first experimentally demonstrated in a pure lead (^{208}Pb) vapor medium by Kasapi *et al.* [43]. They have generated a spatial profile of probe beam by passing it through an aperture. By controlling the detuning of control beam, they have shown the propagation of spatially modulated probe beam with and without distortion. Truscott *et al.* were the first to demonstrate experimentally the formation of optically written waveguide in an atomic rubidium vapor [44]. In this experiment, rubidium atoms form a three-level V-configuration, where a weak probe beam and a strong pump beam are coupled to two different excited states while

sharing a common ground state. They have used pump beam with a Laguerre-Gaussian charge 3 doughnut-shaped profile to pattern an atomic waveguide for guiding weak probe beam. The doughnut-shaped pump beam creates a steep-sided refractive index spatial profile by coherent pumping the ground state population to one of the excited states. Their experiment was later examined in great detail theoretically by Kapoor *et al.* [45] and Anderson *et al.* [46] by considering full density matrix treatment. The spatially varying refractive index is also accounted for induced focusing [47, 48], transverse confinement [49, 50], self-imaging [51], and optical beam steering [52–54].

In comparison with EIT approach, saturated absorption spectroscopy technique in two-level atoms has also been utilized to show diffraction-free propagation of laser beams. This mechanism offers promising advantages in slow light propagation which is very useful for quantum information technology [55, 56]. In this technique, a strong pump beam creates a very narrow spectral hole in the absorption profile of a copropagating weak beam which leads to an increase in its transmission [31, 32]. This induced spectral hole is accompanied by a strong dispersion which causes slow light propagation. Utilizing this saturation absorption mechanism, Dey *et al.* [57] have recently proposed a waveguiding scheme in a two-level system. By taking different spatial modes of pump beam, they showed that paraxial diffraction of probe beam can be partially eliminated in saturated absorptive medium. They found that a super-Gaussian profile is preferable as compared to other pump beam shapes for diffraction-free propagation of Gaussian probe beam. Furthermore, they have presupposed that how a probe beam partially acquires the transverse shape of pump beam at the output of the medium which might be applicable in optical microscopy.

In addition to the previous mechanism, coherent Raman process in rubidium atoms have been used for all-optical waveguiding by Praveen *et al.* [58]. They modeled atoms as three-level Λ-system and operated in off-resonance Raman configuration. Taking into account the Raman resonance phenomenon, they observed that the signal beam transmission rapidly changes and resulted in a sharp variation in refractive index at signal frequencies near Raman resonance. They used control beam as a first order Laguerre-Gaussian mode to induce a fiber like index variation for confining a weak signal beam. Their experiment shows that the coupling efficiency of the guided signal beam has a linear relationship with input signal beam. Their findings predicted that induced atomic waveguide may be useful in efficient nonlinear processes at very low power beams.

Objective of the above mentioned study is meant to summarize theoretical and experimental approaches so far for suppressing the diffraction. However, all of these optically written waveguide based schemes are limited to either a single transverse mode or only certain spatial modes of guiding beam. Besides the various advantages of these attempts, specific mode propagation restricts their applicability in emerging areas such as image processing with high resolution, quantum information processing, data storage and optical imaging. Thus so far, waveguiding with multimode profiles have not been implemented in above mentioned guiding schemes. With all of these limitation to the context of diffraction in mind, intensive research has been carried out in modern optics. Theoretical investigations as well as experimental examination were carried out currently for surpassing the diffraction and enhancing the resolution in multimode wave profile.

An entirely diffrent approch of transmission of an arbitrary image by means of multimode incoherent soliton in self-focusing nonlinear medium has been used by Kip *et al.* [59] . In their experiment they used a sufficiently broad and spatially incoherent soliton to write a multimode waveguide in a photorefractive crystal. The number of guided modes of that induced waveguide are large enough to supports the transmission of an incoherent image through the nonlinear medium. This scheme was remarkable but limited to the transmission of only an incoherent image. In case of coherent images, destruction of the image information is caused by both modal and modulational instability, which lead to filamentation of parts of the image.

In a very recent study, a more challenging and counterintuitive approach to remove the restriction over spatial modes has been theoretically proposed and experimentally verified by Firstenberg *et al.* [60–62]. This scheme is fundamentally different from stationary waveguide methods in the sense that the nonuniformity in susceptibility is created in momentum space instead of real space. They have exploited the atomic thermal motions and collisions to eliminate the paraxial diffraction of arbitrary images under EIT mechanism. The underlying physics in this approach can be explained as the phase difference acquired during propagation for each plane-wave component of the image is exactly compensated by an additional phase shift induced by the atomic motion, thus leading to the elimination of diffraction. Experimental challenge associated with this method is that it assumes an explicit breaking of the usual two-photon resonance condition such that strong absorption occurs. This strong attenuation results inherent loss in resolution which restricts its applicability in quantum information technology. Recently, Zhang *et al.* [63] have exploited the thermal motion of atoms to show

the diffraction-less propagation of an arbitrary image and frequency conversion via four-wave mixing process.

For the progress in this study, the diffraction-less propagation of multimode light beam through optically written waveguides is theoretically demonstrated by Dey *et al.* [64]. They have used Laguerre-Gaussian control beam to write waveguide for confining probe beam in off-resonant Raman system. They have shown that a probe beam with a single Gaussian, two Gaussian modes, and multiple secant-hyperbolic shaped can be propagated without diffraction. This diffraction-less propagation of multimode transverse images solves the difficulty of waveguides which were earlier limited to a single transverse mode. Moreover, they have also predicted that by varying the spot size of the Laguerre-Gaussian control beam it is possible to control the transmission and feature size of the output probe beam. This scheme introduces a novel approach for the propagation of arbitrary images in warm atomic vapors.

A significant contribution in theoretical and experimental approaches to limit the diffraction sets a milestone. However, the proposed investigations and their applicability in different areas are limited due to less resolution and distortion in arbitrary image processing. Resolution enhancement is the ultimate purpose for creation, detection and transmission of the smaller images. The light-matter interaction provides a wide variety of diffraction-free techniques to beat the fundamental diffraction-limit in both near-field and far-field regimes. For examples, near-field and far-field fluorescence spectroscopy techniques are used to obtain 3D image of living cells [65, 66]. In another proposal, possibility to attain spatial resolution of a fraction of wavelength of light has been developed by stimulated emission depletion (STED) fluorescence microscopy [67–69]. In these optical microscopy techniques, an object with nanometer resolution could be imaged by recording fluorescence spectrum from single atoms or molecules. The position of an atom with subwavelength precision have been measured using classical field amplitude and phase arrangements techniques [70, 71]. Even more appreciable work has been explored by coherent coupling of atomic system with standing wave, to measure the separation between two closely situated atoms [72, 73]. Chang *et al.* have suggested a new microscopy scheme that can determine the separation between two identical atoms with subwavelength precision [74]. In this scheme, two identical atoms are interacting with a standing wave laser field in a cavity. The information about atoms position is extracted from the collective resonance fluorescence spectrum of atoms. The quadrature-field measurement of nonclassical fields are also used to locate the position of atom with subwavelength

accuracy by moving atomic beam through a cavity [75–78]. These schemes are based on the concept of virtual slits formed by localized atoms.

Recently, several new atomic localization schemes have been proposed by detecting the spontaneously emitted photons [79]. These methods also exploited the interaction of the atom with the classical standing wave field. An atomic localization scheme by using a simple two-level system interacting with the classical standing-wave field has been suggested by Qamar *et al.* [80]. They measured the resonance fluorescence spectrum from two-level atomic system and extracted information about the position of the atom. The precise measurement of atom position has been increased by utilizing three-level [81, 82] and four-level atomic systems [83]. The amplitude and phase control of the absorption [84] and gain [85] spectrum of four-level atomic system have been also exploited for subwavelength atom localization.

Optical lithography techniques based on classical fields have been limited due to the diffraction. In optical lithography, a light field is used to etch a substrate for writing a pattern which is widely used in microchip semiconductor industries [86]. However, optical lithography based on classical field approach can create structures on a scale comparable to half of the wavelength of light ($\lambda/2$). Therefore, quantum optical based schemes are applied for the fabrication of small mask structures in optical lithography beyond the diffraction-limit. Boto *et al.* discussed theoretically to surpass this diffraction-limit by using nonclassical quantum nature of entangled N-photon [87]. Interestingly, they showed that it is possible to create structures with minimum size of $\lambda/(2N)$ in an N-photon absorbing substrate. This theoretical prediction was later verified experimentally by Angelo *et al.* via utilizing two-photon entangled states [88]. Their experimental results show that the classical diffraction-limit can be beaten by a factor of two. Recently, Kiffner *et al.* have proposed a new approach based on CPT to obtain same spatial resolution $\lambda/(2N)$ which does not need an N-photon absorption process [89]. This scheme utilizes a position dependent dark state via exposing the atoms with standing wave patterns and requires multilambda systems and multiple laser beams. To avoid the requirement of multiphoton absorption or entanglement of the photons, Liao *et al.* have suggested a new method to subwavelength lithography via Rabi oscillations between two atomic levels [90]. Quantum optical lithography with subwavelength resolution has been later predicted by using classical field in Doppleron-type resonances [91]. Optical lithography with super-resolution has been also suggested via interaction between Λ-type atoms and temporally-cascaded driving fields [92].

1.1 Theoretical background of atom-field interaction

Before beginning the detailed discussion on light-matter interaction in quantum optics, it is important to first understand the fundamentals of semiclassical theory. In semiclassical theory, the atoms are treated as quantum system with their discrete energy levels and the fields are treated classically. The dynamics of atoms are governed by a appropriate density operator obeying the Liouville equation. The basic Maxwell's equations of classical electrodynamics are used to describe the propagation of electromagnetic fields. We start with the derivation of atom-field interaction Hamiltonian from a gauge invariance point of view and then simplify it under electric dipole approximation.

1.1.1 Atom-field interaction Hamiltonian

We consider the interaction between the electromagnetic fields and alkali metal atoms. All alkali atoms have a single electron in their outermost shell while inner shells are nearly filled. In such atoms, the outer electron of charge $-e$ and mass m is bound to the nucleus by the Coulomb interaction $V(r)$. In the presence of $V(r)$, the Hamiltonian of the electron is expressed as

$$H_0 = \frac{\mathbf{P}^2}{2m} + V(r)\,, \tag{1.1}$$

where $\mathbf{P}$ is the canonical momentum and r is the position of the electron. We now derive the Hamiltonian of the electron in the presence of external electromagnetic (em) fields. The electric field $\mathbf{E}$ and magnetic field $\mathbf{B}$ associated with em field can be expressed in the following form:

$$\mathbf{E}(\mathbf{r},t) = -\nabla\Phi(\mathbf{r},t) - \frac{1}{c}\frac{\partial}{\partial t}\mathbf{A}(\mathbf{r},t) \tag{1.2}$$

$$\mathbf{B}(\mathbf{r},t) = \nabla \times \mathbf{A}(\mathbf{r},t)\,, \tag{1.3}$$

where $\mathbf{A}(\mathbf{r},t)$ is the vector potential and $\Phi(\mathbf{r},t)$ is the scalar potential of the external field, c is the speed of light in vacuum. Using these expressions for the fields in the Lorentz force equation: $\mathbf{F} = -e[\mathbf{E} + (\mathbf{V} \times \mathbf{B})/c]$ and comparing it with classical Lagrange's equation, one

can readily find the modified Hamiltonian as

$$H' = \frac{1}{2m}\left[\mathbf{P} + \frac{e}{c}\mathbf{A}(\mathbf{r},t)\right]^2 - e\Phi(\mathbf{r},t)\,. \tag{1.4}$$

Thus the total Hamiltonian of atom-field system takes the following form

$$H = \frac{1}{2m}\left[\mathbf{P} + \frac{e}{c}\mathbf{A}(\mathbf{r},t)\right]^2 - e\Phi(\mathbf{r},t) + V(r)\,. \tag{1.5}$$

We now discuss the motion of the electron in the nuclear and external fields and derive this total Hamiltonian from a gauge invariant point of view.

1.1.2 Interaction Hamiltonian under gauge transformation

In quantum mechanics the quantization of the particle motion is done by replacing all observables by their operators forms such as momentum $\mathbf{P} \rightarrow \hat{\mathbf{P}} = -i\hbar\nabla$, and the total energy $\mathrm{E}\rightarrow\hat{\mathrm{E}} = i\hbar\frac{\partial}{\partial t}$, where $\hbar = h/2\pi$ is the reduced Planck's constant. Thus the motion of an electron in the nuclear field is described by the non-relativistic Schrödinger equation:

$$i\hbar\frac{\partial}{\partial t}\Psi(\mathbf{r},t) = \left[\frac{-\hbar^2}{2m_e}\nabla^2 + V(r)\right]\Psi(\mathbf{r},t), \tag{1.6}$$

where $\Psi(\mathbf{r},t)$ is the wave function of the quantum system and the quantity, $|\Psi(\mathbf{r},t)|^2$ gives the probability density of finding an electron at position $\mathbf{r}$ and time t. The general solution of Eq. (1.6) can be written as:

$$\Psi(\mathbf{r},t) = \psi(\mathbf{r},t)e^{i\chi}, \tag{1.7}$$

where χ is an arbitrary scalar function and does not affect the probability density. Therefore, the phase factor χ is optional as the two wave functions differing by a constant phase factor signify the same physical state. However, if the phase is a function of both space and time variables, then the solution of the following form

$$\Psi(\mathbf{r},t) = \psi(\mathbf{r},t)e^{i\chi(\mathbf{r},t)}\,, \tag{1.8}$$

does not satisfy the Schrödinger equation Eq. (1.6), but the probability density still remains invariant under this transformation. Therefore, we must modify the Schrödinger equation in

order to satisfy local gauge or phase invariance. The modified Schrödinger equation is given by

$$i\hbar\frac{\partial}{\partial t}\Psi(\mathbf{r},t) = \left\{\frac{1}{2m}\left[-i\hbar\nabla + \frac{e}{c}\mathbf{A}(\mathbf{r},t)\right]^2 - e\Phi(\mathbf{r},t) + V(r)\right\}\Psi(\mathbf{r},t)\,, \tag{1.9}$$

where the functions $\mathbf{A}(\mathbf{r},t)$ and $\Phi(\mathbf{r},t)$ on right hand side of Eq. (1.9) represent the usual vector and scalar potentials of the external electromagnetic field, respectively. In order to make Eq. (1.9) invariant under a transformation akin in Eq. (1.8), the functions $\mathbf{A}(\mathbf{r},t)$ and $\Phi(\mathbf{r},t)$ has to be replaced by their gauge transformations

$$\mathbf{A}(\mathbf{r},t) \rightarrow \mathbf{A}'(\mathbf{r},t) = \mathbf{A}(\mathbf{r},t) - \frac{\hbar c}{e}\nabla\chi(\mathbf{r},t)\,, \tag{1.10}$$

$$\Phi(\mathbf{r},t) \rightarrow \Phi'(\mathbf{r},t) = \Phi(\mathbf{r},t) + \frac{\hbar}{e}\frac{\partial\chi(\mathbf{r},t)}{\partial t}\,. \tag{1.11}$$

Under these gauge transformations, the fields $\mathbf{E}$ and $\mathbf{B}$ remain invariant [93]. After simplification and rearrangement, the Eq. (1.9) takes new form

$$i\hbar\frac{\partial}{\partial t}\Psi(\mathbf{r},t) = \hat{H}\Psi(\mathbf{r},t)\,. \tag{1.12}$$

where $\hat{H}$ is the total Hamiltonian and is given by

$$\begin{aligned}\hat{H} = &-\frac{\hbar^2}{2m}\nabla^2 - \frac{ie\hbar}{2mc}[\mathbf{A}(\mathbf{r},t)\cdot\nabla + \nabla\cdot\mathbf{A}(\mathbf{r},t)] + \frac{e^2}{2mc^2}\mathbf{A}(\mathbf{r},t)\cdot\mathbf{A}(\mathbf{r},t)\\ &- e\Phi(\mathbf{r},t) + V(r)\,.\end{aligned} \tag{1.13}$$

We simplify $\hat{H}$ by considering Coulomb gauge condition, i.e., $\Phi(\mathbf{r},t) = 0$ and $\nabla\cdot\mathbf{A}(\mathbf{r},t) = 0$. The total Hamiltonian in the radiation gauge becomes

$$\hat{H} = -\frac{\hbar^2}{2m}\nabla^2 + V(r) - \frac{ie\hbar}{mc}\mathbf{A}(\mathbf{r},t)\cdot\nabla + \frac{e^2}{2mc^2}\mathbf{A}(\mathbf{r},t)\cdot\mathbf{A}(\mathbf{r},t)\,. \tag{1.14}$$

We further simplify the above Hamiltonian under a reasonable approximation known as dipole approximation.

1.1.3 The electric dipole approximation

We are interested in a problem of the bound electron and its behavior in the presence of an incident plane electromagnetic wave. A plane electromagnetic wave is described by a vector potential $\mathbf{A}(\mathbf{r_0}+\mathbf{r},t)$:

$$\mathbf{A}(\mathbf{r_0}+\mathbf{r},t) = \mathbf{A}(t)\exp[i\mathbf{k}\cdot(\mathbf{r_0}+\mathbf{r})]\,, \tag{1.15}$$

where $\mathbf{r_0}$ is location of nucleus of the atom. We assume that the wavelength of the electromagnetic field is much larger than the typical size of the atom, which is of the order of the Bohr radius a_0. Thus the spatial variation of electromagnetic field is nearly constant over the dimension of the atom. Under this approximation, $\mathbf{k}\cdot\mathbf{r} << 1$, where $|\mathbf{k}| = 2\pi/\lambda$ is the wave vector and λ is the wavelength of the radiation field, the vector potential can be written as

$$\begin{aligned}\mathbf{A}(\mathbf{r_0}+\mathbf{r},t) &= \mathbf{A}(t)\exp[i\mathbf{k}\cdot(\mathbf{r_0}+\mathbf{r})]\\ &= \mathbf{A}(t)\exp(i\mathbf{k}\cdot\mathbf{r_0})(1+i\mathbf{k}\cdot\mathbf{r}+...)\\ &\approx \mathbf{A}(t)\exp(i\mathbf{k}\cdot\mathbf{r_0})\,.\end{aligned} \tag{1.16}$$

This is so called the "*electric dipole approximation*". Hence a spatially uniform vector potential $\mathbf{A}(\mathbf{r_0}+\mathbf{r},t) \approx \mathbf{A}(\mathbf{r_0},t)$ is considered in further study. The total Hamiltonian for the field-atom interaction in the dipole approximation is given by

$$\hat{H} = -\frac{\hbar^2}{2m}\nabla^2 + V(r) - \frac{ie\hbar}{mc}\mathbf{A}(\mathbf{r_0},t)\cdot\nabla + \frac{e^2}{2mc^2}\mathbf{A}^2(\mathbf{r_0},t)\,. \tag{1.17}$$

We now perform a gauge transformation using $\chi(\mathbf{r},t) = (-e/\hbar c)\mathbf{A}(\mathbf{r_0},t)\cdot\mathbf{r}$. Thus the wave function $\Psi(\mathbf{r},t)$ of Eq. (1.8) takes new form

$$\Psi(\mathbf{r},t) = \exp\left[\frac{-ie}{\hbar c}\mathbf{A}(\mathbf{r_0},t)\cdot\mathbf{r}\right]\psi(\mathbf{r},t)\,, \tag{1.18}$$

Substituting Eq. (1.17) and Eq. (1.18) in Schrödinger Eq. (1.12) and after simplification, we find

$$i\hbar\left[\frac{-ie}{\hbar c}\dot{\mathbf{A}}(\mathbf{r_0},t)\cdot\mathbf{r}\psi(\mathbf{r},t) + \dot{\psi}(\mathbf{r},t)\right] = \left[-\frac{\hbar^2}{2m}\nabla^2 + V(r)\right]\psi(\mathbf{r},t)\,.$$

We can express the $\mathbf{E}$ field at $\mathbf{r_0}$ in terms of the Coulomb gauge potential as $\mathbf{E}(\mathbf{r_0}, t) = -\frac{1}{c}\frac{\partial}{\partial t}\mathbf{A}(\mathbf{r_0}, t)$. Therefore the simplified form of Schrödinger equation under electric dipole approximation is given by

$$\begin{aligned} i\hbar\frac{\partial}{\partial t}\psi(\mathbf{r}, t) &= \left\{-\frac{\hbar^2}{2m}\nabla^2 + V(r) + e\mathbf{r}\cdot\mathbf{E}(\mathbf{r_0}, t)\right\}\psi(\mathbf{r}, t) \\ &= (\hat{H}_0 + \hat{H}_I)\psi(\mathbf{r}, t)\,. \end{aligned} \tag{1.19}$$

where $\hat{H}_0$ is the unperturbed Hamiltonian in the absence of the incident electric field and is given by

$$\hat{H}_0 = -\frac{\hbar^2}{2m}\nabla^2 + V(r), \tag{1.20}$$

and $\hat{H}_I$ represents interaction Hamiltonian of atom-field system after electric dipole approximation. This is expressed as

$$\hat{H}_I = e\hat{\mathbf{r}}\cdot\mathbf{E}(\mathbf{r_0}, t) = -\hat{\mathbf{d}}\cdot\mathbf{E}(\mathbf{r_0}, t)\,, \tag{1.21}$$

where $\hat{\mathbf{d}}$ $(= -e\hat{\mathbf{r}})$ is the electric dipole moment operator of the atom. This interaction Hamiltonian has been used to study the atom-field interaction in our forthcoming problems. One of the simplest problems of atom-field interaction is a two-level atomic model system. A two-level atomic system can be realized in the experiment when only two atomic levels are resonant or nearly resonant with the frequency of incident em radiation, while all other levels are highly detuned. We therefore present the basic results of a two-level atom interacting with a near resonant laser field.

1.2 Interaction of light with a system of two-level atoms

The unperturbed Hamiltonian $\hat{H}_0$ in Eq. (1.20) of an atom has a set of eigenstates $|i\rangle$. These eigenstates represent the various internal stationary states of the atom. We first consider only two energy eigenstates of an atom with a ground state $|1\rangle$ and an excited state $|2\rangle$ as shown in Fig. 1.1.

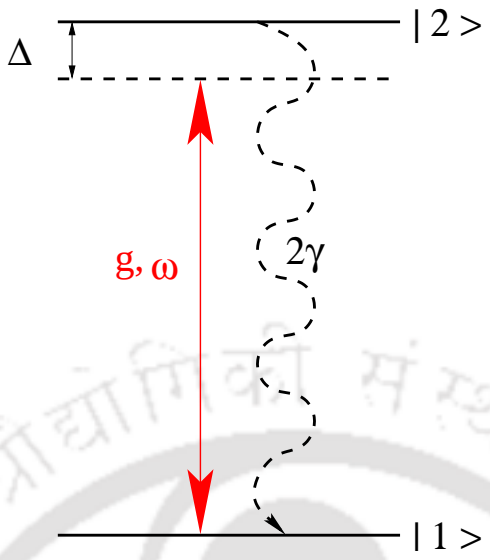

FIGURE 1.1: The energy level diagram of a two-level rubidium atom. The atomic system is driven by a monochromatic laser field of Rabi frequency g and angular frequency ω. The spontaneous decay rate of the excited state $|2\rangle$ to ground state $|1\rangle$ is labeled by 2γ.

The energy eigenvalues corresponding to the eigenstates $|1\rangle$ and $|2\rangle$ are given by following eigenvalue equation:

$$\hat{H}_0|i\rangle = \hbar\omega_i|i\rangle = E_i|i\rangle\,, \tag{1.22}$$

where $\hbar\omega_i$ $(i = 1, 2)$ is the energy eigenvalue of state $|i\rangle$. Therefore, the transition frequency between the two levels is given by $\omega_{21} = (E_2 - E_1)/\hbar$. The eigenstates form a complete set of orthonormal states and satisfy the closure relation: $\sum_i |i\rangle\langle i|$=1. Keeping this fact in mind, we can express $\hat{H}_0$ in terms of the eigenstates and their corresponding eigenvalues as

$$\begin{aligned}\hat{H}_0 &= \sum_{i,j=1}^{2} |i\rangle\langle i|\hat{H}_0|j\rangle\langle j| = \sum_{i=1}^{2} \hbar\omega_i|i\rangle\langle i| \\ &= \hbar\omega_1|1\rangle\langle 1| + \hbar\omega_2|2\rangle\langle 2|\,.\end{aligned} \tag{1.23}$$

We now consider the effect of an external electromagnetic field on the atom. The electric field associated with an electromagnetic wave is defined by

$$\mathbf{E}(\mathbf{r}, t) = \hat{\mathbf{e}}\mathcal{E}_0(\mathbf{r})\, e^{i(\mathbf{k}\cdot\mathbf{r}-\omega t)} + \text{c.c.}\,, \tag{1.24}$$

where $\mathcal{E}_0(\mathbf{r})$ is the slowing varying amplitude, $\hat{\mathbf{e}}$ is the unit polarization vector, and $\mathbf{k}$ ($|\mathbf{k}| = \omega/c$) is the wave vector of field. Note that the complex conjugate (c.c.) term has been added in above equation in order to make electric field as real quantity. The carrier frequency ω of the laser field is very close to atomic resonance frequency ω_{21}. The electric field $\mathbf{E}(\mathbf{r}, t)$ induces a dipole moment between the two atomic levels. The explicit form of the electric dipole moment operator, using same procedure as in Eq. (1.23), is given by

$$\hat{\mathbf{d}} = \sum_{i,j=1}^{2} \mathbf{d}_{ij}|i\rangle\langle j| = |1\rangle\langle 2|\mathbf{d}_{12} + |2\rangle\langle 1|\mathbf{d}_{21}\,, \tag{1.25}$$

where $\mathbf{d}_{ij} = \langle i|\hat{\mathbf{d}}|j\rangle$ is a off-diagonal matrix element of the electric dipole moment operator. The off-diagonal matrix elements do exist as two atomic levels have opposite parity. It should be noted that the diagonal matrix elements $\mathbf{d}_{11}$ and $\mathbf{d}_{22}$ are zero because the dipole operator has odd parity. The induced electric dipole moment interacts with the incident electric field and gives rise an interaction energy. The interaction energy of the atom-field system under dipole approximation is given by the interaction Hamiltonian $\hat{H}_I$,

$$\hat{H}_I = -\hat{\mathbf{d}} \cdot \mathbf{E} = -(|1\rangle\langle 2|\mathbf{d}_{12} \cdot \mathbf{E} + |2\rangle\langle 1|\mathbf{d}_{21} \cdot \mathbf{E}). \tag{1.26}$$

Therefore, the total Hamiltonian of the atom-field system is given by

$$\hat{H} = \hat{H}_0 + \hat{H}_I = \hbar\omega_{21}|2\rangle\langle 2| - (|1\rangle\langle 2|\mathbf{d}_{12} \cdot \mathbf{E} + |2\rangle\langle 1|\mathbf{d}_{21} \cdot \mathbf{E}), \tag{1.27}$$

where $\hbar\omega_{21}$ is the energy of the excited state $|2\rangle$ relative to the ground state $|1\rangle$, which is assumed to be at zero energy for a reference.

Substituting the expression for electric field from Eq. (1.24) into Eq. (1.27), we find explicit form of total Hamiltonian as

$$\begin{aligned}\hat{H} = \hbar\omega_{21}|2\rangle\langle 2| - \Big[\mathbf{d}_{21} \cdot \hat{\mathbf{e}}\mathcal{E}(\mathbf{r})\, e^{i(\mathbf{k}\cdot\mathbf{r}-\omega t)} + \mathbf{d}_{21} \cdot \hat{\mathbf{e}}\mathcal{E}^*(\mathbf{r})\, e^{-i(\mathbf{k}\cdot\mathbf{r}-\omega t)}\Big]|2\rangle\langle 1| \\ - \Big[\mathbf{d}_{12} \cdot \hat{\mathbf{e}}\mathcal{E}(\mathbf{r})\, e^{i(\mathbf{k}\cdot\mathbf{r}-\omega t)} + \mathbf{d}_{12} \cdot \hat{\mathbf{e}}\mathcal{E}^*(\mathbf{r})\, e^{-i(\mathbf{k}\cdot\mathbf{r}-\omega t)}\Big]|1\rangle\langle 2|\,.\end{aligned} \tag{1.28}$$

Defining the new quantities

$$g = \frac{\mathbf{d}_{21} \cdot \hat{\mathbf{e}}\mathcal{E}}{\hbar}\, e^{i\mathbf{k}\cdot\mathbf{r}}\,, \tilde{g} = \frac{\mathbf{d}_{21} \cdot \hat{\mathbf{e}}\mathcal{E}^*}{\hbar}\, e^{-i\mathbf{k}\cdot\mathbf{r}}\,, \tag{1.29}$$

where $g(\tilde{g})$ is referred as the Rabi frequency (counter-rotating frequency) of the laser field. Note that under dipole approximation, the spatial phase factors appearing in definitions of Rabi frequencies are treated to be unity. The total Hamiltonian by including these new parameters can be written as

$$\hat{H} = \hbar\omega_{21}|2\rangle\langle 2| - \hbar\Big[g\, e^{-i\omega t} + \tilde{g}\, e^{i\omega t}\Big]|2\rangle\langle 1| - \hbar\Big[\tilde{g^*}\, e^{-i\omega t} + g^*\, e^{i\omega t}\Big]|1\rangle\langle 2|\,. \tag{1.30}$$

It is very clear from Eq. (1.30) that the total Hamiltonian is time-dependent as the interaction part contains rapidly oscillating phase factors. Thus we cannot find the solution to the Schrödinger equation Eq. (1.19) unless we remove the time-dependent parts. However, under a suitable unitary transformation we can transform the total Hamiltonian Eq. (1.30) into a time-independent form. We consider a transformation of the following form

$$\hat{U} = e^{-i\omega|2\rangle\langle 2|t} \tag{1.31}$$

This unitary transformation is known as a "*rotating frame transformation*". If $|\psi(\mathbf{r},t)\rangle$ and $|\phi(\mathbf{r},t)\rangle$ represent the state vectors of the system in the stationary frame and the rotating frame, respectively, then they can be related by

$$|\psi(\mathbf{r},t)\rangle = \hat{U}|\phi(\mathbf{r},t)\rangle\,. \tag{1.32}$$

Using above unitary transformation into the Schrödinger equation Eq. (1.19) and after rearranging the terms we obtain

$$i\hbar\frac{\partial}{\partial t}|\phi(\mathbf{r},t)\rangle = (\hat{U}^\dagger\hat{H}\hat{U} - i\hbar\hat{U}^\dagger\frac{\partial\hat{U}}{\partial t})|\phi(\mathbf{r},t)\rangle = \hat{\mathcal{H}}|\phi(\mathbf{r},t)\rangle\,. \tag{1.33}$$

Obviously, the state vectors in the rotating frame obey the Schrödinger equation with a transformed Hamiltonian given by

$$\hat{\mathcal{H}} = \hbar\Delta|2\rangle\langle 2| - \hbar\Big[g + \tilde{g}\, e^{2i\omega t}\Big]|2\rangle\langle 1| - \hbar\Big[\tilde{g^*}\, e^{-2i\omega t} + g^*\Big]|1\rangle\langle 2|\,, \tag{1.34}$$

where $\Delta = \omega_{21} - \omega$ is the detuning of the laser field from the transition. In equation Eq. (4.2), the rapidly oscillating terms at frequency $\pm 2\omega$ will give zero value on an average in a time scale of an optical period as compared to without oscillating terms. This is because the value

of $\tilde{g} \ll 2\omega$ in the optical frequency domain. The terms related to $\tilde{g}$ along with complex conjugates will be important only if $\tilde{g} \approx 2\omega$. Therefore, we neglect these rapidly oscillating terms while retaining the dc terms. This approximation is known as the "*rotating-wave approximation*" (RWA). The effective Hamiltonian for the system of interest in the appropriate rotating frame can be written as

$$\hat{\mathcal{H}} = \hbar\Delta|2\rangle\langle 2| - \hbar(g|2\rangle\langle 1| + g^*|1\rangle\langle 2|)\,. \tag{1.35}$$

This is effective Hamiltonian for a single atom under rotating-wave approximation. We can readily write the state vector $|\psi\rangle$ of a single two-level atom which contains all possible information about the system. Also, the time evolution of state vector for a single atom can be well described by Schrödinger equation Eq. (1.19). However, for a collection of many such atoms, we can not guess the actual state of individual atoms as each atom is in an unspecified state. Therefore, we describe the physical state of an ensemble of many identical quantum systems by adopting density operator ρ formalism.

1.2.1 The Liouville equation for a two-level atomic system

The density operator ρ is defined as a projection operator onto the state vector.

$$\rho = \sum_i P_i|\psi_i\rangle\langle\psi_i|\,, \tag{1.36}$$

where P_i is the time-independent probability of finding the system in state $|\psi_i\rangle$. Generally, P_i is statistical probability of finding an individual N_i systems in state $|\psi_i\rangle$ and described by $P_i = N_i/N$, where $\sum_i P_i = 1$ and $\sum_i N_i = N$. The time derivative of this equation is given by

$$\dot{\rho} = \sum_i P_i(|\dot{\psi}_i\rangle\langle\psi_i| + |\psi_i\rangle\langle\dot{\psi}_i|)\,, \tag{1.37}$$

where over-dot denotes a partial derivative with respect to time t. Substituting $|\dot{\psi}_i\rangle$ and $\langle\dot{\psi}_i|$ from the Schrödinger equation Eq. (1.19) into Eq. (1.37), we obtain

$$\dot{\rho} = -\frac{i}{\hbar}\Big[\hat{\mathcal{H}}, \rho\Big]\,. \tag{1.38}$$

This equation is known as the Liouville or Von Neumann equation. It is more general form of equation of motion than the Schrödinger equation and it gives statistical as well as quantum

mechanical information about the system. Using the transformed Hamiltonian of Eq. (1.35) into Eq. (1.38), the equations of motion for the density matrix elements is given by

$$\dot{\rho}_{22} = -\dot{\rho}_{11} = ig\rho_{12} - ig^{*}\rho_{21}\,, \tag{1.39}$$

$$\dot{\rho}_{21} = \dot{\rho}^{*}_{12} = -i\Delta\rho_{21} + ig(\rho_{11} - \rho_{22})\,. \tag{1.40}$$

These equations have resemblance to the equations obtained by Bloch in the context of the motion of a spin-1/2 system in an oscillatory magnetic field. Therefore, the above equations are known as the optical Bloch equations [94]. In a general solution of density matrix elements, the diagonal elements ρ_{ii} are real while off-diagonal elements ρ_{ij} are complex. The physical interpretations of the density matrix elements are as follows: The diagonal element ρ_{11} gives the probability of finding atom in the ground state $|1\rangle$, while ρ_{22} denotes the probability of finding atom in the excited state $|2\rangle$. Note that the total probability is conserved for a closed system, i.e., $\rho_{11} + \rho_{22} = 1$. The off-diagonal element ρ_{12} $(=\rho^{*}_{21})$ represents the coherence between levels $|1\rangle$ and $|2\rangle$. The physical meaning of the off-diagonal elements are more abstract as they describe the atomic polarization. This atomic polarization is related to the macroscopic polarization of the atomic medium.

1.2.2 Rabi oscillations in two-level system

Eqs. (1.39) and (1.40) are basically a set of four simultaneous equations for the four elements of the density matrix. We solve these equations by assuming that atom is initially in the ground state $|1\rangle$, i.e., $\rho_{11} = 1$ at time $t = 0$. The solutions for atomic population ρ_{22} and coherence ρ_{21} are then given by

$$\rho_{22} = \frac{4|g|^2}{\Omega^2}\sin^2\left(\frac{\Omega t}{2}\right), \tag{1.41}$$

$$\rho_{21} = \frac{2g}{\Omega^2}\sin\left(\frac{\Omega t}{2}\right)\left\{-\Delta\sin\left(\frac{\Omega t}{2}\right) + i\Omega\cos\left(\frac{\Omega t}{2}\right)\right\}, \tag{1.42}$$

where $\Omega = \{\Delta^2 + 4|g|^2\}^{1/2}$.

If atom is at resonance with the applied field ($\Delta = 0$), then $\Omega = 2|g|$ and above Eqs. (1.41) and Eqs. (1.42) simplifies to

$$\rho_{22} = \sin^2(|g|t) \tag{1.43}$$

$$\rho_{21} = \frac{ig}{|g|}\sin\left(\frac{|g|t}{2}\right)\cos\left(\frac{|g|t}{2}\right) = \frac{ig}{2|g|}\sin(|g|t)\ . \tag{1.44}$$

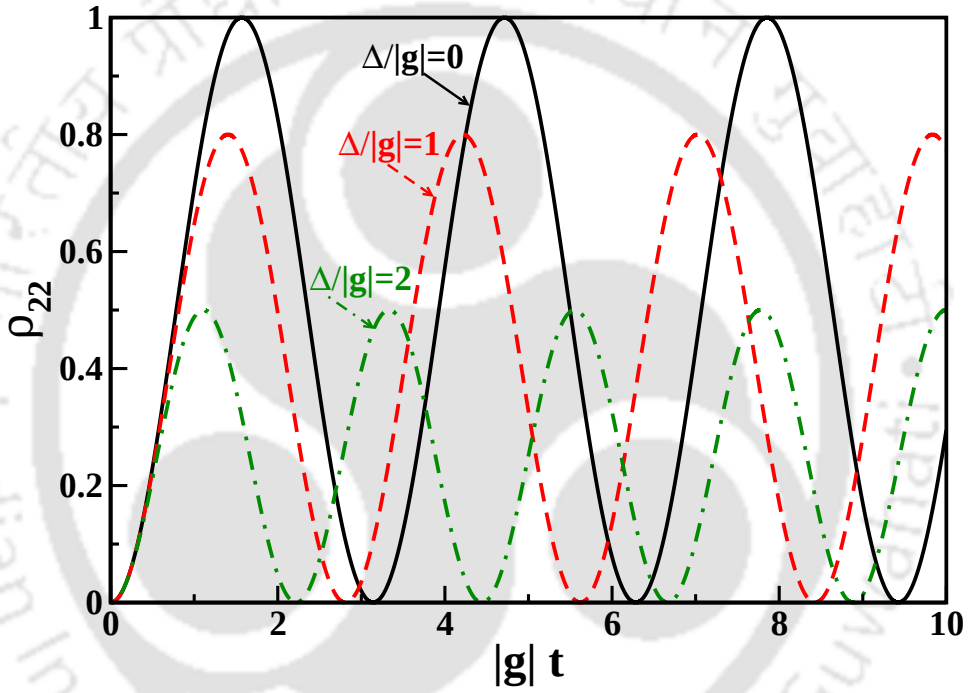

FIGURE 1.2: The Rabi oscillation of the excited state population ρ_{22} as a function of normalized interaction time for three values of normalized field detuning indicated against the plots.

Fig. 1.2 illustrates the time dependence of the population ρ_{22} for various values of $\Delta/|g|$. At the resonance, $\Delta = 0$, the population ρ_{22} of the excited state oscillates symmetrically at frequency $2|g|$ between zero and one (see black solid line in Fig. 1.2). These oscillations are known as the optical Rabi oscillations and frequency $2|g|$ is called the Rabi frequency. This atomic oscillation is equivalent to the problem of a spin-1/2 system with two possible states first discovered by Rabi [95]. In his model, Rabi shows that a spin-1/2 particle undergoes the so-called Rabi oscillations between the spin-up and spin-down states when subjected to an

oscillatory magnetic field. For a finite value of field detuning, the angular frequency of the population oscillation changes to $\Omega = \{\Delta^2 + |g|^2\}^{1/2}$. This detuning dependent frequency is called the generalized Rabi frequency. Thus, as we increase the detuning Δ of the laser field, the angular frequency of population oscillation increases while the amplitude of the oscillation is attenuated as shown in Fig. 1.2.

Next, we calculate the induced dipole moment for a single two-level atom which is in the ground state $|1\rangle$ at time t=0. This is done by taking the expectation value of the atomic dipole moment operator $\hat{\mathbf{d}}$,

$$\begin{aligned} \langle \hat{\mathbf{d}}(\mathbf{r}) \rangle &= \mathrm{Tr}(\rho \hat{\mathbf{d}}) \\ &= (\rho_{21}\, e^{-i\omega t} \mathbf{d}_{12} + \text{c.c.})\,, \end{aligned} \tag{1.45}$$

where $\rho_{21}\, e^{-i\omega t}$ has been used in the original frame of reference. The simplified form of coherence ρ_{21} from Eq. (1.42) is given by

$$\begin{aligned} \rho_{21} &= \frac{2|g|}{\Omega^2}\left\{-\frac{\Delta}{2} + \frac{\Delta}{2}\cos(\Omega t) + \frac{i\Omega}{2}\sin(\Omega t)\right\} \\ &= \frac{2|g|}{\Omega^2}\left\{-\frac{\Delta}{2} + \frac{\Delta}{2}\left(\frac{e^{i\Omega t} + e^{-i\Omega t}}{2}\right) + \frac{i\Omega}{2}\left(\frac{e^{i\Omega t} - e^{-i\Omega t}}{2i}\right)\right\} \\ &= \frac{2|g|}{\Omega}\left\{-\frac{\Delta}{2\Omega} + \frac{1}{4}\left(\frac{\Delta}{\Omega} + 1\right)e^{i\Omega t} + \frac{1}{4}\left(\frac{\Delta}{\Omega} - 1\right)e^{-i\Omega t}\right\}. \end{aligned} \tag{1.46}$$

Substituting above coherence ρ_{21} from Eq. (1.46) into Eq. (1.45), we get

$$\langle \hat{\mathbf{d}}(\mathbf{r}) \rangle = \frac{2|g|}{\Omega}\left\{-\frac{\Delta}{2\Omega}\, e^{-i\omega t} + \frac{1}{4}\left(\frac{\Delta}{\Omega} + 1\right) e^{-i(\omega-\Omega)t} + \frac{1}{4}\left(\frac{\Delta}{\Omega} - 1\right) e^{-i(\omega+\Omega)t}\right\} + \text{c.c.}\,. \tag{1.47}$$

This equation shows that the atomic dipole moment oscillates not only at the frequency ω of the external applied field but also at the Rabi sideband frequencies $\omega - \Omega$ and $\omega + \Omega$. Next we examine some of the properties of a two-level atom in the dressed state picture via diagonalizing the Hamiltonian given in Eq. (1.35).

1.2.3 Dressed state analysis of the two-level atom

The matrix representation of the rotating frame Hamiltonian of Eq. (1.35) by assuming the original eigenstates $|1\rangle$ and $|2\rangle$ of the atom as the basis vectors can be written as

$$\mathcal{H} = \hbar \begin{bmatrix} 0 & g^* \\ g & \Delta \end{bmatrix}$$

However, the presence of the off-diagonal elements shows that the original eigenstates $|1\rangle$ and $|2\rangle$ of the free atom are no longer the eigenstates of the atom-field system. It can be readily verified by diagonalizing $\mathcal{H}$ that the new eigenstates are a coherent superposition of $|1\rangle$ and $|2\rangle$. We therefore Diagonalize this Hamiltonian to extract its new eigenvalues and corresponding eigenstates. The eigenstates are

$$|\alpha\rangle = \sin\theta\,|1\rangle + \cos\theta|2\rangle \tag{1.48}$$

$$|\beta\rangle = \cos\theta\,|1\rangle - \sin\theta\,|2\rangle\,, \tag{1.49}$$

where mixing angle is given by $\tan(2\theta) = g/\Delta$. Thus it is evident that the presence of strong laser field the atomic levels $|1\rangle$ and $|2\rangle$ split into sub-levels. The corresponding energy eigenvalues to the dressed states $|\alpha_+\rangle$ and $|\alpha_-\rangle$ are given by

$$E_+ = \frac{\hbar}{2}\left[\Delta + \Omega\right]\,, \tag{1.50}$$

$$E_- = \frac{\hbar}{2}\left[\Delta - \Omega\right]\,, \tag{1.51}$$

where $\Omega = \sqrt{\Delta^2 + 4|g|^2}$ is the generalized Rabi frequency. This shift in the energy from the bare atomic states $|1\rangle$ and $|2\rangle$ is called the AC Stark shift. This energy shift will play a crucial role in some of the later discussions in this chapter. In case of a weak incident field, i.e., for $|g| << \Delta$, the mixing angle will be smaller and thus the dressed states are closer to the bare atomic states. At the atomic resonance condition $\Delta = 0$, $\theta = \pi/4$ and $E_\pm = \hbar|g|$. In this case, there is perfect superposition of the two bare states $|1\rangle$ and $|2\rangle$ given as

$$|\alpha\rangle = \frac{1}{\sqrt{2}}(|1\rangle - |2\rangle)\,, \tag{1.52}$$

$$|\beta\rangle = \frac{1}{\sqrt{2}}(|1\rangle + |2\rangle)\,. \tag{1.53}$$

In such a case, the atom spends equal time in the excited and ground states. This simply means that the population is being equally distributed between the ground and excited states instead of resting mostly in the ground state. This situation results in the reduced absorption of the laser field.

So far we have discussed the dynamics of a two-level atom in the absence of relaxation processes. The relaxation processes are usually ignored for very short pulses whose duration is much less than the relaxation times. The relaxation processes include decay of the excited atomic levels due to spontaneous emission and collisions. We will see that the population in the respective levels will reach at a steady state value in the presence of damping effects, and consequently, the Rabi oscillations will be damped out.

1.2.4 Transient and steady state response of two-level atoms

We study the damping effects by adding decay terms to the equation Eq. (1.38) phenomenologically. Thus the modified Liouville's equation for the density operator is given by

$$\dot{\rho} = -\frac{i}{\hbar}\left[\hat{\mathcal{H}}, \rho\right] + \mathcal{L}_{\gamma}\rho\,, \tag{1.54}$$

where the last term describing spontaneous decay and dephasing of dipole moment is given by Liouvillean operator

$$\begin{aligned}\mathcal{L}_{\gamma}\rho = &-\gamma\left(|2\rangle\langle 2|\rho - 2|1\rangle\langle 1|\rho_{22} + \rho|2\rangle\langle 2|\right)\\ &-\gamma_c\left(|2\rangle\langle 2|\rho - 2|2\rangle\langle 2|\rho_{22} + \rho|2\rangle\langle 2|\right)\,.\end{aligned} \tag{1.55}$$

The spontaneous decay rate γ originates due to the finite lifetime of the excited state $|2\rangle$ and is consequence of uncertainty relation in energy and time $\Delta\omega\Delta t \geq 1$. Collisional decay rate γ_c arises due to elastic and inelastic collisions between atoms via shortening the life time of coherence and populations, respectively. Elastic collisions are dominant part of line-broadening effects in gaseous media and hence, we limit our consideration to the elastic variety of collisions.

By incorporating the decay and collisional rates, the optical Bloch equations are written as

$$\dot{\rho}_{22} = -2\gamma\rho_{22} + ig\rho_{12} - ig^*\rho_{21}\,, \tag{1.56}$$

$$\dot{\rho}_{11} = 2\gamma\rho_{22} - ig\rho_{12} + ig^*\rho_{21}\,, \tag{1.57}$$

$$\dot{\rho}_{21} = -[\Gamma + i\Delta]\rho_{21} + ig(\rho_{11} - \rho_{22})\,, \tag{1.58}$$

$$\dot{\rho}_{12} = -[\Gamma - i\Delta]\rho_{12} - ig^*(\rho_{11} - \rho_{22})\,. \tag{1.59}$$

where 2γ is the radiative damping rate at which population decays spontaneously from the excited state $|2\rangle$ to the ground state $|1\rangle$. While Γ $(= \gamma + \gamma_c)$ is the dephasing rate of the coherence ρ_{12} and it is sum of radiative and collisional rates. These damping constants are sometimes expressed in terms of relaxation times as

$$2\gamma = 1/T_1, \;\; \Gamma = 1/T_2\,, \tag{1.60}$$

where T_1 and T_2 are known as the longitudinal and transverse relaxation times.

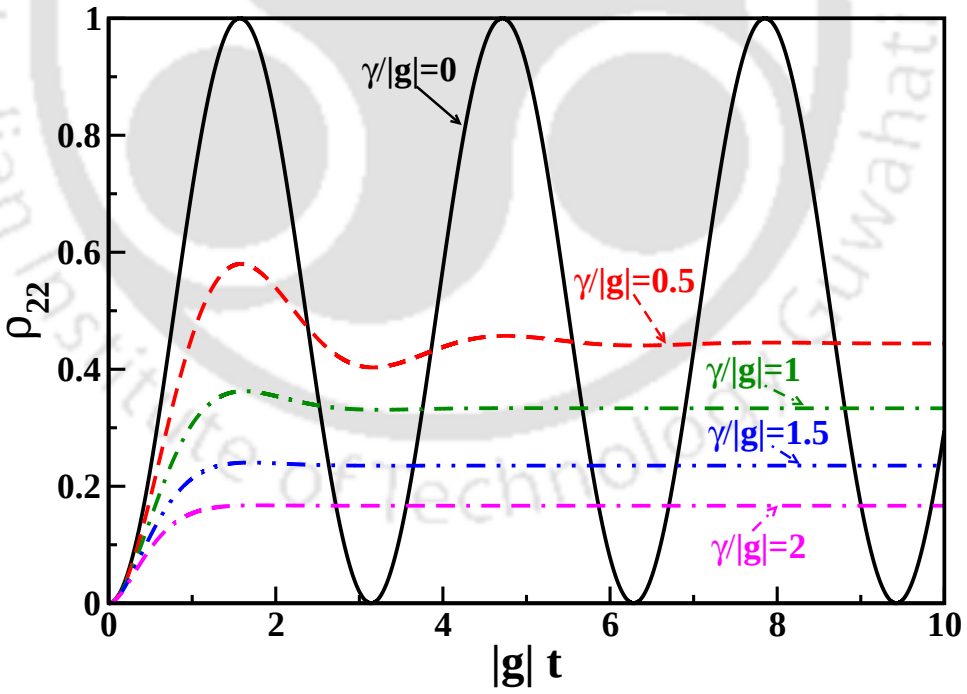

FIGURE 1.3: Damped Rabi oscillations. The excited state population ρ_{22} as a function of interaction time at $\Delta = 0$ for different values of normalized radiative decay rate γ.

In the absence of collisional dephasing rate, $\Gamma = \gamma$ and at atomic resonance $\Delta = 0$, the transient solution of Eqs. (1.56)- (1.59) for population ρ_{22}, under the initial condition $\rho_{22} = 0$ and $\rho_{12} = 0$, is given by

$$\rho_{22} = \frac{|g|^2}{\gamma + 2|g|^2}\left\{1 - \left[\cos(\lambda t) + \frac{3\gamma}{2\lambda}\sin(\lambda t)\right]\exp(-3\gamma t/2)\right\} \tag{1.61}$$

where $\lambda = \{4|g|^2 - \gamma^2/4\}^{1/2}$. Fig. 1.3 shows the time-dependent behavior of excited state population ρ_{22} for the atoms initially in their ground states. In the absence of radiative decay ($\gamma = 0$), the population oscillates sinusoidally which shows the pure Rabi oscillations. For a finite value of decay rate ($\gamma \neq 0$), all curves approach to a saturation value. At a higher value of γ, the oscillation are damped out more rapidly as depicted in Fig. 1.3. It is also evident from Fig. 1.3 that the population will eventually reach some steady state value.

Thus, in presence of damping effects, the solutions of optical Block equations (1.56)-(1.59) are no longer purely oscillatory. The system now comes into steady state after a substantial longer period of time as compared to relaxation time. Therefore, we seek the solutions of optical Block equations in the steady state condition. The steady state solutions are found by setting all rates of change in Eqs. (1.56)-(1.59) equal to zero and solving them algebraically. The results are given by

$$\rho_{22} = \frac{\Gamma|g|^2}{\gamma(\Delta^2 + \Gamma^2) + 2\Gamma|g|^2} \tag{1.62}$$

$$\rho_{21} = \frac{ig\gamma(\Gamma - i\Delta)}{\gamma(\Delta^2 + \Gamma^2) + 2\Gamma|g|^2}\,. \tag{1.63}$$

The induced polarization for an ensemble of atoms with number density $\mathcal{N}$ and dipole operator $\hat{\mathbf{d}}(\mathbf{r})$ between the level $|1\rangle$ and $|2\rangle$ is defined by

$$\mathbf{P} = \mathcal{N}\langle\hat{\mathbf{d}}(\mathbf{r})\rangle = \mathcal{N}\mathrm{Tr}(\rho\hat{\mathbf{d}}) \tag{1.64}$$

$$\mathbf{P} = \mathcal{N}(\rho_{21}\, e^{-i\omega t}\mathbf{d}_{12} + \rho_{12}\, e^{i\omega t}\mathbf{d}_{21}) \tag{1.65}$$

Now we proceed to find out the susceptibility of the medium. For this purpose, we express the susceptibility as the constant of proportionality relating **P** and **E**. In the following we discuss how this thing can be achieve in details.

1.2.5 Linear and nonlinear susceptibility of the medium

We calculate the polarization in terms of electric field in the following way. Since the electrostatic field due to nucleus is stronger than the external applied field, the perturbative approach is sufficient to describe the atom-filed interaction. Therefore, we need to write the induced polarization in the form of Taylor expansion to all orders in external electric field **E**

$$P_\alpha = P_\alpha|_{E=0} + \sum_\beta \left(\frac{\partial P_\alpha}{\partial E_\beta}\right)\Big|_{E=0} E_\beta + \frac{1}{2!}\sum_{\beta,\gamma}\left(\frac{\partial^2 P_\alpha}{\partial E_\beta \partial E_\gamma}\right)\Big|_{E=0} E_\beta E_\gamma + ... \tag{1.66}$$

where subscript α denotes one component of polarization ($\alpha = x$ or y or z) whereas indices β and γ etc. indicates sum over all x, y and z for each α in Cartesian coordinate system. The first term of this equation corresponds to polarization due to the permanent dipole moment of the medium in the absence of external electric field. In the absence of any perturbing forces, an atom is assumed to be spherically symmetric. Therefore, the zeroth order term vanishes for a system under our consideration. The second term of Eq. (1.66) represents the induced linear polarization. The single partial derivative in the bracket with summation is called linear susceptibility χ. The higher order susceptibility term can be found in the subsequent terms. These are important only if electric field intensity is very strong. In principle, polarization response of medium at a given point $\mathbf{r}$ at moment t depends on the electric field at all other points $\mathbf{r}'$ at all earlier moments of time t'. Therefore, χ must be expressed in such a manner that it has zero value for $t - t' < 0$ in order to preserve causality and nonzero value for $\mathbf{r} \neq \mathbf{r}'$ which is called a nonlocal response. Keeping this fact in mind, we truncate above expansion after the first order term and concentrate on the linear polarization which can be expressed as

$$\mathbf{P}_\alpha(\mathbf{r}, t) = \sum_\beta \int_{-\infty}^{t}\int_{-\infty}^{+\infty} dt' d^3r' \chi_{\alpha\beta}(\mathbf{r} - \mathbf{r}', t - t')\mathbf{E}_\beta(\mathbf{r}', t')\,, \tag{1.67}$$

where $\chi_{\alpha\beta}$ is the linear dielectric susceptibility tensor of rank two in an anisotropic medium where response of the medium is different for different components of the electric field. For isotropic medium, the polarization is aligned with and proportional to the electric field. This implies that the complex susceptibility is direction independent and should be treated as a scalar quantity, i.e, $\chi_{\alpha\beta} = \chi$. Hence, for a linear homogeneous and isotropic dielectric medium

as in the present thesis work, the polarization can be written as

$$\mathbf{P}(\mathbf{r},t) = \int_{-\infty}^{t} dt' \chi(t-t')\mathbf{E}(\mathbf{r},t')\,. \tag{1.68}$$

The electric field associated with an electromagnetic wave is given by

$$\mathbf{E}(\mathbf{r},t) = \hat{\mathbf{e}}\mathcal{E}_0(\mathbf{r},t)\, e^{i(\mathbf{k}\cdot\mathbf{r}-\omega t)} + \text{c.c.}\,. \tag{1.69}$$

Using this definition of electric field in Eq. (1.68), we get

$$\mathbf{P}(\mathbf{r},t) = \hat{\mathbf{e}} \int_{-\infty}^{t} dt' \chi(t-t')\mathcal{E}_0(\mathbf{r},t')\, e^{i(\mathbf{k}\cdot\mathbf{r}-\omega t')} + \text{c.c.}\,. \tag{1.70}$$

We assume that the electric field is a continuous wave, thus the field amplitude $\mathcal{E}_0(\mathbf{r},t')$ is time-independent. Therefore, polarization for long interaction time can be expressed as

$$\mathbf{P}(\mathbf{r},t) = \hat{\mathbf{e}} \int_{-\infty}^{\infty} dt' \chi(t-t')\mathcal{E}_0(\mathbf{r})\, e^{i(\mathbf{k}\cdot\mathbf{r}-\omega t)}\, e^{i\omega(t-t')} + \text{c.c.}\,. \tag{1.71}$$

Using a transformation $t - t' = \tau$ in Eq. (1.68), we get

$$\mathbf{P}(\mathbf{r},t) = \hat{\mathbf{e}} \int_{-\infty}^{\infty} d\tau \chi(\tau)\, e^{i\omega(\tau)}\mathcal{E}_0(\mathbf{r})\, e^{i(\mathbf{k}\cdot\mathbf{r}-\omega t)} + \text{c.c.}\,, \tag{1.72}$$

where Fourier transform of susceptibility can be expressed as

$$\chi(\omega) = \int_{-\infty}^{+\infty} d\tau \chi(\tau)\, e^{i\omega(\tau)}\,. \tag{1.73}$$

Using above definition of susceptibility, the polarization can be written as

$$\mathbf{P}(\mathbf{r},t) = \hat{\mathbf{e}}\chi(\omega)\mathcal{E}_0(\mathbf{r})\, e^{i(\mathbf{k}\cdot\mathbf{r}-\omega t)} + \text{c.c.} = \chi(\omega)\mathbf{E}(\mathbf{r},t)\,. \tag{1.74}$$

Comparing Eqs. (1.65) and (1.74), the susceptibility of a two-level system is expressed as

$$\chi_{21}(\omega) = \frac{\mathcal{N}|d_{12}|^2}{\hbar} \frac{i\gamma(\Gamma - i\Delta)}{\gamma(\Delta^2+\Gamma^2) + 2\Gamma|g|^2}\,. \tag{1.75}$$

Note that this expression of susceptibility contains both the linear as well as nonlinear contributions instead of only linear contribution. This is because the field strength is already present in the Rabi frequency $|g|$ in the denominator. For better understanding, it is beneficial to break

the complex susceptibility into its real and imaginary components which is given by

$$\mathrm{Re}[\chi_{21}(\omega)] = \frac{\mathcal{N}|d_{12}|^2}{\hbar} \frac{\Delta}{(\Delta^2 + \Gamma^2) + 2(\Gamma/\gamma)|g|^2} . \tag{1.76}$$

$$\mathrm{Im}[\chi_{21}(\omega)] = \frac{\mathcal{N}|d_{12}|^2}{\hbar} \frac{\Gamma}{(\Delta^2 + \Gamma^2) + 2(\Gamma/\gamma)|g|^2} . \tag{1.77}$$

The real part $\mathrm{Re}[\chi_{21}(\omega)]$ gives the dispersion of the medium. The dependence of dispersion on the field detuning for three different values of field intensity is plotted in Fig. 1.4(b). We can see from Fig. 1.4(b) that it has a standard anomalous dispersive kind of lineshape even in the presence of an intense laser field.

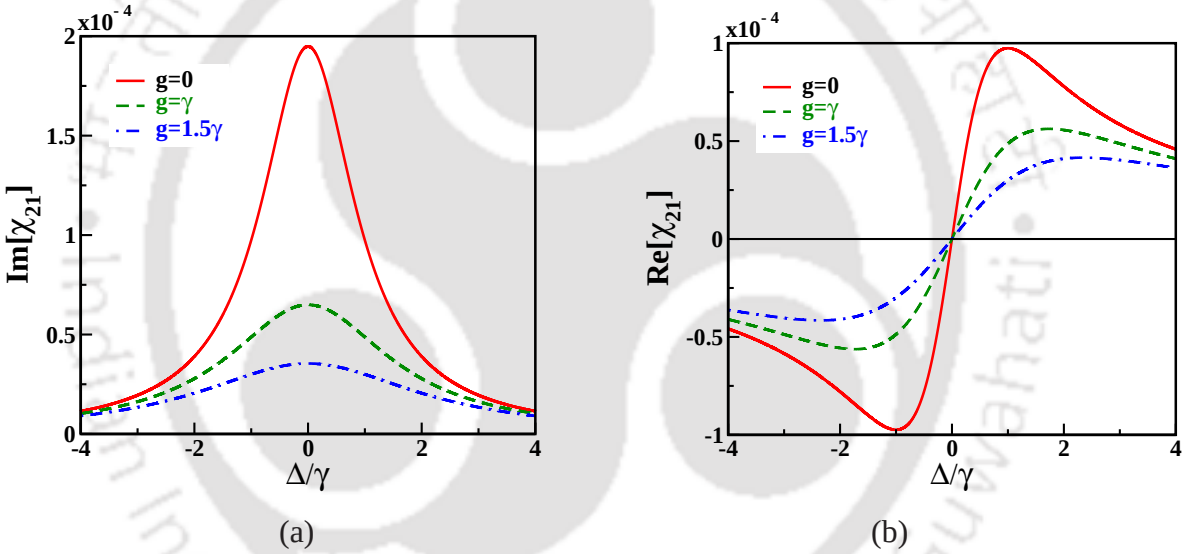

FIGURE 1.4: The susceptibility of laser field as a function of normalized detuning Δ/γ. (a) Imaginary ($\mathrm{Im}[\chi]$) part gives absorption and (b) real ($\mathrm{Re}[\chi]$) part describes dispersion. The other parameters are $\gamma = 3\pi \times 10^6$rad/sec, $\lambda = 795$ nm, and $\mathcal{N} = 5{\times}10^{11}$ atoms/cm^3.

The imaginary part $\mathrm{Im}[\chi_{21}(\omega)]$ is related to the absorption coefficient of the medium. The linewidth (full width at half maximum) of the absorption spectrum is given by

$$\delta = 2\{\Gamma^2 + 2(\Gamma/\gamma)|g|^2\}^{1/2} . \tag{1.78}$$

This clearly shows that the linewidth depends on radiative and collisional decay rates as well as intensity of laser field. The effect of intensity of laser field on the absorption lineshape is

illustrated in Fig. 1.4(a). The width of spectral profile continues to broaden with increasing intensity of the field. This tendency of broadening of spectral line with intensity is known as power broadening. It is clear from Fig. 1.4(a) that the power broadening becomes more pronounce for high intensity of laser beams. Interestingly, the value of absorption in the line center is almost saturated with respect to its weak field value. Therefore, the presence of intense laser fields leads to saturation effects. This phenomenon is known as saturation broadening [96]. Thus the saturation effect reduces the rate of absorption or attenuation of the incident laser field. In the weak field limit, the real and imaginary parts of linear susceptibility takes usual form

$$\mathrm{Re}[\chi_{21}(\omega)] = \frac{\mathcal{N}|d_{12}|^2}{\hbar}\frac{\Delta}{(\Delta^2+\Gamma^2)}\,. \tag{1.79}$$

$$\mathrm{Im}[\chi_{21}(\omega)] = \frac{\mathcal{N}|d_{12}|^2}{\hbar}\frac{\Gamma}{(\Delta^2+\Gamma^2)}\,. \tag{1.80}$$

Thus for a fairly weak light beams the absorption line has a perfect Lorentzian shape where power broadening is negligible (see solid red curve in Fig. 1.4(a). The linewidth of the absorption line in this case reduces to a simple addition of the radiative and collisional decay rates ($2\Gamma = 2\gamma + 2\gamma_c$). The refractive index n of the medium is connected with the real part of the susceptibility by the following relation

$$\begin{aligned} n &= \sqrt{1 + 4\pi\mathrm{Re}[\chi_{21}(\omega)]} \\ &= 1 + 2\pi\mathrm{Re}[\chi_{21}(\omega)] \qquad \text{if } \mathrm{Re}[\chi_{21}] << 1\,. \end{aligned} \tag{1.81}$$

For the maximum value of refractive index n, the real part $\mathrm{Re}[\chi_{21}(\omega)]$ should be maximum. The real part $\mathrm{Re}[\chi_{21}(\omega)]$ is maximum at $\Delta = \Gamma$. However, the high index can not be utilized since the imaginary part of susceptibility is very large at this point. Thus a laser beam tuned close to an atomic resonance of a two-level atomic system always suffers from huge absorption. The large absorption prevents the propagation of laser beams inside the resonant medium. However, one can get zero absorption with high refractive index by using atomic coherence and interference effects in an ensemble of phase coherent atoms. The ensemble of such atoms is a new state matter know as phaseonium [97]. Such a high refractive index would require 1 Torr pressure in a gaseous medium [98]. Moreover, the other processes such as Doppler broadening, collisions and number of fluctuations influence the coherence and thus

limiting the scheme for practical realization. The well known saturation absorption technique is used in order to get rid of from this large absorption [99, 100]. In this technique an extra strong field is applied which takes medium into a saturation stage and protects the weak laser beam. MacCall and Hahn experimentally demonstrated that an electromagnetic pulse having area between π and 2π can propagate shape invariant through a resonant two-level absorptive medium [101]. This phenomenon where a single pulse creates transparency for itself is known as *self induced transparency* (SIT) [102, 103].

The emphasize of the present thesis is to deal with continuous wave laser beams instead of light pulses. Therefore, the multilevel systems are exploited to fulfill the need, i.e., the vanishing of absorption with high refractive index. A dramatic modification in the absorption and dispersion properties of a coherent medium has been seen when these multilevel systems interact with more than one laser field. In the following, we discuss the interaction of a three-level atom with two laser fields.

1.3 Interaction of light with a system of three-level atoms

We consider an isotropic homogeneous gas medium composed of rubidium atoms. Each atom is modeled in three-level Λ-configuration as shown in Fig. 1.5. A single excited state $|3\rangle$ is coupled with two closely spaced ground metastable states $|1\rangle$ and $|2\rangle$ via two optical fields. A weak probe field of frequency ω_p couples the dipole allowed transition $|3\rangle \leftrightarrow \langle 1|$ and a strong control field of frequency ω_c drives the dipole allowed transition $|3\rangle \leftrightarrow \langle 2|$. The direct optical coupling between the two ground sublevels is not possible due to parity constraints. In other words, the transition $|2\rangle \leftrightarrow \langle 1|$ is an electric dipole forbidden transition. The excited state $|3\rangle$ decays spontaneously to the states $|1\rangle$ and $|2\rangle$ at the rates $2\gamma_1$ and $2\gamma_2$, respectively. The probe and control fields are given respectively as

$$\mathbf{E}_p(\mathbf{r},t) = \hat{\mathbf{e}}_p \mathcal{E}_p(\mathbf{r})\, e^{i(\mathbf{k}_p\cdot\mathbf{r}-\omega_p t)} + \text{c.c.}\,, \tag{1.82}$$

$$\mathbf{E}_c(\mathbf{r},t) = \hat{\mathbf{e}}_c \mathcal{E}_c(\mathbf{r})\, e^{i(\mathbf{k}_c\cdot\mathbf{r}-\omega_c t)} + \text{c.c.}\,, \tag{1.83}$$

where $\mathcal{E}_p(\mathbf{r})$, $\mathcal{E}_c(\mathbf{r})$ are the slowing varying envelope functions; $\hat{\mathbf{e}}_p$, $\hat{\mathbf{e}}_c$ are the unit polarization vectors, and $\mathbf{k}_p$, $\mathbf{k}_c$ are the wave vectors of probe and control fields, respectively. Note that the

complex conjugate (c.c.) term has been added in above two equations to make electric fields as real quantity.

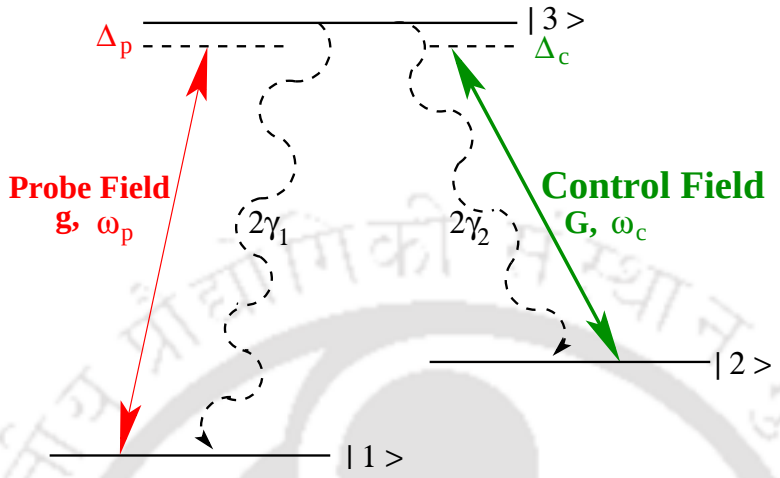

FIGURE 1.5: The energy level diagram of three-level rubidium atom in Λ-configuration. The atomic system is driven by two laser fields. A weak probe field of Rabi frequency g is coupled to transition $|3\rangle \leftrightarrow \langle 1|$. A strong control field of Rabi frequency G drives the transition $|3\rangle \leftrightarrow \langle 2|$. The transitions $|3\rangle \leftrightarrow \langle 1|$ and $|3\rangle \leftrightarrow \langle 2|$ are electric dipole allowed transitions while the transition $|2\rangle \leftrightarrow \langle 1|$ is an electric dipole forbidden transition.

The total Hamiltonian of three-level Λ-system interacting with optical fields under electric dipole approximation is given by

$$\hat{H} = \hat{H}_0 + \hat{H}_I\,, \tag{1.84}$$

where $\hat{H}_0$ is unperturbed Hamiltonian of the atom and $\hat{H}_I$ is the interaction Hamiltonian between the atom and optical fields. The expression for unperturbed Hamiltonian is written as

$$\hat{H}_0 = \hbar\omega_{31}|3\rangle\langle 3| + \hbar\omega_{21}|2\rangle\langle 2|\,, \tag{1.85}$$

where $\hbar\omega_{31}$ is the energy of the excited state $|3\rangle$ and $\hbar\omega_{21}$ is the energy of metastable state $|2\rangle$ relative to the ground state $|1\rangle$. We have assumed that the ground level $|1\rangle$ has zero energy. The interaction Hamiltonian between the atom and the external classical electric fields can be expressed as

$$\hat{H}_I = -(|3\rangle\langle 1|\mathbf{d}_{31}\cdot\mathbf{E_p} + |3\rangle\langle 2|\mathbf{d}_{32}\cdot\mathbf{E_c} + \text{H.c.})\,, \tag{1.86}$$

where $\mathbf{d}_{31}(\mathbf{d}_{32})$ and $\mathbf{E_p}$ ($\mathbf{E_c}$) are denoting the atomic dipole matrix element and applied external electric field between the states $|3\rangle$ and $|1\rangle(|2\rangle)$. The abbreviation "H.c." stands for the Hermitian conjugate of the preceding expression is to be added. The explicit form of interaction Hamiltonian including electric fields expressions can be rewritten as

$$\begin{aligned}\hat{H}_I = &-\Big[\mathbf{d}_{31}\cdot\hat{\mathbf{e}}_p\mathcal{E}_p(\mathbf{r})\,e^{i(\mathbf{k}_p\cdot\mathbf{r}-\omega_p t)} + \mathbf{d}_{31}\cdot\hat{\mathbf{e}}_p\mathcal{E}_p^*(\mathbf{r})\,e^{-i(\mathbf{k}_p\cdot\mathbf{r}-\omega_p t)}\Big]|3\rangle\langle 1| \\ &-\Big[\mathbf{d}_{31}^*\cdot\hat{\mathbf{e}}_p\mathcal{E}_p(\mathbf{r})\,e^{i(\mathbf{k}_p\cdot\mathbf{r}-\omega_p t)} + \mathbf{d}_{31}^*\cdot\hat{\mathbf{e}}_p\mathcal{E}_p^*(\mathbf{r})\,e^{-i(\mathbf{k}_p\cdot\mathbf{r}-\omega_p t)}\Big]|1\rangle\langle 3| \\ &-\Big[\mathbf{d}_{32}\cdot\hat{\mathbf{e}}_c\mathcal{E}_c(\mathbf{r})\,e^{i(\mathbf{k}_c\cdot\mathbf{r}-\omega_c t)} + \mathbf{d}_{32}\cdot\hat{\mathbf{e}}_c\mathcal{E}_c^*(\mathbf{r})\,e^{-i(\mathbf{k}_c\cdot\mathbf{r}-\omega_c t)}\Big]|3\rangle\langle 2| \\ &-\Big[\mathbf{d}_{32}^*\cdot\hat{\mathbf{e}}_c\mathcal{E}_c(\mathbf{r})\,e^{i(\mathbf{k}_c\cdot\mathbf{r}-\omega_c t)} + \mathbf{d}_{32}^*\cdot\hat{\mathbf{e}}_c\mathcal{E}_c^*(\mathbf{r})\,e^{-i(\mathbf{k}_c\cdot\mathbf{r}-\omega_c t)}\Big]|2\rangle\langle 3|\,, \end{aligned} \tag{1.87}$$

where "$*$" denotes the complex conjugate.

Defining the new quantities as

$$g = \frac{\mathbf{d}_{31}\cdot\hat{\mathbf{e}}_p\mathcal{E}_p}{\hbar}\,e^{i\mathbf{k}_p\cdot\mathbf{r}}\,, \tilde{g} = \frac{\mathbf{d}_{31}\cdot\hat{\mathbf{e}}_p\mathcal{E}_p^*}{\hbar}\,e^{-i\mathbf{k}_p\cdot\mathbf{r}}\,; \tag{1.88}$$

$$G = \frac{\mathbf{d}_{32}\cdot\hat{\mathbf{e}}_c\mathcal{E}_c}{\hbar}\,e^{i\mathbf{k}_p\cdot\mathbf{r}}\,, \tilde{G} = \frac{\mathbf{d}_{32}\cdot\hat{\mathbf{e}}_c\mathcal{E}_c^*}{\hbar}\,e^{-i\mathbf{k}_p\cdot\mathbf{r}}\,, \tag{1.89}$$

where $g(\tilde{g})$ and $G(\tilde{G})$ are known as the Rabi frequencies (counter-rotating frequencies) for probe and control fields, respectively. Note that under dipole approximation, the spatial phase factors appearing in definitions of Rabi frequencies are treated to be unity. Introducing above parameters in Eq. (1.87) for the interaction Hamiltonian, we get

$$\begin{aligned}\hat{H}_I = &-\hbar\Big[g\,e^{-i\omega_p t} + \tilde{g}\,e^{i\omega_p t}\Big]|3\rangle\langle 1| - \hbar\Big[\tilde{g}^*\,e^{-i\omega_p t} + g^*\,e^{i\omega_p t}\Big]|1\rangle\langle 3| \\ &-\hbar\Big[G\,e^{-i\omega_c t} + \tilde{G}\,e^{i\omega_c t}\Big]|3\rangle\langle 2| - \hbar\Big[\tilde{G}^*\,e^{-i\omega_c t} + G^*\,e^{i\omega_c t}\Big]|2\rangle\langle 3|\,. \end{aligned} \tag{1.90}$$

We consider a unitary transformation

$$|\psi(\mathbf{r},t)\rangle = e^{-i[\omega_p|3\rangle\langle 3| + (\omega_p-\omega_c)|2\rangle\langle 2|]t}|\phi(\mathbf{r},t)\rangle\,. \tag{1.91}$$

Using Schrodinger's equation one can obtain

$$i\hbar\frac{\partial}{\partial t}|\phi(\mathbf{r},t)\rangle = \hat{H}_{eff}|\phi(\mathbf{r},t)\rangle\,, \tag{1.92}$$

where $\hat{H}_{eff}$ is an effective Hamiltonian and it is given by

$$\hat{H}_{eff} = U^{\dagger}(\hat{H}_0 + \hat{H}_I)U - \hbar(\omega_p|3\rangle\langle 3| + (\omega_p - \omega_c)|2\rangle\langle 2|)\,. \tag{1.93}$$

Here U is a unitary transformation which is defined by

$$U = e^{-i[\omega_p|3\rangle\langle 3|+(\omega_p-\omega_c)|2\rangle\langle 2|]t}\,. \tag{1.94}$$

The unperturbed Hamiltonian doesn't not change under this unitary transformation as one can verify easily

$$U^{\dagger}(H_0)U = \hbar\omega_{31}|3\rangle\langle 3| + \hbar\omega_{21}|2\rangle\langle 2|\,. \tag{1.95}$$

Under the unitary transformation, the interaction Hamiltonian takes new form

$$\begin{aligned} U^{\dagger}\hat{H}_I U = &-\hbar\left[g + \tilde{g}\, e^{2i\omega_p t}\right]|3\rangle\langle 1| - \hbar\left[\tilde{g}^{*}\, e^{-2i\omega_p t} + g^{*}\right]|1\rangle\langle 3| \\ &- \hbar\left[G + \tilde{G}\, e^{2i\omega_c t}\right]|3\rangle\langle 2| - \hbar\left[\tilde{G}^{*}\, e^{-2i\omega_c t} + G^{*}\right]|2\rangle\langle 3|\,. \end{aligned} \tag{1.96}$$

In this equation, the rapidly oscillating terms at frequency $\pm 2\omega_p(\pm 2\omega_c)$ will give zero value on an average in any appreciable time scale as compared to without oscillating terms because $\tilde{g} \ll 2\omega_p$ and $\tilde{G} \ll 2\omega_c$ in an optical frequency domain. The terms related to $\tilde{g}$ and $\tilde{G}$ will be important only if $\tilde{g} \approx 2\omega_p$ and $\tilde{G} \approx 2\omega_c$ along with their complex conjugates, respectively. Therefore, we neglect these rapidly oscillating terms while retaining the dc terms. This approximation is known as the "*rotating-wave approximation*" (RWA). The effective Hamiltonian for the system of interest in the appropriate rotating frame can be written as

$$\hat{H}_{eff} = \hbar\Delta_p|3\rangle\langle 3| + \hbar(\Delta_p - \Delta_c)|2\rangle\langle 2| - \hbar(g|3\rangle\langle 1| + G|3\rangle\langle 2| + \text{H.c.})\,, \tag{1.97}$$

where $\Delta_p = \omega_{31} - \omega_p$ and $\Delta_c = \omega_{32} - \omega_c$ are the one-photon detunings of the probe and control fields from the respective transitions. The two-photon Raman detuning is defined as $\Delta = \Delta_p - \Delta_c$, which involves two different frequencies to transfer an atom from ground state $|1\rangle$ to state $|2\rangle$ via third state $|3\rangle$ through Raman process. We further use this effective Hamiltonian $\hat{H}_{eff}$ in the Liouville equation to study the dynamics of three-level Λ-system.

1.3.1 The Liouville equation for a three-level Λ-system

We study equation of motion for the density matrix elements by the Liouville Equation:

$$\dot{\rho} = -\frac{i}{\hbar}\left[\hat{H}_{eff}, \rho\right] + \mathcal{L}_{\gamma}\rho\,, \tag{1.98}$$

where the term describing spontaneous decay and dephasing of dipole moment is given by Liouvillean operator

$$\begin{aligned}\mathcal{L}_{\gamma}\rho = &-\gamma_1\left(|3\rangle\langle 3|\rho - 2|1\rangle\langle 1|\rho_{33} + \rho|3\rangle\langle 3|\right)\\ &-\gamma_2\left(|3\rangle\langle 3|\rho - 2|2\rangle\langle 2|\rho_{33} + \rho|3\rangle\langle 3|\right)\,.\end{aligned} \tag{1.99}$$

The first and second terms on right hand side describe spontaneous emission from state $|3\rangle$ to states $|1\rangle$ and $|2\rangle$, with rates $2\gamma_1$ and $2\gamma_2$, respectively. In the third term we have also introduced energy-conserving dephasing processes with rates Γ.

Pluging the effective Hamiltonian from Eq. (1.97) into Eq. (1.98), we obtain the equations of motion for the elements of the density matrix,

$$\dot{\rho}_{33} = -2(\gamma_1+\gamma_2)\rho_{33} + ig\rho_{13} - ig^*\rho_{31} + iG\rho_{23} - iG^*\rho_{32}\,, \tag{1.100}$$

$$\dot{\rho}_{22} = 2\gamma_2\rho_{33} + iG^*\rho_{32} - iG\rho_{23}\,, \tag{1.101}$$

$$\dot{\rho}_{32} = -\left[\Gamma_{32} + i\Delta_c\right]\rho_{32} + ig\rho_{12} + iG\rho_{22} - iG\rho_{33}\,, \tag{1.102}$$

$$\dot{\rho}_{31} = -\left[\Gamma_{31} + i\Delta_p\right]\rho_{31} + iG\rho_{21} + ig\rho_{11} - ig\rho_{33}\,, \tag{1.103}$$

$$\dot{\rho}_{21} = -\left[\Gamma_{21} - i(\Delta_c - \Delta_p)\right]\rho_{21} + iG^*\rho_{31} - ig\rho_{23}\,, \tag{1.104}$$

where the coherence decay rates are defined as $\Gamma_{32} = (\gamma_1 + \gamma_2)$, $\Gamma_{31} = (\gamma_1 + \gamma_2)$, and $\Gamma_{21} = \Gamma$. The remaining equations for population and coherences can be calculated from population conservation condition: $\rho_{11} + \rho_{22} + \rho_{33} = 1$ and $\rho_{ij} = \rho^*_{ji}$. For simplicity, we shall consider the spontaneous emission from the excited state to the ground states with same decay rate $\gamma_1 = \gamma_2 = \gamma$ in our further calculations. We next try to find out exact solutions of these density matrix equations under steady state limit.

1.3.2 Steady state solution of density matrix elements

We exactly solve the density matrix equations under steady state condition. In the steady state condition, the time derivatives of right hand side of density matrix Eqs. (1.100)- (1.100) are set to be zero ($\dot{\rho} = 0$). Now solving these resulting linear algebraic equations one can readily find the populations and the coherences to all order in both probe and control fields. The optical coherence ρ_{31} for probe field is given by

$$\rho_{31} = N/D\,, \tag{1.105}$$

where numerator N and denominator D are given by

$$\begin{aligned} N =&(|G|^2(\gamma(i\gamma + \Delta_p)(\Gamma^2 + (\Delta_c - \Delta_p)^2) \\ &+ (\gamma(i\Gamma + \Delta_c - \Delta_p) + \Gamma(\Delta_c + \Delta_p))|g|^2 + \gamma(i\Gamma + \Delta_c - \Delta_p)|G|^2)g)\,, \end{aligned} \tag{1.106}$$

$$\begin{aligned} D =&(\gamma|g|^6 + |g|^4(2\gamma(\gamma\Gamma + \Delta_c(-\Delta_c + \Delta_p)) + 3(\gamma + 2\Gamma)|G|^2) \\ &+ \gamma|G|^2((\Gamma^2(\Delta_c - \Delta_p)^2)(\gamma^2 + {\Delta_p}^2) \\ &+ 2(\gamma\Gamma + (\Delta_c - \Delta_p)\Delta_p)|G|^2 + |G|^4)|g|^2(\gamma(\gamma^2 + {\Delta_c}^2)(\Gamma^2 + (\Delta_c - \Delta_p)^2) \\ &+ (4\gamma^2\Gamma + \gamma(6\Gamma^2 + 4(\Delta_c - \Delta_p)^2) + \Gamma(\Delta_c + \Delta_p)^2)|G|^2 + 3(\gamma + 2\Gamma)|G|^4))\,. \end{aligned} \tag{1.107}$$

This is exact expression for probe field coherence including both linear as well as nonlinear contributions. We use above coherence to calculate the susceptibility of the medium.

1.3.3 Linear and nonlinear susceptibility of the probe field

The induced polarization for an ensemble of atoms with number density $\mathcal{N}$ and the dipole matrix interaction term $d_{1\alpha}$ between the level $|1\rangle$ and $|j\rangle$ is defined by

$$\mathbf{P}(\mathbf{r}, t) = \mathcal{N}\langle\hat{\mathbf{d}}(\mathbf{r})\rangle = \mathcal{N}Tr(\rho\hat{\mathbf{d}})\,, \tag{1.108}$$

$$\mathbf{P}(\mathbf{r}, t) = \mathcal{N}(\rho_{31}\, e^{-i\omega_p t}\hat{\mathbf{d}}_{13} + \rho_{32}\, e^{-i\omega_c t}\hat{\mathbf{d}}_{23} + \text{c.c.})\,. \tag{1.109}$$

The polarization **P** is also related to the amplitude of the probe field $\mathbf{E}_p$ in the following way

$$\mathbf{P}(\mathbf{r},t) = \chi(\omega_p)\mathbf{E}_p(\mathbf{r},t) = \hat{\mathbf{e}}_p\chi(\omega_p)\mathcal{E}_p(\mathbf{r})\, e^{-\omega_p t} + \text{c.c.}\,. \tag{1.110}$$

Therefore, using Eq. (1.108) and Eq. (1.110), the susceptibility for probe field can be expressed as

$$\chi(\omega_p) = \frac{\mathcal{N}|d_{13}|^2}{\hbar g}\rho_{31} = \frac{3\mathcal{N}\lambda_p^3\gamma}{16\pi^3 g}\rho_{31}\,, \tag{1.111}$$

where $\lambda_p = 2\pi c/\omega_p$ is the wavelength of the $|1\rangle \leftrightarrow \langle 3|$ transition. The spontaneous emission rate γ is given by Weisskopf-Wigner theory: $\gamma = 4|\vec{d}_{13}|^2\omega_p^3/3\hbar c^3$. Note that the expression in Eq (1.111) gives the total susceptibility, including both linear and nonlinear contributions as coherence ρ_{31} is obtained to all orders in probe field.

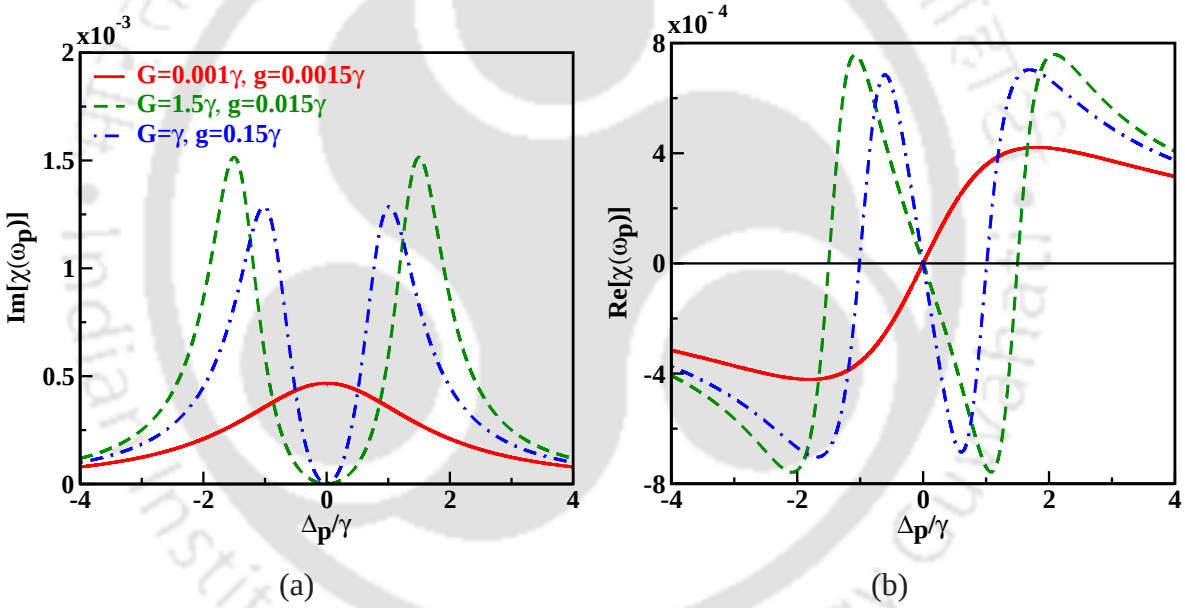

FIGURE 1.6: Imaginary (Im[χ]) and real (Re[χ]) components of probe field susceptibility of Eq. (1.111) as a function of normalized detuning Δ_p/γ. (a) absorption and (b) dispersion. The three different curves are displayed for three sets of fields: $G = 0.001\gamma$, $g = 0.0015\gamma$ (red solid line); $G = 1.5\gamma$, $g = 0.015\gamma$ (green dashed line), and $G = \gamma$, $g = 0.15\gamma$ (blue dot-dashed line). The other parameters are $\Delta_c = 0$, $\Gamma = 0.001\gamma$, $\gamma = 3\pi \times 10^6$ rad/sec, $\lambda = 795$ nm, and $N = 5{\times}10^{11}$ atoms/cm^3.

Fig. 1.6 shows the plot of the probe field susceptibility of Eq. (1.111) as a function of the probe field detuning from resonance. The imaginary component Im[χ] of the susceptibility

which determines the absorption spectrum is illustrated in Fig. 1.6(a). The real component Re[χ] of susceptibility which characterizes the dispersion is displayed in Fig. 1.6(b). As can be seen from Fig. 1.6, the response is highly dependent on the strengths of the probe and control fields. In the limit of a week control field ($G << \gamma$), the Λ-type system reduces to a two-level system driven by a probe field, where a huge absorption is always accompanied with anomalous dispersion around the line center. Surprisingly, for a strong control field ($G >> \gamma, g$), the imaginary part Im[χ] undergoes destructive interference in the region of resonance. This simply means that the coherently driven medium becomes transparent to the weak probe field under the action of a strong control field. This phenomenon is known as *electromagnetically induced transparency* (EIT) [104]. Moreover, the absorption spectrum also carries the signatures of an Autler-Townes doublet [105]. There are two enhanced absorption peaks on the lower and upper frequency sides of absorption profile. Furthermore, the dispersion becomes normal from the anomalous in a region of low absorption. Also, the slope of the normal dispersion curve is more steeper in the vicinity of the line center. The steepness of dispersion can be controlled further by lowering the strength control field and increasing the strength probe field. For example at $G = \gamma \approx g$, we obtain a transparency window with a line width much narrower than the case of strong control field. Therefore, changing the strengths of the fields not only changes the spectral profile of absorption, but also modifies the slope of dispersion. This steep variation in the refractive index profile is useful to control the speed of light inside the medium.

It is now well known that the absorptive and dispersive properties of the atomic medium can be controlled by using external coherent fields. Coherent control of the optical properties of medium by an extra resonant laser field was first proposed by Tewari and Agarwal [106]. EIT was first designated by Harris *et al.* where they discussed the enhancement of nonlinear effects in optical media [107]. The phenomenon of EIT was later experimentally observed in several medium by various research groups. Boller *et al.* were the first to experimentally demonstrate the EIT using an auto-ionizing transition in strontium vapor [108]. In their experiment, the signal beam transmission was improved from e^{-20} to e^{-1} in the presence of a strong coupling field. Field *et al.* [109] reported EIT in Pb vapor where they observed the transmission improvement from e^{-14} to e^{-4}. Xiao *et al.* [110] observed and measured the dispersive properties of EIT in rubidium vapor. The important applications of EIT technique are covered in slow light [111, 112], fast light [113, 114] and stored light [115, 116]. These mechanism of

controlling light have potential applications in quantum networks and quantum information processing.

Using the definition of Eq. (1.66) for series expansion for induced polarization ($P = N\rho_{31}\hat{d}_{13}$), the linear part of polarization can be calculated as

$$P^{(1)} \approx \left(\frac{\partial P}{\partial g}\right)\Big|_{g=0} g = \mathcal{N}\hat{d}_{13}\left(\frac{\partial \rho_{31}}{\partial g}\right)\Big|_{g=0} g \tag{1.112}$$

$$= \mathcal{N}\hat{d}_{13}\frac{ig[\Gamma + i(\Delta_p - \Delta_c)]}{(2\gamma + i\Delta_p)[\Gamma + i(\Delta_p - \Delta_c)] + |G|^2}\,. \tag{1.113}$$

Hence, the explicit expression for linear susceptibility is written as

$$\chi^{(1)}(\omega_p) = \frac{\mathcal{N}|d_{13}|^2}{\hbar}\frac{i[\Gamma + i(\Delta_p - \Delta_c)]}{(2\gamma + i\Delta_p)[\Gamma + i(\Delta_p - \Delta_c)] + |G|^2}\,. \tag{1.114}$$

We now analyze linear susceptibility of the probe field as given in Eq. (1.114). At two-photon resonance $\Delta_p = \Delta_c$, the linear susceptibility reduces to

$$\chi^{(1)}(\omega_p) = \frac{\mathcal{N}|d_{13}|^2}{\hbar}\frac{i\Gamma}{\Gamma(2\gamma + i\Delta_p) + |G|^2}\,. \tag{1.115}$$

It is clear that both the real and imaginary parts of $\chi^{(1)}(\omega_p)$ are zero for $\Gamma = 0$. This true if the levels $|1\rangle$ and $|2\rangle$ have infinitely longer life time. In a Λ-system, the life time of ground levels are much large which gives a large coherence time of the ground state coherence. This is why the Λ-system is very useful to realize the EIT phenomenon as compared to other atomic model configurations.

Following the standard textbooks such as "*Quantum Optics*" by G. S. Agarwal [117], we explain the physical reason behind EIT resonance. We calculate the poles of the denominator of $\chi^{(1)}(\omega_p)$ in Eq. (1.114). At pump field resonance $\Delta_c = 0$, the two poles are given by

$$\Delta_p = \frac{i}{2}(2\gamma + \Gamma) \pm \sqrt{|G|^2 - \frac{1}{4}(2\gamma - \Gamma)^2}\,. \tag{1.116}$$

The first term gives the width which is $(2\gamma + \Gamma)/2$ and the second term gives the position of the two absorption peaks. It should be noted that absorption peaks have some contribution from dephasing rates, not exactly located at $\pm|G|$. We now discuss the pole structure for different conditions of control field strength $|G|$.

1. For the first case in which $|G| << \frac{1}{2}|2\gamma - \Gamma|$, the two poles are

$$\Delta_p = \frac{i}{2}(2\gamma + \Gamma) \pm i\sqrt{\frac{1}{4}(2\gamma - \Gamma)^2 - |G|^2}$$
$$\approx 2i\gamma, i\Gamma + |G|^2/(2\gamma - \Gamma) \qquad \gamma >> \Gamma\,. \tag{1.117}$$

Hence, in this case two poles are purely imaginary and as usually $\gamma >> \Gamma$, there exists only one absorption peak at $\Delta_p = 0$ with line width 2γ. This condition is depicted by a solid red line in Fig. 1.6(a).

2. For the second case in which $|G| >> \frac{1}{2}|2\gamma - \Gamma|$, the two poles are

$$\Delta_p \approx \frac{i}{2}(2\gamma + \Gamma) \pm |G|\,. \tag{1.118}$$

This case represents the Autler-Townes splitting [105] where two absorption profiles have distinct frequencies but same width $(2\gamma + \Gamma)/2$. The green dashed line in Fig. 1.6(a) illustrates this particular condition of strong control field.

3. In the third case of $|G| = \frac{1}{2}|2\gamma - \Gamma|$, the two poles are

$$\Delta_p = \frac{i}{2}(2\gamma + \Gamma) \pm i\sqrt{\frac{1}{4}(2\gamma - \Gamma)^2 - |G|^2}$$
$$\approx i\gamma, \qquad \gamma >> \Gamma\,. \tag{1.119}$$

This condition corresponds to two peaks in the absorption profile (see blue dot-dashed line in Fig. 1.6(a)). In order to understand above properties of EIT resonance, we proceed to dressed state analysis of effective Hamiltonian Eq. (1.97). Dressed state analysis provides a complete physical interpretation of both CPT and EIT resonances.

1.3.4 Dressed state analysis of the three-level Λ-system

Using the bare eigenstates $|1\rangle$, $|2\rangle$, and $|3\rangle$ of free atom as the basis vectors, the matrix representation of the rotating frame Hamiltonian Eq. (1.97) can be defined as

$$H_{eff} = -\hbar \begin{bmatrix} 0 & 0 & g^* \\ 0 & -(\Delta_p - \Delta_c) & G^* \\ g & G & -\Delta_p \end{bmatrix}$$

This effective Hamiltonian in rotating frame can be diagonalized to extract its new eigenvalues and eigenstates. The new eigenstates are a coherent superposition of the bare atomic states and are regarded as dressed states of Λ-system. For the special case of two-photon resonance ($\Delta = 0$), we find the three new eigenstates as

$$|\alpha_0\rangle = \cos\theta\,|1\rangle - \sin\theta\,|2\rangle\,, \tag{1.120}$$

$$|\alpha_+\rangle = \sin\theta\sin\phi\,|1\rangle + \cos\theta\sin\phi\,|2\rangle + \cos\phi\,|3\rangle\,, \tag{1.121}$$

$$|\alpha_-\rangle = \sin\theta\cos\phi\,|1\rangle + \cos\theta\cos\phi\,|2\rangle - \sin\phi\,|3\rangle\,, \tag{1.122}$$

where the angles θ and ϕ are known as mixing angles and are given by

$$\tan\theta = \frac{g}{G}\ \ , \tan(2\phi) = \frac{2\sqrt{(|g|^2 + |G|^2)}}{\Delta_p}. \tag{1.123}$$

The corresponding energy eigenvalues are given by

$$\epsilon_0 = 0\,, \tag{1.124}$$

$$\epsilon_+ = \frac{\hbar}{2}\left[\Delta_p + \sqrt{{\Delta_p}^2 + 4(|g|^2 + |G|^2)}\right], \tag{1.125}$$

$$\epsilon_- = \frac{\hbar}{2}\left[\Delta_p - \sqrt{{\Delta_p}^2 + 4(|g|^2 + |G|^2)}\right]. \tag{1.126}$$

The dressed state $|\alpha_0\rangle$ remains at zero energy while other two dressed states $|\alpha_+\rangle$ and $|\alpha_-\rangle$ are shifted up and down by an amount ϵ_+ and ϵ_-, respectively. The eigenstate $|\alpha_0\rangle$ is a linear superposition of the two ground states $|1\rangle$ and $|2\rangle$ and it does not contain the excited state $|3\rangle$. Thus, the state $|\alpha_0\rangle$ is decoupled from the laser field and there is no possibility of excitation to the state $|3\rangle$. Therefore, the state $|\alpha_0\rangle$ is known as dark state. The atoms prepared in this state will not absorb or emit any light and will be trapped in this dark state. This phenomenon is known as "*coherent population trapping*" (CPT) [23, 24]. This case is illustrated by a blue dot-dashed line in Fig. 1.6(a) where two laser fields have comparable strength $g \approx G$. The first experimental observation on CPT was reported by Alzetta *et al.* [118]. In their work, they found that the absorption vanishes when the fluorescence of sodium atoms is illuminated

by a two coherent laser fields. This fluorescent spectrum was analyzed as a function of external inhomogeneous magnetic field applied along the axis of vapor cell. They observed a regular decrease in fluorescence intensity at some positions along the length of the vapor cell. This happens when the hyperfine splittings of the ground state coincides with the frequency difference of the two laser fields. Orriols [119] has theoretically explained the absorption cancellation by using coherence and interference effects that lead to the CPT phenomenon. The application of CPT mechanism includes lasing without inversion [120], coherent population transfer [121], metrology [122], and in the area of atomic clocks [123–125].

We now consider a special case where the probe field (g) is much weaker than the control field (G), that is, $g << G$. The resulting dressed states at probe resonance ($\Delta_p = 0$) are given by

$$|\alpha_0\rangle = |1\rangle\,, \tag{1.127}$$

$$|\alpha_+\rangle = \frac{1}{\sqrt{2}}(|2\rangle + |3\rangle)\,, \tag{1.128}$$

$$|\alpha_-\rangle = \frac{1}{\sqrt{2}}(|2\rangle - |3\rangle)\,. \tag{1.129}$$

It is evident that a weak probe field does not affect the atomic states and thus the ground state $|1\rangle$ becomes identical to the dark state $|\alpha_0\rangle$. In contrast, a strong control field induces coherent superposition of states $|2\rangle$ and $|3\rangle$. The total transition amplitude from ground state $|1\rangle$ to the dressed states $|\alpha_+\rangle$ and $|\alpha_-\rangle$ is zero. This means that the probe absorption vanishes when the two-photon resonance condition is satisfied. This is so-called EIT phenomenon and it is illustrated by a green dashed-line in Fig. 1.6(a).

In the weak probe field limit, the separation of between the states $|\alpha_+\rangle$ and $|\alpha_-\rangle$ is the twice of control field Rabi frequency, $2|G|$. The two absorption peaks in the EIT spectra occurs at $\Delta_p = \pm|G|$ due to two transitions from $|1\rangle$ to the dressed states $|\alpha_+\rangle$ and $|\alpha_-\rangle$, respectively.

So far we have discussed the effect of the electric field on the atoms and their responses in terms of absorption and dispersion. The complex susceptibility given by Eq. (1.111) represents the response of the system to an applied field. This response then gives the induced polarization which acts as a source for Maxwell's wave equation. We next derive beam propagation equation using basic Maxwell's equations.

1.4 Maxwell's wave equation in a dielectric medium

We now discuss the effect of atomic response on the propagation dynamics of the electric field by using the classical theory of electromagnetism. The classical theory commences with Maxwell's equations in a dielectric medium [126, 127]. We start writing down the fundamental Maxwell's equations in Gaussian units which govern the propagation of an electromagnetic field. In a medium they can be written as following

$$\nabla \cdot \mathbf{D} = 4\pi\varrho\,, \text{(Gauss's Law)} \tag{1.130}$$

$$\nabla \cdot \mathbf{B} = 0\,, \text{(Gauss's Law for Magnetism)} \tag{1.131}$$

$$\nabla \times \mathbf{E} = -\frac{1}{c}\frac{\partial \mathbf{B}}{\partial t}\,, \text{(Faraday's Law of Induction)} \tag{1.132}$$

$$\nabla \times \mathbf{H} = \frac{4\pi}{c}\mathbf{J} + \frac{1}{c}\frac{\partial \mathbf{D}}{\partial t}\,, \text{(Ampere's Circuital Law)} \tag{1.133}$$

where **E** and **H** are time-avaraged values of the basic electric and magnetic field vectors at some space-time point $(\mathbf{r}, t)$, rather than instantaneous values, respectively. The speed of light is denoted by c. The material equations for the electric displacement **D** field and the magnetic induction **B**, coming from the interaction of matter and field, are as follows:

$$\mathbf{D} = \mathbf{E} + 4\pi\mathbf{P}\,, \tag{1.134}$$

$$\mathbf{B} = \mathbf{H} + 4\pi\mathbf{M}\,, \tag{1.135}$$

where **P** is the electric polarization and **M** is the magnetic polarization which are defined in terms of microscopic bound charges and bound current respectively. We assume that the medium is non magnetic $\mathbf{M} = 0$, charge free $\varrho = 0$, and non conducting $\mathbf{J} = 0$. By taking curl of the equation Eq. (1.132) and using Eq. (1.134), one can rewrite it as follows

$$\nabla \times \nabla \times \mathbf{E} + \frac{1}{c^2}\frac{\partial^2}{\partial t^2}(\mathbf{E} + 4\pi\mathbf{P}) = 0\,. \tag{1.136}$$

Now using identity $\nabla \times \nabla \times \mathbf{A} = \nabla(\nabla \cdot \mathbf{A}) - \nabla^2\mathbf{A}$ in Eq. (1.136), we find the wave equation for a transverse electric field ($\nabla \cdot \mathbf{E} = 0$) as the following,

$$\nabla^2\mathbf{E} - \frac{1}{c^2}\frac{\partial^2 \mathbf{E}}{\partial t^2} = \frac{4\pi}{c^2}\frac{\partial^2 \mathbf{P}}{\partial t^2}\,. \tag{1.137}$$

This is Maxwell's wave equation for an electric field in a dielectric medium. The equation determines how the field changes as it propagates through the medium. The term on the right-hand side of Eq. (1.137) containing the macroscopic polarization **P** is related to the microscopic polarization of the medium. The optical properties of the medium such as absorption and refractive index modify the evolution of the electric field. In order to simplify the wave Eq. (1.137), we make some reasonable approximation by writing explicit form of an electric field and the polarization. If a nearly monochromatic electric field is propagating along the z-direction of medium with frequency ω and wave vector k, then we have both electric field and field-induced polarization of the following forms:

$$\mathbf{E}(x,y,z,t) = \hat{\mathbf{e}}\mathcal{E}(x,y,z,t)\, e^{i(kz-\omega t)} + \text{c.c.}\,, \tag{1.138}$$

$$\mathbf{P}(x,y,z,t) = \hat{\mathbf{e}}\mathcal{P}(x,y,z,t)\, e^{i(kz-\omega t)} + \text{c.c.}\,, \tag{1.139}$$

where $\mathcal{E}(x,y,z,t)$ and $\mathcal{P}(x,y,z,t)$ are the slowing varying envelope functions. The unit vector $\hat{\mathbf{e}}$ denotes the direction of polarization.

The required derivatives of Eq. (1.137) are given by

$$\nabla^2\mathbf{E} = \hat{\mathbf{e}}(\nabla_\perp^2\mathcal{E} + \frac{\partial^2\mathcal{E}}{\partial z^2} + 2ik\frac{\partial\mathcal{E}}{\partial z} - k^2\mathcal{E})\, e^{ikz-i\omega t} + \text{c.c.}\,, \tag{1.140}$$

$$\frac{\partial^2\mathbf{E}}{\partial t^2} = \hat{\mathbf{e}}(\frac{\partial^2\mathcal{E}}{\partial t^2} - 2i\omega\frac{\partial\mathcal{E}}{\partial t} - \omega^2\mathcal{E})\, e^{ikz-i\omega t} + \text{c.c.}\,, \tag{1.141}$$

$$\frac{\partial^2\mathbf{P}}{\partial t^2} = \hat{\mathbf{e}}(\frac{\partial^2\mathcal{P}}{\partial t^2} - 2i\omega\frac{\partial\mathcal{P}}{\partial t} - \omega^2\mathcal{P})\, e^{ikz-i\omega t} + \text{c.c.}\,, \tag{1.142}$$

where $\nabla_\perp^2 = \partial^2/\partial x^2 + \partial^2/\partial y^2$ is the transverse Laplacian operator in the transverse direction. We assume that the change in envelopes of the electric field $\mathcal{E}$ and polarization $\mathcal{P}$ with time and space are very small within the optical period and optical wavelength. Mathematically, this assumption can be represented by following inequalities:

$$\left|\frac{\partial^2\mathcal{E}}{\partial z^2}\right| \ll \left|k\frac{\partial\mathcal{E}}{\partial z}\right| \ll |k^2\mathcal{E}|, \quad \left|\frac{\partial^2\mathcal{E}}{\partial t^2}\right| \ll \left|\omega\frac{\partial\mathcal{E}}{\partial t}\right| \ll |\omega^2\mathcal{E}|\,, \tag{1.143}$$

$$\left|\frac{\partial^2\mathcal{P}}{\partial z^2}\right| \ll \left|k\frac{\partial\mathcal{P}}{\partial z}\right| \ll |k^2\mathcal{P}|, \quad \left|\frac{\partial^2\mathcal{P}}{\partial t^2}\right| \ll \left|\omega\frac{\partial\mathcal{P}}{\partial t}\right| \ll |\omega^2\mathcal{P}|\,. \tag{1.144}$$

The above approximation is known as the "*slowly varying envelope approximation*" (SVEA). Substituting above derivatives into Eq. (1.137) and ignoring the second order partial derivatives with respect to z and t, we find wave equation for slowly varying electric field envelope as follows:

$$\frac{1}{2ik}\nabla_{\perp}^{2}\mathcal{E} + \frac{\partial \mathcal{E}}{\partial z} + \frac{1}{c}\frac{\partial \mathcal{E}}{\partial t} = 2\pi ik\mathcal{P}. \tag{1.145}$$

We consider that the laser beam is a continuous wave and thus $\frac{\partial \mathcal{E}}{\partial t} = 0$. Therefore, the above equation becomes

$$\frac{1}{2ik}\nabla_{\perp}^{2}\mathcal{E} + \frac{\partial \mathcal{E}}{\partial z} = 2\pi ik\mathcal{P}. \tag{1.146}$$

The above form of wave equation is called "*paraxial wave equation*". This paraxial wave equation for electric field amplitude $\mathcal{E}$ can be expressed in terms of probe field Rabi frequency $g = d_{31}\mathcal{E}_{\rm p}/\hbar$ and polarization $P = \chi_p \mathcal{E}_p$. We obtain propagation equation for probe field as

$$\frac{\partial g}{\partial z} = \frac{ic}{2\omega}\left(\frac{\partial^2 g}{\partial x^2} + \frac{\partial^2 g}{\partial y^2}\right) + 2i\pi k\chi_p g\,. \tag{1.147}$$

Here $\omega = ck$ and c is velocity of light in free space. The first terms in parentheses on the right hand side describes the beam diffraction. The second term accounts for the dispersion and absorption of the beam inside the medium. This equation can be solved numerically using split-step Fourier method given in Appendix A.

1.4.1 The origin of paraxial diffraction and diffraction-limit

The classical resolution limit imposed by optical diffraction originates from its geometrical effects [126, 127]. The physical interpretation of paraxial diffraction spreading of any arbitrary image of the light beam with finite shape and size can be given by its Fourier decomposition. The distribution of any electric field associated with the laser beam can be represented as a superposition of plane waves:

$$\mathbf{E}(\mathbf{r}, t) = \sum_{k_x, k_y} \mathbf{E}(k_x, k_y)\, e^{i(k_z z + k_x x + k_y y - \omega t)} + \text{c.c.}\,. \tag{1.148}$$

We consider the light propagation in z-direction. Using Maxwell's equation one can readily find the longitudinal component of the wave vector

$$k_z = \sqrt{k^2 - {k_x}^2 - {k_y}^2}\,, \tag{1.149}$$

where $k = n\omega/c$ is an absolute value of wave vector $\mathbf{k} = (k_x, k_y, k_z)$. Here n is the refractive index of medium at wavelength λ.

For larger values of spatial frequency components k_x, k_y, i.e., when $n^2\omega^2/c^2 < {k_x}^2 + {k_y}^2$, then k_z component becomes complex

$$k_z = i\sqrt{{k_x}^2 + {k_y}^2 - k^2}\,. \tag{1.150}$$

These are so-called evanescent waves which decay exponentially with distance z. Detection of evanescent waves to improve spatial resolution comes under near-field microscopy. These waves cannot be collected in conventional materials as they decay exponentially with propagation distance.

However, we are interested in propagating waves for which $(n^2\omega^2/c^2 > {k_x}^2 + {k_y}^2)$. In the paraxial limit $k_x, k_y << k$, the Eq. (1.149) can be written as

$$k_z = k - \frac{{k_x}^2 + {k_y}^2}{2}\,. \tag{1.151}$$

The phase gathered by each transverse components k_x or k_y of a plane wave after a propagation distance z is given by

$$\phi(k_x, k_y, z) = k_z(k_x, k_y)z\,. \tag{1.152}$$

Therefore, each Fourier component acquires a unique phase shift throughout its propagation either in free space or medium. The coherent superposition of all plane wave components at one point of space gives rise to diffraction. As a result, the transmitted beam or an image is distorted heavily even after propagating only a few Rayleigh lengths. This interpretation indicates that diffraction can be eliminated if conditions are engineered such that each plane wave component acquires the same phase shift during propagation. For example, several specially-shaped beams with spatially-dependent phases such as Airy [128, 129], Bessel [130, 131], and Mathieu beams [132, 133] has been suggested which can propagate without diffraction in

free space. In these special class of non-diffracting beams, the phase gathered by each plane wave comprising beams are exactly equal. Consequently, the superposition of all plane waves remains the same during the propagation.

From this interpretation it is clear that the propagating waves are limited to $n^2\omega^2/c^2 > {k_x}^2 + {k_y}^2$. Therefore, the information about the smallest spatial feature size of an image is contained in the largest spatial frequencies k_x and k_y. The largest value of ${k_x}^2 + {k_y}^2$ is given by ${k_x}^2 + {k_y}^2 = k^2$. Therefore, the maximum resolution of spatial shape in the image is limited to

$$\Delta x = \frac{2\pi}{k} = \frac{2\pi c}{n\omega} = \frac{\lambda}{n}\,. \tag{1.153}$$

This is called the classical diffraction-limit of an optical device. Overcoming this limit and reducing feature size of an image is one of the main goals in the high resolution spectroscopy. From this equation, it is very clear that there is a possibility of reducing the feature size of an image by increasing the refractive index of the medium. This reduced feature size find potential applications in optical lithography and in optical imaging.

1.4.2 Paraxial wave equation in free-space

The wave equation for the electric field in free-space can be obtained from Eq. (1.137) by ignoring the source term ($\mathbf{P} = 0$) as

$$\nabla^2\mathbf{E} - \frac{1}{c^2}\frac{\partial^2\mathbf{E}}{\partial t^2} = 0\,. \tag{1.154}$$

Let us consider a solution of Eq. (1.154) for a linearly polarized monochromatic electric field of the following form

$$\mathbf{E}(\mathbf{r}, t) = \hat{\mathbf{e}}\mathcal{E}(\mathbf{r})\, e^{-i\omega t} + \text{c.c.}\,, \tag{1.155}$$

where $\mathbf{r}$ is the position vector which defines a point in three-dimensional space, ω is the monochromatic angular frequency and $\mathcal{E}(\mathbf{r})$ is one of the electromagnetic field components. Substituting this expression in Eq. (1.154), we obtain

$$\nabla^2\mathcal{E}(\mathbf{r}) + k^2\mathcal{E}(\mathbf{r}) = 0\,, \tag{1.156}$$

where $k = \omega/c$ is the wave number. This equation is known as a Helmholtz equation which describes the propagation of monochromatic waves in free-space. One of the solutions to the spatial Helmholtz equation Eq. (1.156) is written as

$$\mathcal{E}(\mathbf{r}) = \mathcal{E}_0\, e^{i\mathbf{k}\cdot\mathbf{r}}\,, \tag{1.157}$$

where $\mathcal{E}_0$ is the constant amplitude and $\mathbf{k}$ is the wave vector with magnitude k. This is so called plane wave solution of the scalar Helmholtz equation. Such a plane wave solution has the same value for all points in any plane normal to wave vector. If we choose the z-axis as the direction of wave propagation, then the plane wave is given by

$$\mathcal{E}(\mathbf{r}) = \mathcal{E}_0\, e^{ikz}\,. \tag{1.158}$$

Ideally, a plane wave does not diffract because it has an infinite cross-sectional area. The output of a laser source is sufficiently collimated along the z-axis and propagates with some finite cross-sectional area. Therefore, we now search beam-like solutions of scalar Helmholtz equation for a unidirectional laser beam. We consider a solution for the laser beam as follows:

$$\mathcal{E}(\mathbf{r}) = \mathcal{E}_0(\mathbf{r})\, e^{ikz}\,, \tag{1.159}$$

where the field amplitude $\mathcal{E}_0(\mathbf{r})$ is no longer constant, unlike a plane wave. Substituting this form of field into Helmholtz equation, we get

$$\left(\frac{\partial^2\mathcal{E}_0}{\partial x^2} + \frac{\partial^2\mathcal{E}_0}{\partial y^2} + \frac{\partial^2\mathcal{E}_0}{\partial z^2} + 2ik\frac{\partial\mathcal{E}_0}{\partial z} - k^2\mathcal{E}_0\right) e^{ikz} + k^2\mathcal{E}_0(\mathbf{r})\, e^{ikz} = 0\,. \tag{1.160}$$

We assume that the variations of field envelope $\mathcal{E}_0(\mathbf{r})$ in the z direction are very small as compared to transverse directions (x, y) within a distance of the order of a wavelength. This assumption can be expressed mathematically as

$$\left|\frac{\partial^2\mathcal{E}}{\partial z^2}\right| \ll \left|\frac{\partial^2\mathcal{E}}{\partial x^2}\right|,\ \left|\frac{\partial^2\mathcal{E}}{\partial y^2}\right|,\ \left|k\frac{\partial\mathcal{E}}{\partial z}\right|,\ |k^2\mathcal{E}|\,. \tag{1.161}$$

This is called "*paraxial wave approximation*". Under the paraxial wave approximation, we ignore $\frac{\partial^2 \mathcal{E}}{\partial z^2}$ and rewrite the Helmholtz equation as

$$\left(\frac{\partial^2 \mathcal{E}_0}{\partial x^2} + \frac{\partial^2 \mathcal{E}_0}{\partial y^2} + 2ik\frac{\partial \mathcal{E}_0}{\partial z}\right) = 0\,. \tag{1.162}$$

This equation is known as "*paraxial wave equation*". The solutions of this partial differential equation yields an infinite set of functions. For examples, Gaussian, Hermite-Gaussian, and Laguerre-Gaussian beams are some well-known standard solutions to the paraxial wave equation in free-space [134]. In the following, we discuss these standard modes in great detail.

1.4.3 The Gaussian beam

The Gaussian beam is the lowest-order solution the paraxial Helmholtz equation. This is the fundamental transverse mode of most of the laser's optical resonator. A mathematical expression for its complex electric field amplitude can be written as

$$\mathcal{E}(\mathbf{r}) = \mathcal{E}_0 \frac{w_0}{w(z)} \exp\left[-\frac{(x^2+y^2)}{w(z)^2} + \frac{ik(x^2+y^2)}{2R(z)} - i\phi - ikz\right], \tag{1.163}$$

$$w(z) = w_0\sqrt{1+\left(\frac{z}{z_R}\right)^2}, \tag{1.164}$$

$$R(z) = z\left[1+\left(\frac{z_R}{z}\right)^2\right], \tag{1.165}$$

$$\phi = \tan^{-1}\left[\frac{z}{z_R}\right], \tag{1.166}$$

$$z_R = \frac{\pi w_0^2}{\lambda}, \tag{1.167}$$

Here $w(z)$ is the beam width at which the field amplitude falls to e^{-1} or intensity drops to e^{-2} of its axial value. It has a minimum value w_0 at $z = 0$ which is refereed as the beam waist or the spot size. The quantity $R(z)$ is the radius of curvature of the beam's wavefronts comprising the beam. The phase factor ϕ is an additional contribution to the phase of the Gaussian beam. This extra phase is known as the longitudinal Gouy phase. The parameter z_R is known as the Rayleigh range which is a measure of the distance on z-axis from the waist to the point at which the width $w(z)$ becomes $\sqrt{2}w_0$. The Rayleigh range z_R will be smaller for the smaller value of the spot size w_0 and thus the greater is the rate of growth with z of the beam width

from the waist. The beam size $w(z)$ increases with distance and becomes linear with z for $z >> z_R$. Hence, the beam divergence is strong in the far-field region. The far-field divergence angle of the Gaussian beam is given by

$$\begin{aligned}\Theta = 2\theta &= 2\frac{w(z)}{z} \\ &\approx 2\frac{w_0}{z_R} = 2\frac{\lambda}{\pi w_0} \qquad (z >> z_R)\,. \end{aligned} \tag{1.168}$$

Clearly, the divergence angle Θ is inversely proportional to the minimum spot size w_0. Thus a Gaussian beam that is focused into a smaller spot spreads out rapidly as it moves away from that waist. In order to avoid the laser beam divergence and to make it well collimated, it must have a larger diameter. A plane wave diffraction through a circular aperture having diameter D has a divergence angle similar to laser beam divergence angle. In this case, the far-field divergence angle is given by

$$\Theta = 1.22\frac{\lambda}{D}\,. \tag{1.169}$$

It is evident from this equation that smaller the aperture diameter D, greater the diffraction. Thus we conclude that a Gaussian beam model is diffraction-limited because it uses the paraxial approximation. This model fails when wavefront are tilted by more than about 10° from the direction of propagation [54]. Expression (1.168) implies that the Gaussian beam formalism is valid only for beams with waists much larger than the wavelength of light. In other words, the paraxial approximation in Eq. (1.161) will not be valid for a Gaussian beam with waists smaller than the wavelength or comparable to wavelength. Therefore, in order to study the beam propagation beyond the paraxial approximation one must retain the second order derivative in z-direction [54, 135].

1.4.4 The Super-Gaussian beam

A Super-Gaussian beam is a light beam which has a uniform intensity across the beam profile. Flat-top beam or top-hat beam can be also approximated as Super-Gaussian beam with some smooth edges. These beams are just opposite to Gaussian beams where the intensity smoothly

drops from its maximum to zero around the beam axis. The transverse profile of a Super-Gaussian beam can be given by

$$\mathcal{E}(\mathbf{r}) = \mathcal{E}_0 \exp\left[-\left(\frac{x^2+y^2}{w^2}\right)^p\right]. \tag{1.170}$$

where $\mathcal{E}_0$ is peak amplitude and w is the beam width of the Super-Gaussian beam; p is an order parameter that determines the different spatial beam shapes. The order parameter $p = 1$ gives a usual Gaussian beam profile. A super-Gaussian mode can be obtained by choosing order parameter $p = 10$. A nearly flat-top beam is obtained by setting $p = 100$. Thus, at very large values of the order parameter the Super-Gaussian beams approach to flat-top beams. Super-Gaussian or Flat-top beams can be generated by using a graded-phase mirror resonator[136] or a spatial light modulator based on liquid crystal [137]. Need to mention here, a Super-Gaussian or a flat-top beam is not a free-space mode as the order parameter p has been added intentionally. A super-Gaussian beam is not a part of standard solutions to the paraxial wave equation. The propagation of an initially super-Gaussian beam in free-space or through optical elements shows that the beam profile first contracts to form smooth edges and spreads further. A circular or rectangular super-Gaussian beam evolves Gaussian-like structure in the center but an airy or sinc function in far-field region. Unlike Gaussian beam, a super-Gaussian beam would not only change the size but also the intensity profile.

1.4.5 Hermite-Gaussian beam

Hermite-Gaussian modes are solutions for the lasers whose cavity design has a rectangular geometry rather than radially symmetric. Therefore, solving the paraxial Helmholtz equation (1.162) in Cartesian coordinates gives rise to a family of solutions known as the Hermite-Gaussian modes [138]. The transverse spatial profile of the electric field for Hermite-Gaussian mode is given by

$$\begin{aligned}\mathcal{E}_{mn}(\mathbf{r}) = \mathcal{E}_0 \frac{w_0}{w(z)} H_m\left(\frac{x\sqrt{2}}{w(z)}\right) \exp\left[-\frac{x^2}{w(z)^2}\right] H_n\left(\frac{y\sqrt{2}}{w(z)}\right) \exp\left[-\frac{y^2}{w(z)^2}\right] \\ \times \exp\left[-i(m+n+1)\tan^{-1}\left(\frac{z}{z_R}\right)\right].\end{aligned} \tag{1.171}$$

Here, $\mathcal{E}_0$ is the constant amplitude, and $w(z)$ is the width of the electric field. The function H_k is a Hermite polynomial of order k, and the indices m and n determine the shape of the electric field profile along the x and y directions, respectively. The lowest-order Hermite-Gaussian beam $m = n = 0$ is fundamental the Gaussian beam. The spatial light modulator based on liquid crystal can be used to produce the Hermite-Gaussian Beams [139].

1.4.6 Laguerre-Gaussian beam

If the laser's optical resonator is cylindrically symmetric, the natural solutions of the paraxial wave equation result in Laguerre-Gaussian modes [140]. Thus, the solution of the paraxial Helmholtz equation in cylindrical coordinates (ρ, ϕ, z) leads to the LaguerreGaussian modes. The complex amplitude of the Laguerre-Gaussian beam is expressed as

$$\mathcal{E}_{pl}(\rho,\phi,z) = \mathcal{E}_0 \frac{w_0}{w(z)} \left(\frac{\rho\sqrt{2}}{w(z)}\right)^{|l|} L_p^{|l|}\left(\frac{2\rho^2}{w^2(z)}\right)^{|l|} \exp\left[\frac{ik\rho^2}{2R(z)} - \frac{\rho^2}{w^2(z)}\right] \times \exp\left[-i(2p+l+1)\tan^{-1}\left(\frac{z}{z_R}\right) + il\phi\right], \tag{1.172}$$

where $L_p^{|l|}$ is the generalized Laguerre polynomial function, p is the radial index and l is the azimuthal index. The lowest-order Laguerre-Gaussian beam $l = p = 0$ coincides with the Gaussian beam. The other beam parameters are same as a Gaussian beam case. The Laguerre-Gaussian beam can be produced using a computer generated holograms [141, 142], or all-optical spatial light modulator in coherent media [143] and digital micro-mirror device [144].

Chapter 2

Diffractionless optical cloning via single dark states

In this chapter, we theoretically explore the possibility of cloning of an arbitrary image carried on control field to probe field with high resolution. For this purpose, we utilize the EIT and CPT resonances in presence of spatially dependent coherent fields to obtain higher spatial resolution. A rigorous literature survey suggested the possibility of an alternative way of imaging through various theoretical and experimental approaches based on EIT and CPT schemes. Mitsunaga *et al.* have suggested and experimentally demonstrated an EIT based absorption imaging technique in cold sodium atoms [145]. They found that a bright spot of signal beam is transmitted through an opaque atomic cloud at the points where coupling beam was present. In their experimental set up, they achieved signal beam transmission upto 200% which is due to cross-focusing effect induced by spatial dependent coupling beam. Based on CPT mechanism, Agarwal *et al.* have predicted that the atom can be localized at subwavelength scale [146]. They have used standing-wave and tightly focused beams to spatially localize the atomic population in subwavelength domain. In an extension of this CPT based scheme, Yavuz and colleagues have discussed and reported the atom localization by spatial dependent dark state [147]. They predict that a fluorescence shadow image of a nanometer sized object implanted into an atomic medium can be obtained by scanning the focusing lens around the object. In an early work, Kapale and Agarwal [148] have found a new optical microscopy technique by using CPT mechanism. In this scheme, three-level atom is driven by an amplitude modulated probe field and a spatially dependent coupling field to localize the

population. Additionally, they have predicted that localization scheme can be used to get a shadow image of nanometer sized object embedded into the atomic medium.

More recently, Li *et al.* [153] experimentally demonstrated that the spatial shape of a control beam can be cast onto a weak probe beam via CPT in a three-level lambda atomic system. In their experiment, the transmitted intensity of the probe beam had a similar spatial profile as that of the control beam, no matter what the input probe is. Moreover, the size of the transmitted probe beam was half of that of the diffraction-limited input probe.

These studies motivate us to explore other possibility of mapping the spatial shape of control beam onto probe beam. The spatial profile of the strong control beam makes the probe's susceptibility inhomogeneous along the transverse direction. This inhomogeneity in susceptibility leads to spatial variations in both absorption and refractive index of probe beam. Key idea behind cloning mechanism is that the absorption and refractive index profiles are dependent on shape and intensity of control beam. Thus, the absorption and refractive index profiles can be flexibly engineered along the transverse direction with desired shape of control beam.

In our study, both control and probe fields are coupled to a three-level atomic lambda system to form a CPT configuration. It is important to note that the probe field is typically treated as a weak and control field as a strong, such that perturbation theory can be employed to derive the linear effect of the atomic medium on the probe field propagation. There have been theoretical and experimental studies where the probe is not necessarily weak [149–151]. In this situation, the effect of the atomic coherence on the propagation dynamics of the control field need to be taken into account [152]. We assume the two laser fields to be of comparable strength, such that perturbation theory for the probe field is not valid any more to describe the effect of the atomic medium on the two fields. We start by calculating the susceptibilities including linear and nonlinear effects for both fields by solving the related density matrix equations. As expected, we find that a spatially-dependent refractive index for the probe field is generated, structured by the spatial intensity profile of the control beam. In particular, the generated structures enable one to transfer the transverse distribution of the control field onto the transmission profile of the probe field. In order to study the full propagation dynamics, we then numerically solve the paraxial propagation equations for both fields by using a higher order split operator method. We begin our analysis with a Gaussian control and a super-Gaussian probe field and observe the gradual mapping of the control field onto the probe field

throughout the propagation. We find in particular that in the case of a strong probe field, the transmitted probe beam is focused more tightly by a factor of two compared to the weak probe field case. Next, we consider a control field with a spatial two-peaked Hermite-Gaussian profile, and demonstrated cloning of the profile onto the probe beam with feature size reduced by a factor of about 2.5. In order to verify that our method can serve as an universal tool for cloning of arbitrary image, we finally simulate the three-dimensional light propagations for both fields, in which the spatial profile of the control field carries the three letters "CPT". We show that also this structure can be cloned onto the probe beam which initially has a simple plane-wave profile, even though the control field is severely distorted throughout the propagation due to diffraction. Again, we observe a reduction of the feature size by a factor of about 2 in the probe field.

2.1 Theoretical model and basic dynamical equations

2.1.1 Equations of motion for density matrix elements

We consider a homogeneous cloud of ^{87}Rb atoms, with two laser fields coupled to the atoms such that a three-level Λ-scheme as shown in Fig. 2.1 is of relevance. The probe field couples to transition $|1\rangle \leftrightarrow |3\rangle$, and the control field to transition $|2\rangle \leftrightarrow |3\rangle$. The two copropagating fields are defined as

$$\mathbf{E}_j(\mathbf{r},t) = \hat{\mathbf{e}}_j \mathcal{E}_j(\mathbf{r})\, e^{-i\left(\omega_j t - k_j z\right)} + \text{c.c.}\,, \tag{2.1}$$

where $\mathcal{E}_j(\mathbf{r})$ are the slowing varying envelope functions, $\hat{\mathbf{e}}_j$ the unit polarization vectors, ω_i the laser field frequencies and k_j is the wave numbers of fields. The index $j \in \{1,2\}$ denotes the probe or control field, respectively.

The Hamiltonian of the system in electric dipole and rotating wave approximation is given by,

$$\begin{aligned}\hat{H} &= \hbar\omega_{a3}|3\rangle\langle 3| + \hbar\omega_{a2}|2\rangle\langle 2| + \hbar\omega_{a1}|1\rangle\langle 1| \\ &\quad - \hbar\left(g e^{-i\omega_1 t}|3\rangle\langle 1| + G e^{-i\omega_2 t}\,|3\rangle\langle 2| \;+\; \text{H.c.}\right),\end{aligned} \tag{2.2}$$

where ω_{aj} are the corresponding atomic frequencies.

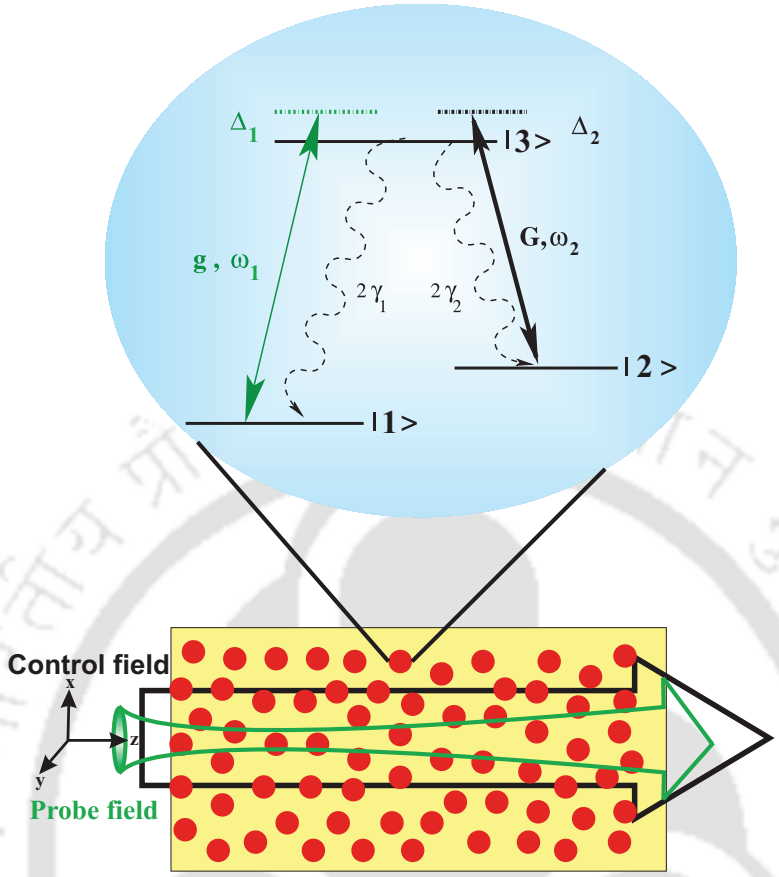

FIGURE 2.1: Schematic setup for the cloning of arbitrary images encoded in the spatial profile of a control field onto the spatial profile of a probe beam. Both fields co-propagate through a rubidium vapor cell, and couple to the atoms on the $|3\rangle \leftrightarrow \langle 1|$ (probe field with frequency ω_1) and $|3\rangle \leftrightarrow \langle 2|$ (control field with frequency ω_2) transitions, respectively. Our analysis includes the case in which both fields are equally strong.

The Rabi frequencies of the probe and control fields are defined as

$$g = \frac{\hat{\mathbf{d}}_{31} \cdot \hat{\mathbf{e}}_1 \mathcal{E}_1 e^{ik_1 z}}{\hbar}, \tag{2.3}$$

$$G = \frac{\hat{\mathbf{d}}_{32} \cdot \hat{\mathbf{e}}_2 \mathcal{E}_2 e^{ik_2 z}}{\hbar}. \tag{2.4}$$

Here, $\hat{\mathbf{d}}_{3j}$ are the corresponding dipole moment matrix elements. The master equation for the density operator ρ is given by

$$\dot{\rho} = -\frac{i}{\hbar}\left[\hat{H}, \rho\right] + \mathcal{L}_\gamma \rho. \tag{2.5}$$

The last term in Eq. (2.5) describes incoherent processes such as spontaneous emission and is determined by

$$\begin{aligned}\mathcal{L}_\gamma[\rho] = &-\gamma_1\left(|3\rangle\langle 3|\rho - 2|1\rangle\langle 1|\rho_{33} + \rho|3\rangle\langle 3|\right)\\ &-\gamma_2\left(|3\rangle\langle 3|\rho - 2|2\rangle\langle 2|\rho_{33} + \rho|3\rangle\langle 3|\right).\end{aligned} \tag{2.6}$$

We label the radiative decay rate from state $|3\rangle$ to ground state $|j\rangle$ by $2\gamma_j$.

Plugging the Hamiltonian of Eq. (2.2) into the master equation, we get equations of motion for the density matrix elements as the following

$$\dot{\rho}_{33} = -2(\gamma_1+\gamma_2)\rho_{33} + ige^{-i\omega_1 t}\rho_{13} - ig^* e^{i\omega_1 t}\rho_{31} + iGe^{-i\omega_2 t}\rho_{23} - iG^* e^{i\omega_2 t}\rho_{32}\,, \tag{2.7}$$

$$\dot{\rho}_{22} = 2\gamma_2\rho_{33} + iG^* e^{i\omega_2 t}\rho_{32} - iGe^{-i\omega_2 t}\rho_{23}\,, \tag{2.8}$$

$$\dot{\rho}_{32} = -\left[(\gamma_1+\gamma_2) + i\omega_{32}\right]\rho_{32} + ige^{-i\omega_1 t}\rho_{12} + iGe^{-i\omega_2 t}(\rho_{22}-\rho_{33})\,, \tag{2.9}$$

$$\dot{\rho}_{31} = -\left[(\gamma_1+\gamma_2) + i\omega_{31}\right]\rho_{31} + iGe^{-i\omega_2 t}\rho_{21} + ige^{-i\omega_1 t}(\rho_{11}-\rho_{33})\,, \tag{2.10}$$

$$\dot{\rho}_{21} = -\left[\Gamma + i\omega_{21}\right]\rho_{21} + iG^* e^{i\omega_2 t}\rho_{31} - ige^{-i\omega_1 t}\rho_{23}\,. \tag{2.11}$$

where $\omega_{32} = \omega_{a3} - \omega_{a2}$, $\omega_{31} = \omega_{a3} - \omega_{a1}$, and $\omega_{21} = \omega_{a2} - \omega_{a1}$.

We define the following transformations

$$\rho_{ii} = \sigma_{ii}\,,\quad \rho_{31} = \sigma_{31}e^{-i\omega_1 t}\,,\quad \rho_{32} = \sigma_{32}e^{-i\omega_2 t}\,,\quad \rho_{21} = \sigma_{21}e^{-i(\omega_1-\omega_2)t}\,. \tag{2.12}$$

In this suitable interaction picture, the density matrix equations follow as

$$\dot{\sigma}_{33} = -2(\gamma_1+\gamma_2)\sigma_{33} + ig\sigma_{13} - ig^*\sigma_{31} + iG\sigma_{23} - iG^*\sigma_{32}\,, \tag{2.13}$$

$$\dot{\sigma}_{22} = 2\gamma_2\sigma_{33} + iG^*\sigma_{32} - iG\sigma_{23}\,, \tag{2.14}$$

$$\dot{\sigma}_{32} = -\left[(\gamma_1+\gamma_2) + i\Delta_2\right]\sigma_{32} + ig\sigma_{12} + iG\sigma_{22} - iG\sigma_{33}\,, \tag{2.15}$$

$$\dot{\sigma}_{31} = -\left[(\gamma_1+\gamma_2) + i\Delta_1\right]\sigma_{31} + iG\sigma_{21} + ig\sigma_{11} - ig\sigma_{33}\,, \tag{2.16}$$

$$\dot{\sigma}_{21} = -\left[\Gamma - i(\Delta_2-\Delta_1)\right]\sigma_{21} + iG^*\sigma_{31} - ig\sigma_{23}\,. \tag{2.17}$$

The detunings of the probe and the control fields from the respective transition frequencies are defined as $\Delta_1 = \omega_{31} - \omega_1$ and $\Delta_2 = \omega_{32} - \omega_2$, respectively. We have further included pure dephasing of the ground state coherence, e.g., due to phase changing collisions, and denote

the total decay rate of the coherence by Γ. The remaining density matrix equations follow from the constraints $\sigma_{11} + \sigma_{22} + \sigma_{33} = 1$ and $\sigma_{ij} = \sigma^*_{ji}$.

2.1.2 Propagation equations for probe and control beams

We use Maxwell's wave equations to simulate the spatial evolution of the control and the probe beams through the medium, in order to study the effect of both diffraction and dispersion during the propagation. The wave equations for the probe ($j = 1$) and control ($j = 2$) fields can be written as

$$\left(\nabla^2 - \frac{1}{c^2}\frac{\partial^2}{\partial t^2}\right)\mathbf{E}_j = \frac{4\pi}{c^2}\frac{\partial^2 \mathbf{P}_j}{\partial t^2}, \tag{2.18}$$

where $\mathbf{P}_j$ are the macroscopic polarizations induced by the control and probe fields, respectively. They can be expressed in terms of both the atomic coherences as well as the susceptibility as

$$\begin{aligned}\mathbf{P}_j &= \mathcal{N}\left(\mathbf{d}_{3j}\sigma_{3j}e^{-i\omega_j t} + \text{c.c.}\right) \\ &= \left(\chi_{3j}\hat{\mathbf{e}}_j\mathcal{E}_j e^{-i\omega_j t} + \text{c.c.}\right),\end{aligned} \tag{2.19}$$

where $\mathcal{N}$ is the density of the atomic medium, and χ_{31} and χ_{32} are the susceptibilities for the response to the probe and control fields, respectively. In slowly varying envelope and paraxial wave approximation, Eqs. (2.1), (2.3), (2.4) and (2.18) lead to propagation equations for the two fields given by

$$\frac{\partial g}{\partial z} = \frac{i}{2k_1}\left(\frac{\partial^2}{\partial x^2} + \frac{\partial^2}{\partial y^2}\right)g + 2i\pi k_1\chi_{31}\, g\,, \tag{2.20}$$

$$\frac{\partial G}{\partial z} = \frac{i}{2k_2}\left(\frac{\partial^2}{\partial x^2} + \frac{\partial^2}{\partial y^2}\right)G + 2i\pi k_2\chi_{32}\, G\,. \tag{2.21}$$

The first terms in the parentheses on the right hand sides account for the diffraction. The second terms on the right hand sides are responsible for the dispersion and absorption of the both the control and probe beams. Note that the two propagation equations are coupled via the susceptibilities χ_{31} and χ_{32}.

2.1.3 Medium susceptibilities of probe and control beams

Next we calculate the response of the medium to the probe and control fields, characterized by the respective susceptibilities. Using Eqs. (2.19), one can readily obtain the susceptibility at the frequencies at ω_p and ω_c as

$$\chi_{31}(\omega_p) = \frac{\mathcal{N}|\hat{\mathbf{d}}_{31}|^2}{\hbar g}\sigma_{31}\,, \tag{2.22}$$

$$\chi_{32}(\omega_c) = \frac{\mathcal{N}|\hat{\mathbf{d}}_{32}|^2}{\hbar G}\sigma_{32}\,. \tag{2.23}$$

In steady state, the atomic coherences $\sigma_{31}(\omega_p)$ and $\sigma_{32}(\omega_c)$ are obtained from Eqs. (2.13)-(2.17) as

$$\sigma_{3j} = \frac{N_{3j}}{D}\,, \tag{2.24}$$

where the numerators N_{32}, N_{31} and the denominator D are listed below:

$$\begin{aligned} N_{31} =&(|G|^2(\gamma(i\gamma+\Delta_1)(\Gamma^2+(\Delta_2-\Delta_1)^2) \\ &+(\gamma(i\Gamma+\Delta_2-\Delta_1)+\Gamma(\Delta_2+\Delta_1))|g|^2+\gamma(i\Gamma+\Delta_2-\Delta_1)|G|^2)g) \end{aligned} \tag{2.25}$$

$$\begin{aligned} N_{32} =&(|g|^2(\gamma(i\gamma+\Delta_2)(\Gamma^2+(\Delta_2-\Delta_1)^2) \\ &+\gamma(i\Gamma-\Delta_2+\Delta_1)|g|^2+(\gamma(i\Gamma-\Delta_2\Delta_1)+\Gamma(\Delta_2+\Delta_1))|G|^2)G) \end{aligned} \tag{2.26}$$

$$\begin{aligned} D =&\gamma|g|^6+|g|^4\left[3|G|^2(\gamma+2\Gamma)+2\gamma(\gamma\Gamma+\Delta_1(\Delta_2-\Delta_1))\right] \\ &+\gamma|G|^2\left[2|G|^2(\gamma\Gamma+\Delta_2(\Delta_1-\Delta_2))+|G|^4+\left(\gamma^2+\Delta_2\right)((\Delta_2-\Delta_1)^2+\Gamma^2)\right] \\ &+|g|^2[|G|^2\left((4\gamma+\Gamma)\Delta_2^2+2\gamma\Gamma(2\gamma+3\Gamma)+2(\Gamma-4\gamma)\Delta_2\Delta_1+(4\gamma+\Gamma)\Delta_1^2\right) \\ &+3|G|^4(\gamma+2\Gamma)+\gamma(\gamma^2+\Delta_1^2)((\Delta_2-\Delta_1)^2+\Gamma^2)]\,. \end{aligned} \tag{2.27}$$

The expressions are rather complex, since we include the fields to all orders, in order to account for nonlinear effects. To simplify the expressions, we have assumed equal decay rates on the two transitions, $\gamma_1 = \gamma_2 = \gamma/2$.

2.1.4 Transverse beam profiles

In the main part of our result section, we will numerically propagate complex transverse beam profiles. But first, in order to interpret the effect of the beam profiles on the propagation, we

chose the transverse spatial profile of the control field as a Hermite-Gaussian mode. At $z = 0$, it can be written as,

$$G(x,y) = G_0\, H_m\left(\frac{x\sqrt{2}}{w_c}\right) H_n\left(\frac{y\sqrt{2}}{w_c}\right) \exp\left[-\frac{(x^2+y^2)}{w_c^2}\right]. \tag{2.28}$$

Here, G_0 is the input amplitude, and w_c is the width of the control field. The function H_k is a Hermite polynomial of order k, and the indices m and n determine the shape of the control field profile along the x and y directions, respectively. Since we want to consider the transfer of arbitrary spatial information, we will study different values of m, n in the following.

Similarly, the probe field is initially assumed to have a super-Gaussian transverse profile given by

$$g(x,y) = g_0\, \exp\left[-\frac{(x^2+y^2)^8}{w_p^{16}}\right]. \tag{2.29}$$

The initial peak amplitude and the width of the probe field are denoted by g_0 and w_p, respectively. Instead of choosing super Gaussian as an initial profile, the shape of the probe field can be consider any arbitrary shape such as a plane wave, Gaussian or hyperbolic shape . The desired spatial profile of the probe beam can be generated by using a spatial light modulator based on either liquid crystal or coherent EIT media [137].

2.2 Numerical simulation and Results

2.2.1 Spatial modulation of linear and nonlinear susceptibility

We now turn to our results and start by studying the probe and control field susceptibilities at frequencies ω_1 and ω_2 using Eq. (2.22) and Eq. (2.23). For this purpose, we first consider a super Gaussian probe field and a Gaussian control field [$m = 0, n = 0$ in Eq. (2.28)] such that the probe susceptibility becomes inhomogeneous along the transverse directions. Results are presented for two different cases of the initial field amplitudes. We denote the case $g_0 \ll G_0$ as the weak field limit, and $g_0 \sim G_0$ as the strong field case. In our numerical calculations, we choose $g_0 = 0.015\,\gamma$ and $g_0 = 0.15\,\gamma$ for the two cases, respectively.

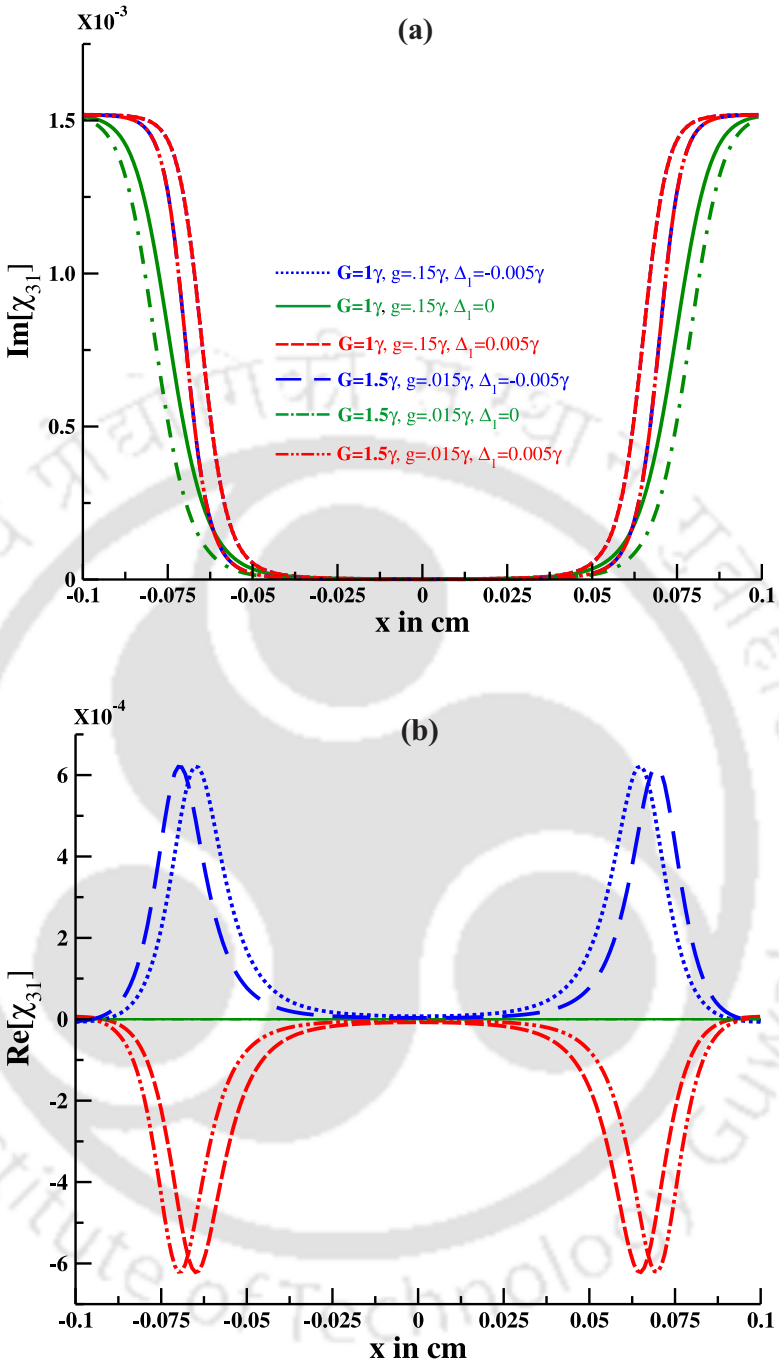

FIGURE 2.2: Probe beam susceptibility as a function of the transverse coordinate x. The control field has a Gaussian ($m = 0, n = 0$) beam profile. (a) shows the imaginary and (b) the real component of the susceptibility. The three different curves show probe field detunings $\Delta_1 = -0.005$ (blue dotted line, blue dashed line), $\Delta_1 = 0.0$ (green solid line, green dot-dashed line), and $\Delta_1 = 0.005\gamma$ (red dashed line, red dashed double-dot line) for two data sets of probe amplitudes $g = 0.015\gamma$ and $g = 0.15\gamma$, respectively. The other parameters are $y = 0.005$cm, $w_p = 150\mu$m, $w_c = 400\mu$m, $\Delta_2 = 0$, $\Gamma = 0.001\gamma$, and $\mathcal{N} = 5\times10^{11}$ atoms/cm^3.

Fig. 2.2 displays the spatial dependence of the probe field susceptibility. The different curves show Im(χ_{13}) and Re(χ_{13}) for three different detunings and both probe intensity cases as a function of x, with $y = 0.005$ cm. From Fig. 2.2(a), we find that the probe field is essentially transmitted without absorption in regions in which the control field amplitude is large, whereas in the wings ($|x| > 0.05$ cm) with low control field, strong absorption occurs. As expected, we found that the width of the transparency window depends on the intensities of the control and probe fields as well as the decay rate of ground state atomic coherence. Comparing the two intensity cases, we find that a relative increase of the probe field intensity results in steeper transitions between regions of high and low absorption. Later, we will show that this in turn leads to a smaller feature size of the image cloning scheme.

The transparency of the medium to the probe field can be understood as arising from coherent population trapping (CPT) or electromagnetically induced transparency (EIT), depending on the relative strength of the two applied fields. In both cases, destructive interference occurs between two different excitation pathways from $|1\rangle$ or $|2\rangle$ to the excited state $|3\rangle$. CPT and EIT are restricted to a certain transparency window. This transparency window can be controlled via the external parameters, and permits to transfer the transverse distribution of the control field onto the transmission profile of the probe field. This is the key mechanism of cloning the control field profile to the probe field.

The corresponding real part of the susceptibility is shown in Fig. 2.2(b). We notice that it can be controlled between negative and positive values via the detuning. For red detuning of the probe field ($\Delta_1 = 0.005\gamma$), it has a local maximum around $x = 0$, whereas for blue detuning, a minimum occurs around $x = 0$. For non-zero detunings, the real part becomes spatially dependent in particular around the regions in which the absorption undergoes a transition from low to high values.

Therefore, at red detuning, the transverse profile of the control field allows one to imprint a fiber-like refractive index gradient onto the atomic medium. This parabolic refractive index variation causes focusing of the probe field towards the center of the control field and also guides the probe field propagation along the propagation axis. Conversely, at blue detuning of the probe field, the real part has maxima at its wings, which is referred to as antiwaveguide like refractive index [184]. This antiwaveguide refractive index leads to shape distortions of the probe field. Hence, electromagnetically induced focusing and defocusing is possible in our setup by properly detuning the probe field. At two photon resonance condition, *i.e.*,

$\Delta_1 = \Delta_2 = 0$, only the imaginary part of the susceptibility varies spatially, while the real part is constant. Then the probe field propagates through the transparency window without being focused or defocused. Note that the probe field will nevertheless spread due to the inevitable diffraction.

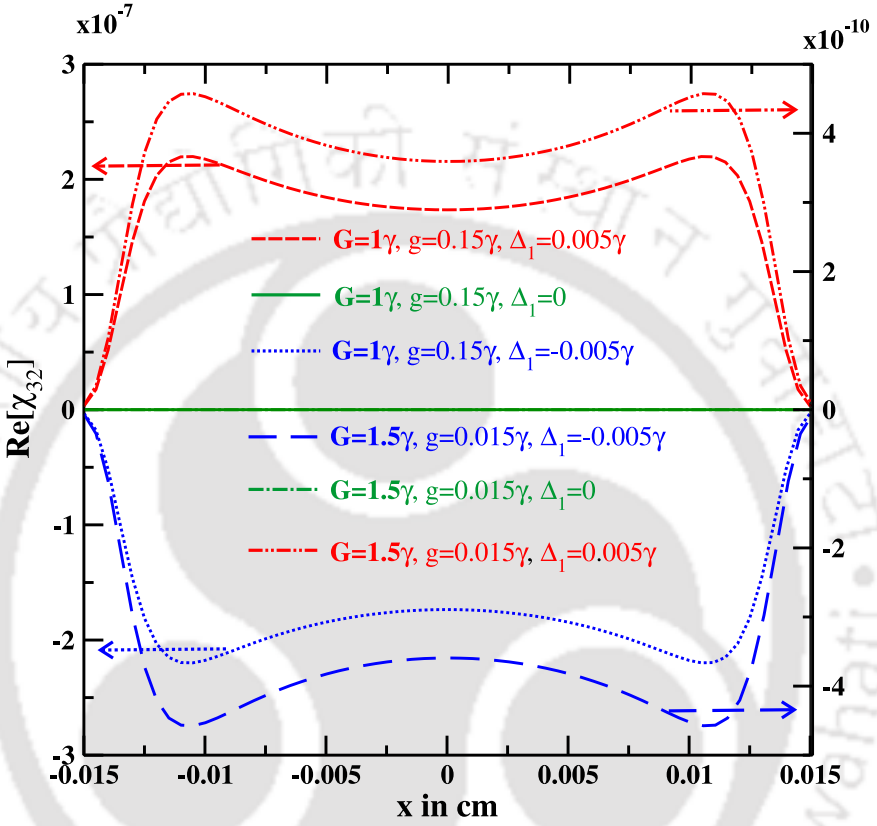

FIGURE 2.3: Real part of the control field susceptibility as a function of transverse position x. The control field has a Gaussian ($m = 0, n = 0$) shape. The three different curves show probe field detunings $\Delta_1 = -0.005$ (blue dotted line, blue dashed line), $\Delta_1 = 0.0$ (green solid line, green dot-dashed line), and $\Delta_1 = 0.005\gamma$ (red dashed line, red dashed double-dot line) for two data sets of probe amplitudes $g = 0.015\gamma$ and $g = 0.15\gamma$, respectively, with different scales of the axes. The other parameters are same as in Fig. 2.2.

Next, we consider the effect on the control field. Fig. 2.3 shows the real part of the susceptibility experienced by the control field. It in particular illustrates that it becomes especially important when the relative intensity of the probe and control fields are of comparable strength, as for the intense probe field case, the spatial dispersion of the control field is about

three orders of magnitude larger than in the weak probe field case. Hence, it is important to include atomic coherence effects in the paraxial wave equation for the control field.

It is also evident from Fig. 2.3 that in addition to the diffraction, the variation of the refractive index induces further distortions of the control field shape for both red- and blue-detuned probe fields. Our further analysis also showed that the absorption of the control field is rather low as compared to the probe field absorption in both cases, such that the control field can be propagated through the medium without significant absorption for relevant parameter ranges.

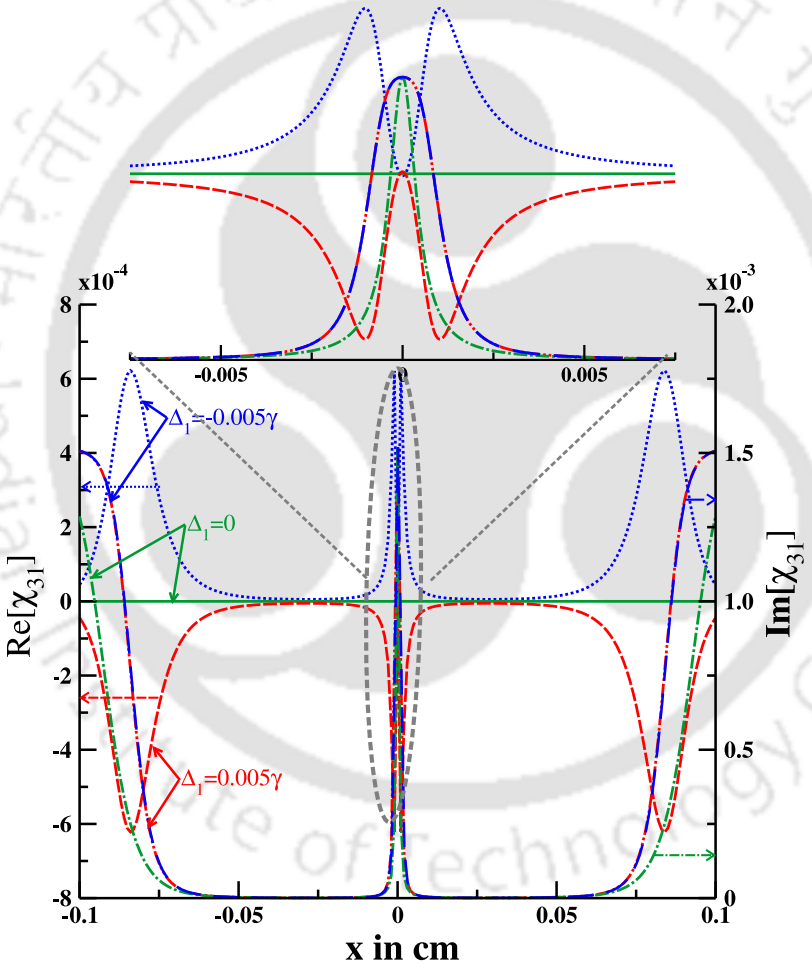

FIGURE 2.4: Probe field susceptibility as a function of the transverse spatial coordinate x. The control field has a doubly-peaked spatial profile characterized by $m = 1$ and $n = 0$ in Eq. (2.28). The central part around $x = 0$ is magnified in the inset in the top part of the figure. The other parameters are $y = 0.005$ cm, $G_0 = 1.5\gamma$, $g_0 = 0.015\gamma$, $w_p = 400\mu$m and $\mathcal{N} = 7.5\times10^{11}$ atoms/cm^3.

Finally, we analyze the dependence of the probe susceptibility on the control field transverse beam shape. Fig. 2.4 shows the transverse variation of the probe field susceptibility for a doubly peaked transverse spatial distribution of the control field obtained by setting $m = 1$ and $n = 0$ in Eq. (2.28). The central part of the figure is shown enlarged in the inset. Overall, the interpretation is similar to the case of a singly-peaked control field beam profile. But the doubly-peaked structure leads to the formation of two transparency windows. For positive probe detuning ($\Delta_1 = 0.005$), each of the transparency windows features a fiber-like refractive index, focusing the probe field towards the waist of the control field and thereby reducing the feature size. The generalization of these results to other spatial modes of the control field with different values of m, n is straightforward.

2.2.2 Propagation dynamics of probe and control beams

In this Section, we present results for the evolution of the spatial beam profile throughout the propagation. For this, we numerically integrate the full set of paraxial wave equations Eqs. (2.20) and (2.21) using a higher order split operator method given in Appendix A. We begin with a super-Gaussian probe beam shape and a Gaussian control beam shape to demonstrate the mapping of the control field profile onto the probe field. Results are shown in Fig. 2.5. Fig. 2.5(a) depicts the intensity profile of the probe beam at different propagation distances z. The initial field amplitudes are $G_0 = 1\gamma$ and $g_0 = 0.15\gamma$, corresponding to the strong probe field case. We find that the probe beam profile gradually acquires the control beam shape as it propagates through the medium. This process is completed at approximately $z = 2$ cm. Interestingly, the probe field width at this propagation distance is about 60 μm which is an order of magnitude less than the initial width of the control beam. At this distance, the Rayleigh length of the cloned probe beam is about 1.42 cm. Consequently, the cloned beam suffers from diffraction throughout the further propagation. We also notice from Fig. 2.5 that at two photon resonance condition $\Delta_1 = \Delta_2 = 0$, the probe beam experiences diffraction. In contrast, at red detuning, the probe field propagates unaltered through the medium. We thus find that the probe field diffraction can be controlled by a proper choice of the single photon detuning Δ_1 of the probe field.

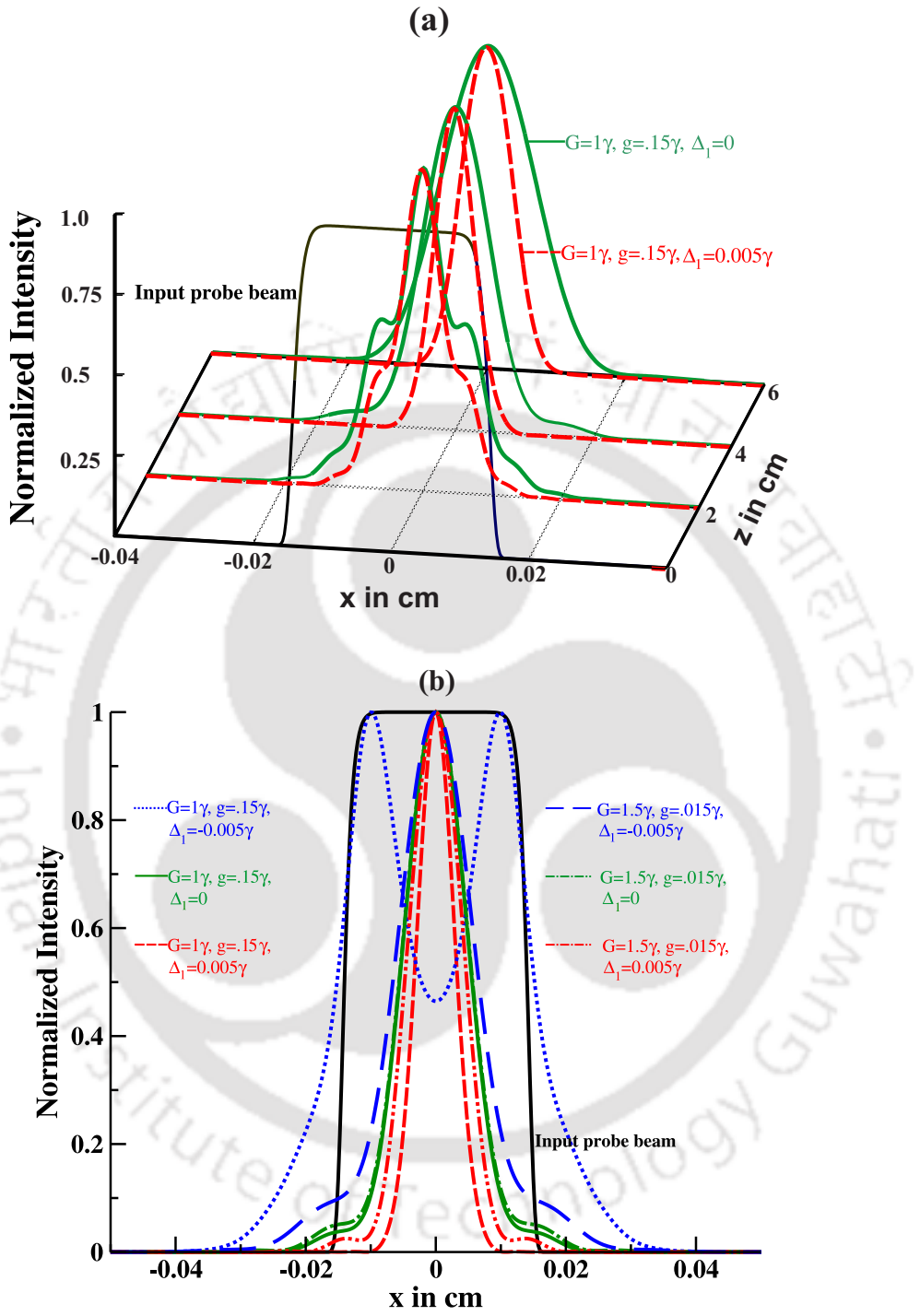

FIGURE 2.5: Normalized intensity profile of the propagating probe beam against against the transverse coordinate x for $y = 0$. (a) shows the beam profile at different propagation distances z. In (b), the transmitted probe beam intensity at the output of a 4 cm long medium is shown for different detunings. All other parameters are chosen as in Fig. 2.2.

Fig. 2.5(b) illustrates how the intensity and detuning of the probe field can be used to control the width of the transmitted probe beam. It shows that the probe beam is more tightly focused by a factor of about two for the strong control field case compared to the weak probe field case. At red detuning condition, our numerical computations show that the width and the transmission of the output probe beam are 85 μm [55 μm] and 20% [5%] for weak [strong] field case.

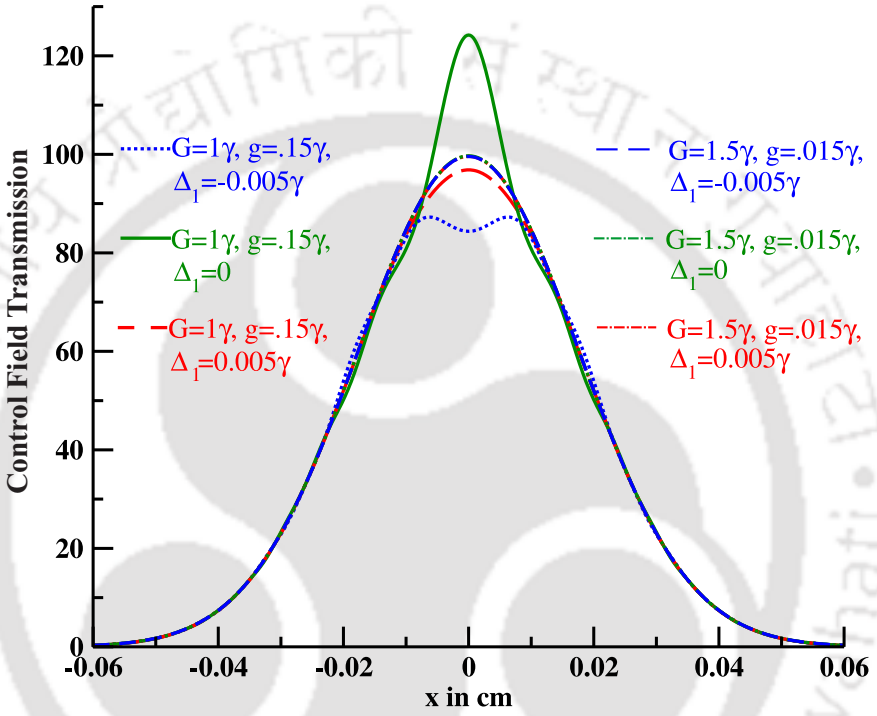

FIGURE 2.6: Spatial intensity profile of the control field as a function of the transverse coordinate x after propagation through a 4 cm long atomic medium. Results are shown for different field parameters. The profile is shown in the $y = 0$ plane. All other parameters are the same as in Fig. 2.5.

Fig. 2.6 show the corresponding results for the spatial variation of the transmitted control beam intensity profile in the $y = 0$ plane after propagation through a 4 cm long atomic medium. For the weak probe field case, the control field propagates essentially without any distortion. But in the strong probe field case, we find from Fig. 2.6 that the control field shape is distorted. Nevertheless, the integrated transmission intensity of the control field is approximately 100% in both cases.

Thus, we conclude that the control beam intensity is spatially redistributed in the strong probe field case. As a consequence, it is necessary to include the effect of atomic coherence in the propagation of the control field in the non-resonant as well as in the resonant condition for the strong probe field case.

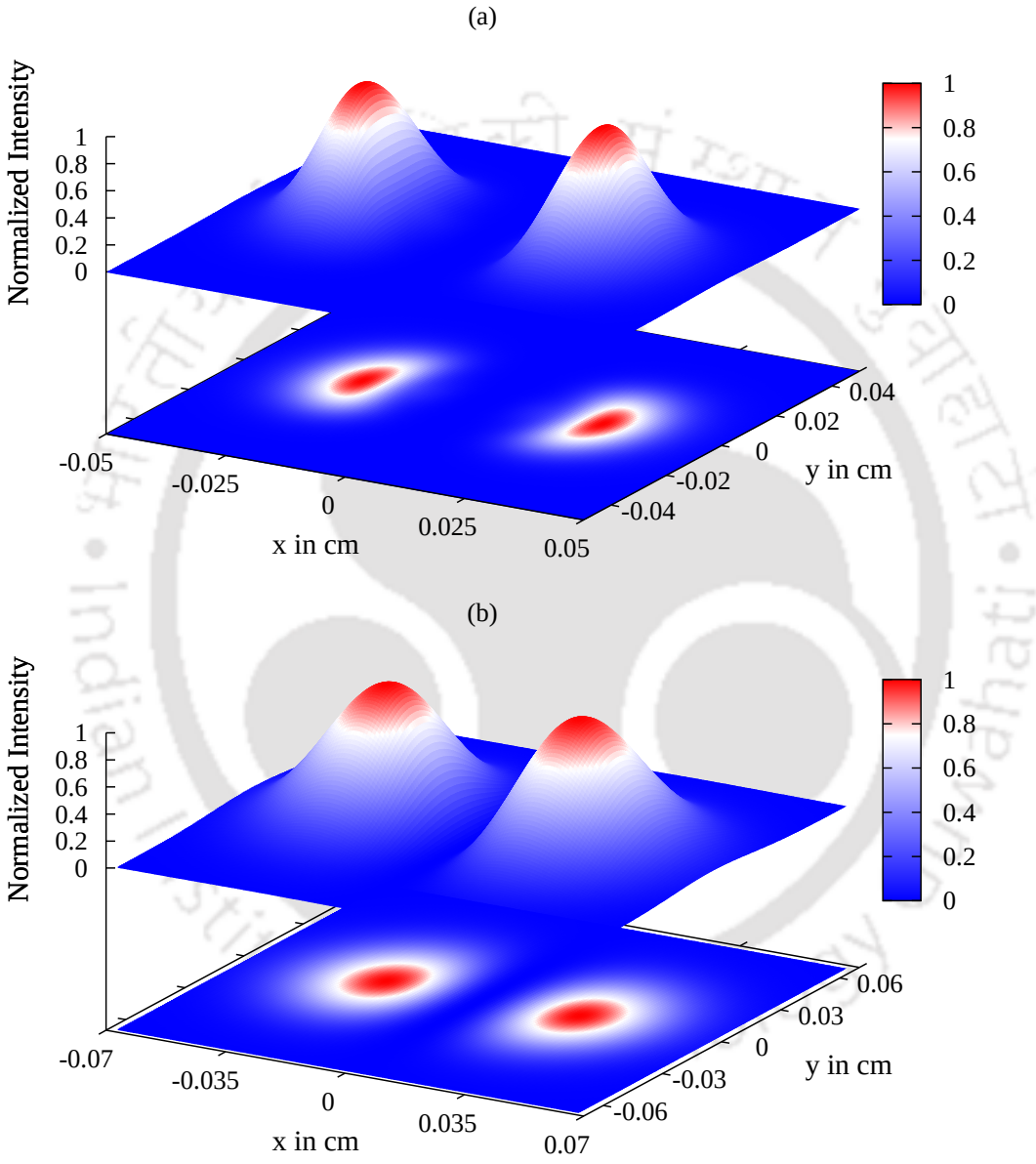

FIGURE 2.7: Transverse spatial intensity profile of the probe and control fields after propagation through an atomic vapor cell of length 4cm. The initial control field profile is chosen as a Hermite-Gaussian doubly-peaked profile. The top panel (a) shows the probe field, the bottom panel (b) for the control field. The parameters are as in Fig. 2.4.

Next, we study cloning of a two-peaked Hermite-Gaussian control beam onto the spatial profile of the probe beam. Fig. 2.7 shows the peak-normalized intensity of both the transmitted probe and control beams after a propagation distance of 4 cm. It can be seen from Fig. 2.7 that while the overall structure of the control beam is preserved, the width of the cloned probe beam profile is reduced by a factor of about 2.5 as compared to the initial width of the control beam. Therefore, the finesse of the transmitted probe beam is about 2.5 times greater than that of the control beam, which is consistent with the findings of an recent experiment by Li *et al* [153]. The integrated transmission intensity of the cloned output probe beam is 5% of the integrated intensity of the input probe beam. The transmission of the cloned beam can be increased by decreasing the optical density. We also found that the width of the cloned beam can be decreased by decreasing the relative intensity of the probe and control field giving us control over the finesse of the cloned probe beam.

Finally, Fig. 2.8 shows how a complex image encoded in the transverse control field intensity profile can efficiently be cloned onto the probe field. For this, we choose the three letters "CPT" as initial profile of the control beam, and a plane wave for the initial probe beam profile. We find from Fig. 2.8(b) that the control beam profile is significantly distorted after 3 cm propagation length through a vapor cell. This distortion arises from diffraction and from the variation of the refractive index experienced by the control field.

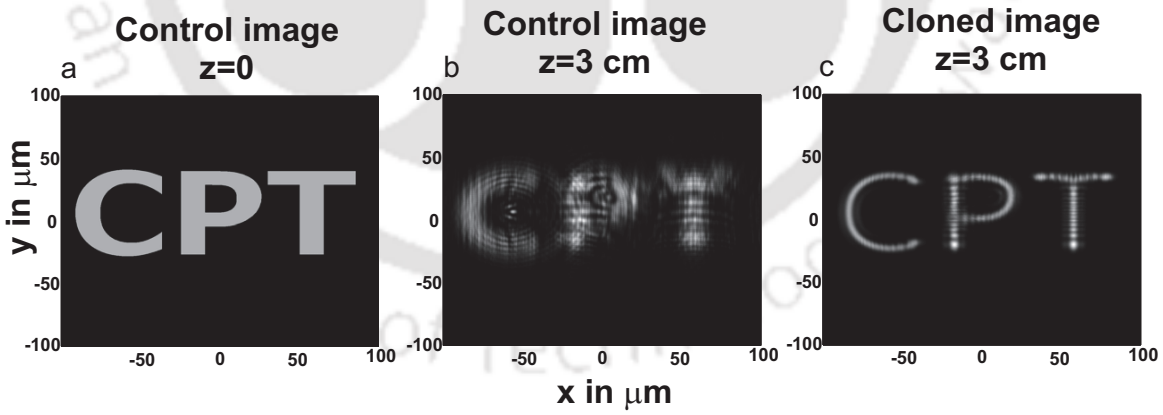

FIGURE 2.8: Transverse spatial intensity profile of the control and probe fields. (a) shows the initial profile of the control field at the medium entry. (b) shows the control field profile after propagation through a vapor cell of length 3cm filled with rubidium atoms. (c) shows the probe field profile after the propagation. Initially, the probe field is chosen as a plane wave. The parameters are $g = 0.15\gamma$, $G = 1.5\gamma$, $\Delta_2 = 0$, $\Delta_1 = 0.002\gamma$, $\Gamma = 0.001\gamma$, and $N = 10^{12}$ atoms/cm^3.

In contrast, the fiber-like spatial dispersion of the probe field can be used to compensate or to reverse the effect of the diffraction. As a result, the cloned image in the transverse profile of the probe beam is tightly focused. We further note from panel (c) that the feature size in the cloned image is reduced by a factor of 2 as compared to the incident control field image. This suggests that the finesse of the transmitted cloned image is two times greater then that of the incident control image. Hence, the feature size of the cloned image is decreased twofold.

2.3 Chapter conclusion

In conclusion, we have studied the possibility of cloning of an arbitrary images encoded in the spatial profile of a coupling beam onto a probe beam. Our method is based on coherent population trapping in a three-level atomic lambda system. We have considered both, weak probe fields and probe fields with strength comparable to the control field, and have discussed the differences for light propagation in the weak and strong field limits. In the "strong field limit" where the probe and control fields are of comparable strength, we firstly calculated the atomic susceptibilities including both linear and nonlinear effects for the two fields. We then found that a waveguide-like structure can be formed inside the medium at red detuning of the probe field when applying a Gaussian control and a super-Gaussian probe. At the same time, a transparency window centered in the waveguide, which can be controlled by changing the relative intensities of the probe and control fields. This transparency window allows to transfer the transverse intensity profile of the control onto the transmitted probe field. By numerically solving the propagation equations for both fields, we found that the spatial profile of the control is gradually mapped onto the transmitted probe already after a few Rayleigh lengths. Interestingly, the feature size in the spatial profile of the probe field is reduced compared to that of the original control field structure. In order to show that our method works for arbitrary images, different spatial profiles of the control and probe fields are considered. In particular, the three letters "CPT" initially encoded on the control field are cloned onto the transmission profile of the probe. In this process, the feature size is decreased by a factor of 2. Interestingly, even though cloning of arbitrary images onto the probe field is constructed nicely, the control field image is severely distorted due to diffraction throughout the propagation.

Chapter 3

Resolution improvement via double dark resonances

The ability to enhance spatial resolution of a Rayleigh [2] or Sparrow-limited [154] image is one of the main challenges in optics. Conventional optics has failed to resolve the characteristic size of an image beyond a value comparable to the wavelength of the probing light [155]. Main constraint of high resolution imaging comes from the diffraction and the absorption. The diffraction of an image is inevitable due to its geometrical origin. The above obstacles can completely or partially be eliminated by use of quantum interference effects.

Optical properties of medium tailored along the transverse direction can open up a new possibility of transferring the characteristic features of the control field to the probe field. This is because the propagation dynamics of probe field is dependent on the diffraction and dispersive properties of the medium. The diffraction and dispersion characteristics of the atomic medium can be manipulated by using proper spatially inhomogeneous control field. This concept has been demonstrated experimentally [153] in a CPT system where a well resolved control field structure is used for optical imaging. Further, the transmitted cloned image has feature size four times smaller as compared to the initial control image. However, EIT and CPT based schemes suffer from strong absorption due to breaking of two-photon resonance condition. Hence the absorption based mechanism limits practical implementation. Therefore, one can take advantages of gain based schemes to generate high resolution cloned image. Resolution of cloned image can be improved by engineering the contrast of

the refractive index of atomic waveguides of the gain medium. Quantum interference effects induced by interacting dark resonances have been shown to drastically increase the contrast of the refractive index profile [156].

In this chapter, we have used interacting dark resonances to imprint the Rayleigh- or Sparrow-limited control image to probe field with high resolution and contrast. To facilitate these processes, we use a four-level atomic system. A single dark state can be created by the control and the probe fields couple to the two arms of Λ-system. This interaction gives rise to usual single transparency window. The double-dark states can be generated by using a microwave or optical field which interacts with magnetic or electric dipole moments of relevant atomic transitions [157–159]. We find that the interference between two dark states results in a new sharp absorption peak at line centre. The double dark resonance (DDR) spectra show two transparency windows accompanied with one sharp absorption peak. Furthermore, we demonstrated that a very weak incoherent pump field is sufficient to turn the induced absorption dips to gain peaks. We exploit these sharp spectral features to write waveguide inside medium. We begin with Rayleigh-limited control field structure and do a comparative study of inhomogeneous susceptibility for EIT, Microwave induced absorption (MIA), and LWI. The result shows that the presence of three fields with an incoherent pump provides a sharp contrast in refractive index from core to cladding than other two cases. We efficiently use this sharp refractive index contrast for cloning the Rayleigh limited control field image to the probe field with high resolution. Finally, we also show that Sparrow limited three modes of the control image can also be cast onto the probe field with appreciable resolution and high transmission. Later, we also use induced absorption and transparency mechanism to demonstrate the spatial switching (off or on) of probe beam. The spatial optical beam switching based on spatial phase modulation has been discussed recently in optical lattice [160].

3.1 Theoretical Formulations

3.1.1 Atomic model system

In this work, we consider a homogeneously broadened four level Rb atomic system consisting of an excited state $|4\rangle$ and three metastable states $|1\rangle$, $|2\rangle$, and $|3\rangle$ interacting with two optical fields and one microwave field as shown in the Fig. 3.1. The excited state $|4\rangle$ is coupled

to two degenerate ground states $|1\rangle$, and $|3\rangle$ by two coherent fields, namely, a weak probe field with frequency ω_1 and a control field with frequency ω_2, respectively, which form a three level Λ-system. The ground state $|3\rangle$ is further coupled to the metastable state $|2\rangle$ by an additional microwave field with frequency ω_3. In the real experimental scenario of ^{87}Rb ($D_1 or D_2$ line) atomic vapor, the hyperfine magnetic sublevel of $5P_{1/2} : |F' = 2, m = 1\rangle$ serves as an excited state $|4\rangle$ in Fig. 3.1. The ground-state hyperfine magnetic sublevels of $5S_{1/2} : |F = 2, m = 2\rangle$, $|F = 1, m = 0\rangle$, and $|F = 2, m = 0\rangle$ correspond to states $|1\rangle$, $|2\rangle$, and $|3\rangle$, respectively [157, 158].

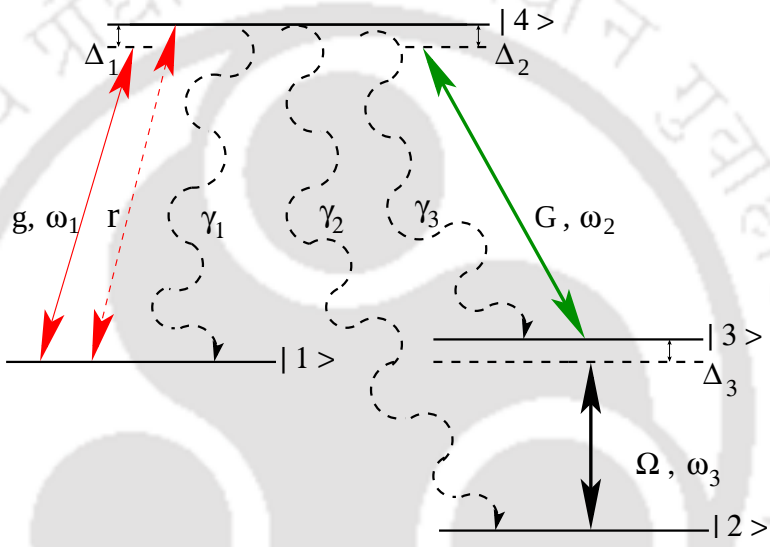

FIGURE 3.1: Schematic diagram of the four-level ^{87}Rb atomic system. The atomic transition $|4\rangle \leftrightarrow |1\rangle$ is coupled by the coherent probe field with Rabi frequency g and incoherent pump field r. The control field with Rabi frequency G interacts to the atomic transition $|4\rangle \leftrightarrow |3\rangle$. A microwave field with Rabi frequency Ω acts on the transition $|3\rangle \leftrightarrow |2\rangle$ to produce the double dark resonance of the system.

We define two copropagating optical fields along the z-axis as

$$\mathbf{E}_j(\mathbf{r}, t) = \hat{\mathbf{e}}_j \mathcal{E}_j(\mathbf{r})\, e^{-i(\omega_j t - k_j z)} + \text{c.c.}\,, \tag{3.1}$$

where $\mathcal{E}_j(\mathbf{r})$ is the slowing varying envelope, $\hat{e}_j$ is the unit polarization vector, ω_j is the laser field frequency and k_j is the wave number of field, respectively. The index $j \in \{1, 2\}$ denotes

the probe or control field, respectively. The microwave field is defined as

$$\mathbf{E}_3(\mathbf{r},t) = \hat{\mathbf{e}}_3\mathcal{E}_3(\mathbf{r})\, e^{-i(\omega_3 t - k_3 z)} + \text{c.c.}\,, \tag{3.2}$$

where, $\mathcal{E}_3(\mathbf{r})$ is constant amplitude, ω_3 is the frequency of the microwave field. In the presence of three coherent fields, the Hamiltonian of the system under the electric dipole and rotating-wave approximation can be expressed as,

$$\hat{H} = \hat{H}_0 + \hat{H}_I\,, \tag{3.3}$$

$$\hat{H}_0 = \hbar\omega_{43}|4\rangle\langle 4| - \hbar\omega_{23}|2\rangle\langle 2| - \hbar\omega_{13}|1\rangle\langle 1|\,, \tag{3.4}$$

$$\begin{aligned}\hat{H}_I = &-(|4\rangle\langle 1|\mathbf{d}_{41}\cdot\hat{\mathbf{e}}_1\mathcal{E}_1 e^{-i(\omega_1 t - k_1 z)} \\ &+ |4\rangle\langle 3|\mathbf{d}_{43}\cdot\hat{\mathbf{e}}_2\mathcal{E}_2 e^{-i(\omega_2 t - k_2 z)} \\ &+ |3\rangle\langle 2|\mathbf{d}_{32}\cdot\hat{\mathbf{e}}_3\mathcal{E}_3 e^{-i(\omega_3 t - k_3 z)} + \text{H.c.})\,.\end{aligned} \tag{3.5}$$

The time dependent parts of the above Hamiltonian can be removed by using of following unitary transformation,

$$\hat{U} = e^{-\frac{i}{\hbar}Wt}\,, \tag{3.6}$$

$$W = \hbar\omega_2|4\rangle\langle 4| - \hbar\omega_3|2\rangle\langle 2| - \hbar(\omega_1-\omega_2)|1\rangle\langle 1|\,. \tag{3.7}$$

If $|\psi(\mathbf{r},t)\rangle$ represents the state vector in the stationary frame and and $|\phi(\mathbf{r},t)\rangle$ in the rotating frame, then they can be espressed as

$$|\psi(\mathbf{r},t)\rangle = \hat{U}|\phi(\mathbf{r},t)\rangle\,. \tag{3.8}$$

Using above unitary transformation into the Schrödinger equation Eq. (1.19) and after rearranging the terms, we obtain

$$i\hbar\frac{\partial}{\partial t}|\phi(\mathbf{r},t)\rangle = (\hat{U}^\dagger\hat{H}\hat{U} - i\hbar\hat{U}^\dagger\frac{\partial\hat{U}}{\partial t})|\phi(\mathbf{r},t)\rangle = \hat{V}|\phi(\mathbf{r},t)\rangle\,, \tag{3.9}$$

where the transformed Hamiltonian $\hat{V}$ is given by

$$\begin{aligned}\hat{V}/\hbar = &-\Delta_2|4\rangle\langle 4| + \Delta_3|2\rangle\langle 2| + (\Delta_1-\Delta_2)|1\rangle\langle 1| \\ &-(g|4\rangle\langle 1| + G\,|4\rangle\langle 3| + \Omega\,|3\rangle\langle 2| + \text{H.c.})\,,\end{aligned} \tag{3.10}$$

where $\Delta_1 = \omega_1 - \omega_{41}$, $\Delta_2 = \omega_2 - \omega_{43}$, $\Delta_3 = \omega_2 - \omega_{32}$ are the single-photon detunings and

$$g = \frac{\mathbf{d}_{41} \cdot \hat{\mathbf{e}}_1 \mathcal{E}_1 e^{ik_1 z}}{\hbar}, \quad G = \frac{\mathbf{d}_{43} \cdot \hat{\mathbf{e}}_2 \mathcal{E}_2 e^{ik_2 z}}{\hbar}, \quad \Omega = \frac{\mathbf{d}_{32} \cdot \hat{\mathbf{e}}_1 \mathcal{E}_3 e^{ik_3 z}}{\hbar}$$

are the Rabi frequencies of the probe, control and the microwave fields, respectively. The atomic transition frequencies and the corresponding dipole moment matrix elements are denoted by ω_{ij} and $\mathbf{d}_{ij}$, respectively.

3.1.2 Dynamical equations for density matrix elements

We use Liouville equation to incorporate the coherent and incoherent processes of the atomic system. Thus the dynamics of the system is governed by the following Liouville equation

$$\dot{\rho} = -\frac{i}{\hbar}\left[\hat{V}, \rho\right] + \mathcal{L}\rho\,, \tag{3.11}$$

where the second term represents the incoherent processes that can be determined by

$$\mathcal{L}\rho = \mathcal{L}_\gamma \rho + \mathcal{L}_d \rho + \mathcal{L}_r \rho\,, \tag{3.12}$$

with

$$\begin{aligned}
\mathcal{L}_\gamma \rho &= -\sum_{i=1}^{3} \frac{\gamma_i}{2} \left(|4\rangle\langle 4|\rho - 2|i\rangle\langle i|\rho_{44} + \rho|4\rangle\langle 4|\right)\,, \\
\mathcal{L}_d \rho &= -\sum_{i=1}^{3}\sum_{i\neq j=1}^{3} \frac{\gamma_c}{2} \left(|i\rangle\langle i|\rho - 2|j\rangle\langle j|\rho_{ii} + \rho|i\rangle\langle i|\right)\,, \\
\mathcal{L}_r \rho &= \mathcal{L}_{14}\rho + \mathcal{L}_{41}\rho\,, \\
\mathcal{L}_{14}\rho &= -\frac{r}{2}\left(|4\rangle\langle 4|\rho - 2|1\rangle\langle 1|\rho_{44} + \rho|4\rangle\langle 4|\right)\,, \\
\mathcal{L}_{41}\rho &= -\frac{r}{2}\left(|1\rangle\langle 1|\rho - 2|4\rangle\langle 4|\rho_{11} + \rho|1\rangle\langle 1|\right)\,.
\end{aligned}$$

The first term of Eq. (3.12) refers to the radiative decay from excited state $|4\rangle$ to ground states $|j\rangle$ as labelled by γ_j. The second term, $\mathcal{L}_d\rho$, represents pure dephasing for the coherence ρ_{ij} due to collision with rate γ_c. The incoherent pumping between levels $|1\rangle$ and $|4\rangle$ with rate r is described by $\mathcal{L}_r\rho$.

The dynamics of the population and atomic coherences in the four-level system can be described by the following set of density matrix equations:

$$\dot{\rho}_{11} = -r\rho_{11} + r\rho_{44} + \gamma_1\rho_{44} + ig^*\rho_{41} - ig\rho_{14}\,, \tag{3.13}$$

$$\dot{\rho}_{22} = \gamma_2\rho_{44} + i\Omega^*\rho_{32} - i\Omega\rho_{23}\,, \tag{3.14}$$

$$\dot{\rho}_{33} = \gamma_3\rho_{44} + i\Omega\rho_{23} - i\Omega^*\rho_{32} + iG^*\rho_{43} - iG\rho_{34}\,, \tag{3.15}$$

$$\dot{\rho}_{44} = -\dot{\rho}_{11} - \dot{\rho}_{22} - \dot{\rho}_{33}\,, \tag{3.16}$$

$$\dot{\rho}_{21} = -\left[\frac{r}{2} + \gamma_{21} - i(\Delta_1 - \Delta_2 - \Delta_3)\right]\rho_{21} + i\Omega^*\rho_{31} - ig\rho_{24}\,, \tag{3.17}$$

$$\dot{\rho}_{23} = -\left[\gamma_{23} + i\Delta_3\right]\rho_{23} - iG\rho_{24} + i\Omega^*(\rho_{33} - \rho_{22})\,, \tag{3.18}$$

$$\dot{\rho}_{24} = -\left[\gamma_{24} + i(\Delta_2 + \Delta_3)\right]\rho_{24} - ig^*\rho_{21} - iG^*\rho_{23} + i\Omega^*\rho_{34}\,, \tag{3.19}$$

$$\dot{\rho}_{31} = -\left[\frac{r}{2} + \gamma_{31} + i(\Delta_2 - \Delta_1)\right]\rho_{31} + i\Omega\rho_{21} - ig\rho_{34} + iG^*\rho_{41}\,, \tag{3.20}$$

$$\dot{\rho}_{34} = -\left[\gamma_{34} + i\Delta_2\right]\rho_{34} - ig^*\rho_{31} + i\Omega\rho_{24} - iG^*(\rho_{33} - \rho_{44})\,, \tag{3.21}$$

$$\dot{\rho}_{41} = -\left[\frac{r}{2} + \gamma_{41} - i\Delta_1\right]\rho_{41} + iG\rho_{31} + ig(\rho_{11} - \rho_{44})\,, \tag{3.22}$$

$$\dot{\rho}_{ij} = \dot{\rho}^*_{ji}\,, \tag{3.23}$$

where the overdots stand for time derivatives and " $*$ " denotes complex conjugate. The total dephasing rate of the atomic coherences is given by $\gamma_{ij} = \gamma_c + \gamma_i/2$.

3.1.3 Solution of density matrix equations under perturbative approach

We adopt steady state solutions of the master Eqs. (3.13)-(3.23) to study the response of the medium. These equations can be solved to all orders in the control and probe field provided both the fields have approximately equal amplitude. However, we restrict ourselves to cases where the probe field is much weaker than the control field and microwave field. This allows us to apply a perturbative approach in order to determine an approximate solution. Thus in the spirit of weak probe field limit, we calculate the coherences and populations to the first order in g and to all order in control field G and microwave field Ω. Hence the steady state solutions of the density matrix equations can be written in a following expansion form

$$\rho_{ij} = \rho_{ij}^{(0)} + g\rho_{ij}^{(+)} + g^*\rho_{ij}^{(-)}, \tag{3.24}$$

where $\rho_{ij}^{(0)}$ describes zeroth order term of the solution in the absence of the probe field. The second and third terms denote the solutions at positive and negative frequencies of the probe field respectively. We now substitute the above expression in Eqs. (3.13)-(3.23) and equate the coefficients of g, g^* and the constant terms. Thus, we obtain a set of sixteen coupled simultaneous equations. The zeroth order solutions of simultaneous equations which are relevant for coherence ρ_{ij} are given by

$$\rho_{11}^{(0)} = \frac{[2(r+\gamma)|G|^2\Omega^2\{\gamma(\Gamma\gamma+|G|^2)+\Gamma[(\Delta_2+\Delta_3)^2+\Omega^2]\}]}{D} \tag{3.25}$$

$$\begin{aligned}\rho_{22}^{(0)} = {} & [r(\gamma|G|^6+|G|^4(2\Gamma\gamma^2-2\gamma\Delta_2\Delta_3-2\gamma\Delta_3^2+\Gamma\Omega^2-\gamma\Omega^2) \\ & +2\Gamma\Omega^2[\Delta_2^4+2\Delta_2^3\Delta_3+\gamma^2\Delta_3^2+\Delta_2^2(2\gamma^2+\Delta_3^2-2\Omega^2)+2\Delta_2\Delta_3(\gamma^2-\Omega^2)+(\gamma^2+\Omega^2)^2] \\ & +|G|^2\{\gamma\Delta_3^4+(\gamma^2+\Omega^2)[\Gamma^2\gamma-(\Gamma-2\gamma)\Omega^2]+\Delta_3^2[\gamma(\Gamma^2+\gamma^2)+2(\Gamma+2\gamma)\Omega^2] \\ & +\Delta_2^2[\Gamma^2\gamma+\gamma\Delta_3^2+(5\Gamma+2\gamma)\Omega^2]+\Delta_2\Delta_3[2\Gamma^2\gamma+2\gamma\Delta_3^2+(7\Gamma+6\gamma)\Omega^2]\})]/D\end{aligned} \tag{3.26}$$

$$\begin{aligned}\rho_{33}^{(0)} = {} & (r\Omega^2\{2\Gamma\Delta_2^4+4\Gamma\Delta_2^3\Delta_3+\Delta_3^2[2\Gamma\gamma^2+(2\Gamma+\gamma)|G|^2] \\ & +\Delta_2^2[2\Gamma\Delta_3^2+(3\Gamma+2\gamma)|G|^2+4\Gamma(\gamma^2-\Omega^2)]+\Delta_2\Delta_3[(5\Gamma+2\gamma)|G|^2+4\Gamma(\gamma^2-\Omega^2)] \\ & +[|G|^2+2(\gamma^2+\Omega^2)][(\gamma|G|^2+\Gamma(\gamma^2+\Omega^2)]\})/D\end{aligned} \tag{3.27}$$

$$\rho_{44}^{(0)} = \frac{(2r|G|^2\Omega^2\{\gamma(\Gamma\gamma+|G|^2)+\Gamma[(\Delta_2+\Delta_3)^2+\Omega^2]\})}{D} \tag{3.28}$$

$$\begin{aligned}D = {} & (r\gamma|G|^6+|G|^4\{2r\gamma[\Gamma\gamma-\Delta_3(\Delta_2+\Delta_3)]+[2\gamma^2+r(\Gamma+4\gamma)]\Omega^2\} \\ & +4r\Gamma\Omega^2\{(\gamma^2+\Delta_2^2)[\gamma^2+(\Delta_2+\Delta_3)^2]+2[\gamma^2-\Delta_2(\Delta_2+\Delta_3)]\Omega^2+\Omega^4\} \\ & +|G|^2\{r\gamma(\Gamma^2+\Delta_3^2)[\gamma^2+(\Delta_2+\Delta_3)^2]+\{\gamma[2\Gamma\gamma^2+r(\Gamma+2\gamma)^2] \\ & +2[\Gamma\gamma+2r(3\Gamma+\gamma)]\Delta_2^2+4(5r\Gamma+2r\gamma+\Gamma\gamma)\Delta_2\Delta_3 \\ & +(8r\Gamma+5r\gamma+2\Gamma\gamma)\Delta_3^2\}\Omega^2+2[\Gamma\gamma+2r(\gamma+\Gamma)]\Omega^4\}).\end{aligned} \tag{3.29}$$

Now, the linear-order atomic coherence $\rho_{41}^{(+)}$ which will yield susceptibility χ_{41} at frequency ω_1 is found as

$$\rho_{41}^{(+)} = i\left(\frac{(\Gamma_{21}\Gamma_{31}+\Omega^2)(\rho_{11}^{(0)}-\rho_{44}^{(0)})+A|G|^2}{\Gamma_{41}(\Gamma_{21}\Gamma_{31}+\Omega^2)+\Gamma_{21}|G|^2}\right), \tag{3.30}$$

with

$$A = \frac{B(\rho_{44}^{(0)} - \rho_{33}^{(0)}) + C(\rho_{33}^{(0)} - \rho_{22}^{(0)})}{(\Gamma_{23}(\Gamma_{24}\Gamma_{34} + \Omega^2) + |G|^2)},$$
$$B = (\Gamma_{21}(\Gamma_{23}\Gamma_{24} + |G|^2) - \Gamma_{23}\Omega^2),$$
$$C = (\Gamma_{21} + \Gamma_{34})\Omega^2,$$

where $\Gamma_{21} = [r/2 + \gamma_{21} - i(\Delta_1 - \Delta_2 - \Delta_3)]$, $\Gamma_{23} = [\gamma_{23} + i\Delta_3]$, $\Gamma_{24} = [\gamma_{24} + i(\Delta_2 + \Delta_3)]$, $\Gamma_{31} = [r/2 + \gamma_{31} + i(\Delta_2 - \Delta_1)]$, $\Gamma_{34} = [\gamma_{34} - i\Delta_2]$, and $\Gamma_{41} = [r/2 + \gamma_{41} - i\Delta_1]$. For the simplicity, we have assumed equal decay rates from excited state, $\gamma_1 = \gamma_2 = \gamma_3 = \gamma$ and coherence dephasing rates $\gamma_{41} = \gamma_{24} = \gamma_{34} \approx \gamma$, $\gamma_{21} = \gamma_{31} = \gamma_{23} \approx \gamma_c = \Gamma$. We now express the macroscopic polarization of the medium in terms of both the atomic coherences as well as the susceptibility as

$$\begin{aligned}\mathbf{P}_1 &= \mathcal{N}\left(\mathbf{d}_{41}\rho_{41}^{(+)}e^{-i\omega_1 t} + \text{c.c.}\right) \\ &= \left(\chi_{41}\hat{\mathbf{e}}_1\mathcal{E}_1 e^{-i\omega_1 t} + \text{c.c.}\right),\end{aligned} \tag{3.31}$$

where $\mathcal{N}$ is the density of the atomic medium. Now Eq. (3.30) and (3.31), will yield the linear response of the medium as

$$\chi_{41}(\Delta_1) = \frac{\mathcal{N}|\mathbf{d}_{41}|^2}{\hbar}\rho_{41}^{(+)}. \tag{3.32}$$

The real and imaginary parts of the susceptibility χ_{41} in Eq. (3.32) gives the dispersion and absorption of the medium respectively. The optical properties of the medium can be manipulated coherently by proper consideration of spatial shape and intensity of the different applied fields. The effect of different fields such as optical, microwave and incoherent pump field on the medium properties are in sequence in the results and discussions section.

3.1.4 Beam propagation equations

The spatial dynamics of the probe and control fields along the z-direction of the medium is governed by the Maxwell's wave equations. The wave equation under slowly varying envelope and paraxial wave approximations can result the beam propagation equation. The spatial

evolution equations for the probe and control fields are obtained as

$$\frac{\partial g}{\partial z} = \frac{i}{2k_1}\left(\frac{\partial^2}{\partial x^2} + \frac{\partial^2}{\partial y^2}\right) g + 2i\pi k_1 \chi_{41}\, g\,, \tag{3.33}$$

$$\frac{\partial G}{\partial z} = \frac{i}{2k_2}\left(\frac{\partial^2}{\partial x^2} + \frac{\partial^2}{\partial y^2}\right) G\,. \tag{3.34}$$

The terms within the parentheses on the right hand side of Eq. (3.33) and Eq. (3.34) are related with transverse variation of the laser beam. These terms account for the diffraction either in free space or in the medium.

The second term on the right hand side of Eq. (3.33) is responsible for the dispersion and absorption or gain of the probe beam. As we have seen in the previous chapter the effects of the atomic coherences on the control beam propagation are very negligible under the weak probe field. Therefore, we study the effect of both diffraction and dispersion for the spatial evolution of the probe beam where we include only the effect of diffraction for the control beam dynamics.

3.2 Results and Discussions

3.2.1 Susceptibility with homogeneous fields

We first study the atomic coherences by using homogeneous optical and microwave fields at steady-state condition. The quantum interference of atomic coherences induces EIT, MIA and LWI in our system. The characteristic of these quantum interference phenomena is illustrated in Fig. 3.2. In Fig. 3.2(a) we have plotted the variations of the imaginary part of the probe susceptibility with probe field detuning Δ_1 in the presence and absence of both microwave and incoherent pump fields. In the absence of both microwave and incoherent pump fields four-level system reduces to three-level Λ system with a weak probe and a strong control field. The probability amplitudes of two arms of the Λ system leads to destructive interference. This interference enable us to cancellation of absorption of probe field provided two-photon resonance condition is fulfilled as shown in Fig. 3.2. This phenomenon is known as EIT. In EIT, a single transparency window is accompanied by two absorptive peaks which originates from the strong control field. Now this single transparency window can be split into double

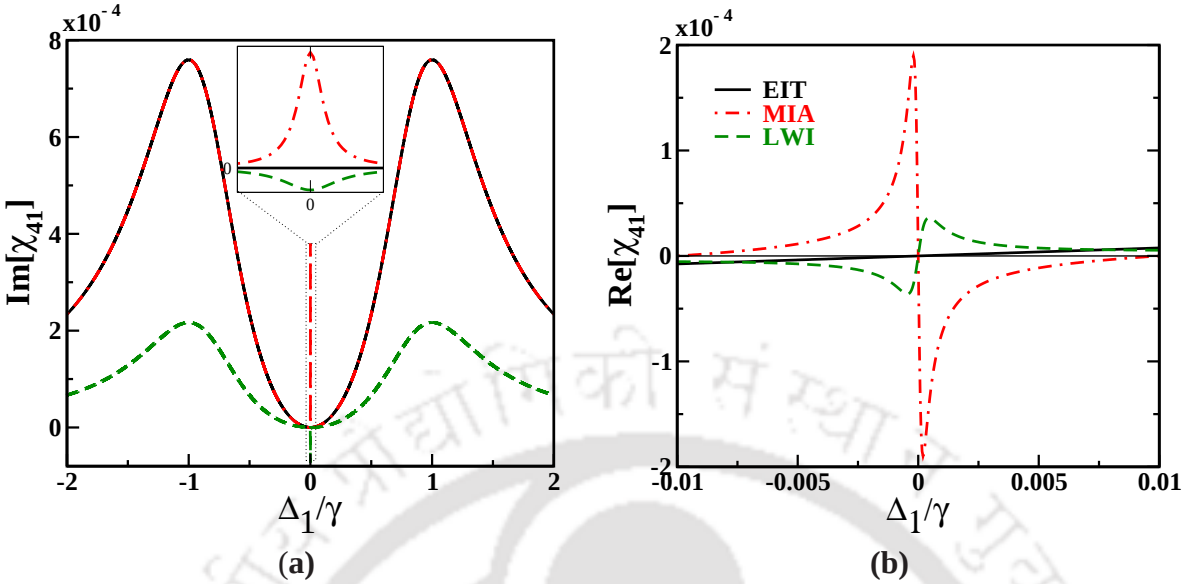

FIGURE 3.2: Variations of imaginary (a) and real (b) parts of the probe susceptibility with the detuning Δ_1 in the presence and absence of both microwave field and incoherent pump is plotted. The zoomed part of the absorption spectrum corresponds to medium loss, gain or transparency at the line center is shown in the inset. The corresponding parameters for these regimes are: $\Omega = 0.01\gamma$, $r = 0$ (red dot-dashed line), $\Omega = 0.01\gamma$, $r = 0.0005\gamma$ (green dashed line), and $\Omega = 0\gamma$, $r = 0$ (black solid line). The common parameters are $G = 1.0\gamma$, $\Delta_2 = \Delta_3 = 0$, $\Gamma = 0.0001\gamma$, $\gamma = 3\pi \times 10^6$ rad/sec, $\lambda = 795$ nm, and $\mathcal{N} = 5{\times}10^{11}$ atoms/cm^3.

transparency windows by the use of the microwave field. It is clear from Fig. 3.2(a) that the double transparency window is accompanied with very narrow absorption peak. This peak occurs due to the double dark states formed by microwave field at three-photon resonance condition. Furthermore, the position and width of these two transparency windows strongly depend on the intensity of microwave field. Now a relatively weak incoherent pump acting along the probe transition can switch the absorption peak to the gain dip. The second term in the numerator of Eq. (3.30) is responsible for gain around line center. This gain characteristic is illustrated by green dashed line line in Fig. 3.2(a). At three photon resonance the second term is negative and is lager than the first term which changes the properties of the medium from absorption into gain. Thus the presence of both weak microwave and incoherent pump fields is able to produce a gain window for the medium. Fig. 3.2(b) clearly shows sharp variation in refractive index due to DDR as compared to single dark resonance. This steep variation in refractive index has been used to separate out the diffraction-limited Rayleigh or Sparrow images.

3.2.2 Susceptibility with inhomogeneous control field

In this section, we discuss the effect of spatial inhomogeneous field on linear susceptibility given in Eq. (3.32). For this purpose, we change the control field profile from homogeneous to spatially inhomogeneous field while keeping rest of the fields as homogeneous for further study. The spatially inhomogeneous transverse profile of the control field is a combination of more than one Gaussian peak. At $z = 0$, the control beam can be written as,

$$G(x,y) = G_0 \sum_{i=1}^{n} \exp\left[-\frac{(x-a_i)^2 + y^2}{w_c^2}\right], \tag{3.35}$$

where G_0 is initial peak amplitude, w_c is beam width and a_i are the individual peak position. The full-width-at-half-maximum (FWHM) of individual peak is $\sqrt{2ln(2)}w_c$.

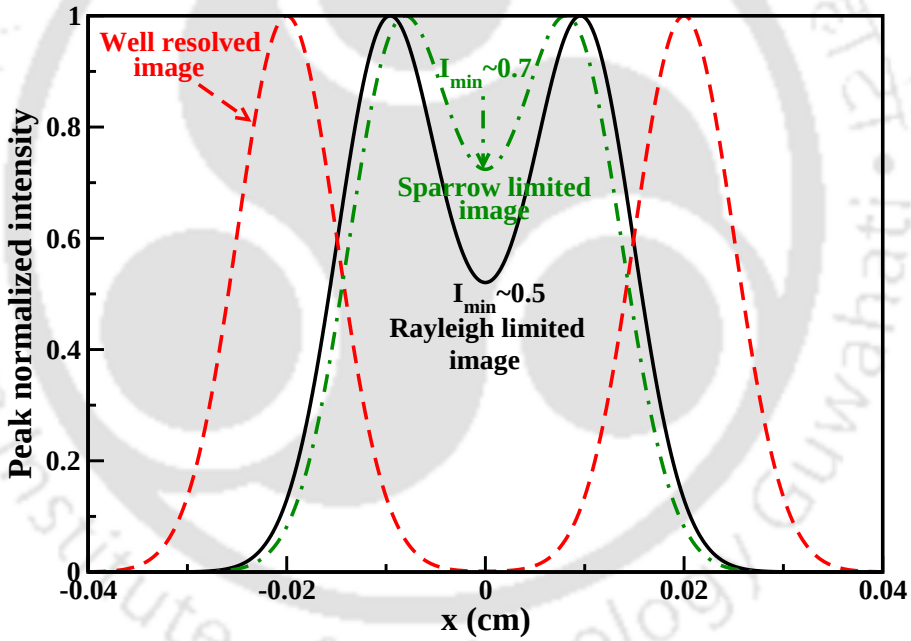

FIGURE 3.3: Spatial intensity variation of the control image is plotted against the transverse axis x with $y = 0$ at entry face of the vapor cell. The Rayleigh limited and Sparrow limited control image are formed by choosing $a_1 = -a_2 = 0.01$ cm and $a_1 = -a_2 = 0.009$ cm, respectively. The individual peaks can be well resolved by changing $a_1 = -a_2 = 0.02$ cm. The common parameters of two graphs are $G_0 = 1\gamma$, and $w_c = 100\ \mu$m.

Fig. 3.3 shows the intensity distribution of the control field against radial position x at the entry face of the medium. The overlapping of two peaks gives rise to a central minimum with non-zero intensity as shown in Fig. 3.3. The Rayleigh-limited or Sparrow limited control field images can be formed when the intensity of the peak normalized central minimum is $I_{min} \sim 0.5$ or ~ 0.7, respectively. The resolution of the diffraction limited images can be improved by reducing the central minimum intensity to zero. Thus, by increasing the peak separation or by decreasing the width of the individual peak enables to create high resolution image.

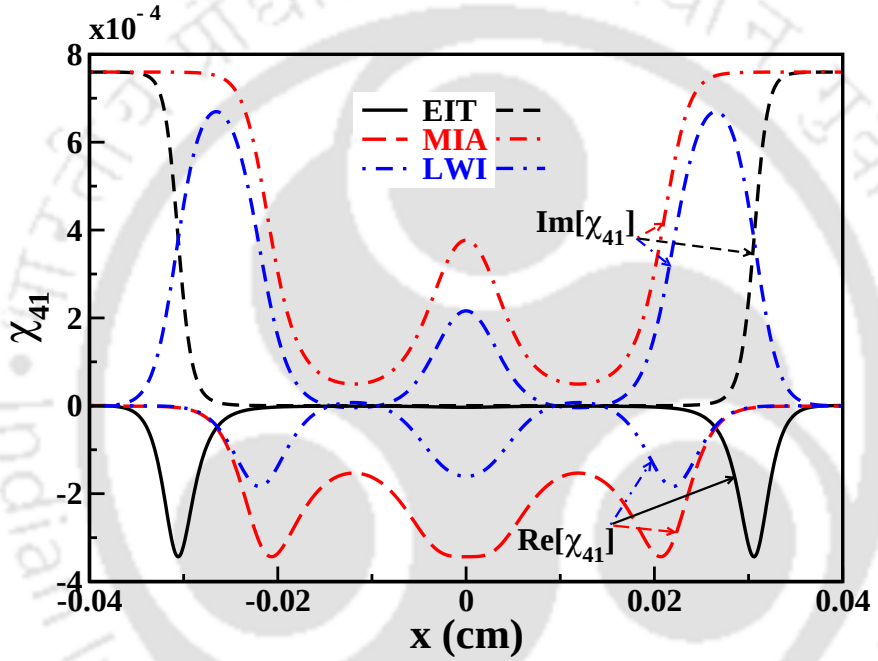

FIGURE 3.4: The Spatial variation of the real (Re[χ_{41}]) and imaginary (Im[χ_{41}]) parts of χ_{41}. The plots are shown against the transverse axis coordinate x of the control beam for $y = 0$ plane. The different curves are for three different set of parameters: $\Omega = 0.015\gamma$, $r = 0$, $\Delta_1 = 0.001\gamma$ (red long dashed, and dot-dashed lines); $\Omega = 0.015\gamma$, $r = 0.0005\gamma$, $\Delta_1 = 0.001\gamma$ (blue dashed double-dot, and dot double-dashed lines), and $\Omega = 0$, $r = 0$, $\Delta_1 = -0.001\gamma$ (black solid, and short dashed lines). The control beam parameters are $G_0 = 1\gamma$, $w_c = 100\,\mu$m, and $a_1 = -a_2 = 0.012$ cm.

The spatially modulated control field perturbs the probe beam susceptibility along the transverse direction as shown in Fig. 3.4. Fig. 3.4 illustrates the spatial variation of the real and imaginary parts of χ_{41} as a function of the transverse axis x for $y = 0$ plane. The very

special inhomogeneous character of dispersion Re[χ_{41}] and absorption Im[χ_{41}] causes the spatial modulation in phase and amplitude for the probe field, respectively. Since the phase of probe beam is influenced by the co-propagating control beam, therefore, this phase modulation is termed as cross phase modulation (XPM) [161]. The mutual coupling between the optical beams is attributed to XPM which causes focusing to the probe beam. The amplitude modulation results in attenuation or gain to the probe beam.

The curves of Fig. 3.4 represent three different cases of EIT, MIA, and LWI, respectively. It is clear from Fig. 3.4 that for MIA and LWI cases two transparency windows are formed at higher intensity regions whereas absorption occurs in relatively low intensity regions of control field G defined by two Gaussian modes using Eq. (3.35). The real part of the susceptibility is maximized at these higher intensity regions. This resembles two parallel waveguide like structures with claddings (0.0075 cm$\gtrsim |x| \gtrsim$ 0.0175 cm) and cores (0.0175 cm$\gtrsim |x| \gtrsim$ 0.0075 cm). In order to have a perfect wave-guiding, there should be a high contrast between core and cladding. In case of EIT, it is evident from Fig. 3.4 that a single transparency window is formed and the variation in refractive index around $x = 0$ is very small. Therefore, the single transparency window is failed to create two parallel waveguides. As a result, EIT is not suitable to separate out the modes with high resolution. However, in the case of MIA, one can see a sharp variation in refractive index (red long dashed line) around $x = 0$, with a rapid increase in contrast from core to cladding. But there is reasonable increase in absorption in the region between 0.0175 cm$\gtrsim |x| \gtrsim$ 0.0075 cm of the doublet as compared to EIT. This increment will reduce transmission of the probe beam and therefore, its visibility seems to be restricted.

Interestingly, in case of LWI, the refractive index contrast between core and cladding is higher than the other two cases. This contrast enhancement causes strong focusing of the probe beam towards the center of the two peaks of the control field. As a result, the width of the probe beam becomes narrow which improves the contrast of the cloned image on the probe field. Also the two deeps of the doublet changes from absorption into gain and can produce the enhancement of the cloned beam transmission. Hence the weak probe beam is not only guided or focused but also amplified in order to preserve the information during the propagation through the optical medium. This is the key mechanism of cloning the un-resolvable or just-resolvable control field profile to the probe field with high resolution. In the following, we use the inhomogeneous susceptibility for LWI case to illustrate the improvement of the resolution of the cloned images of the control field onto the probe field.

3.2.3 Beam propagation dynamics

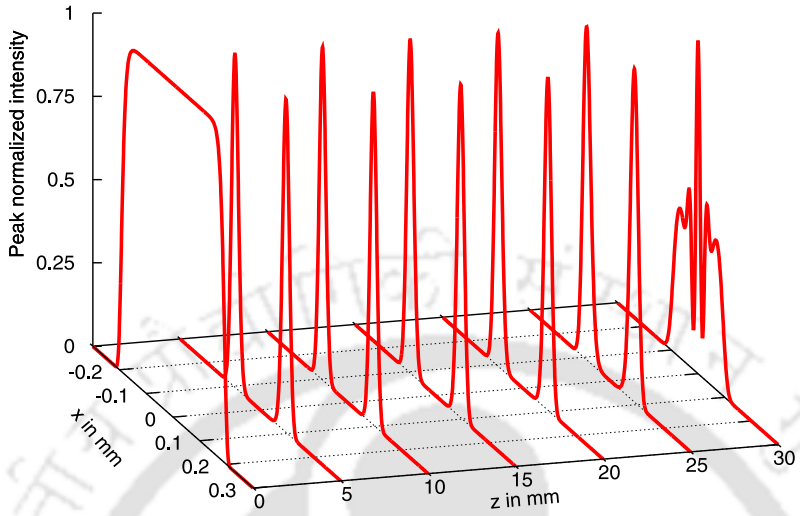

(a)

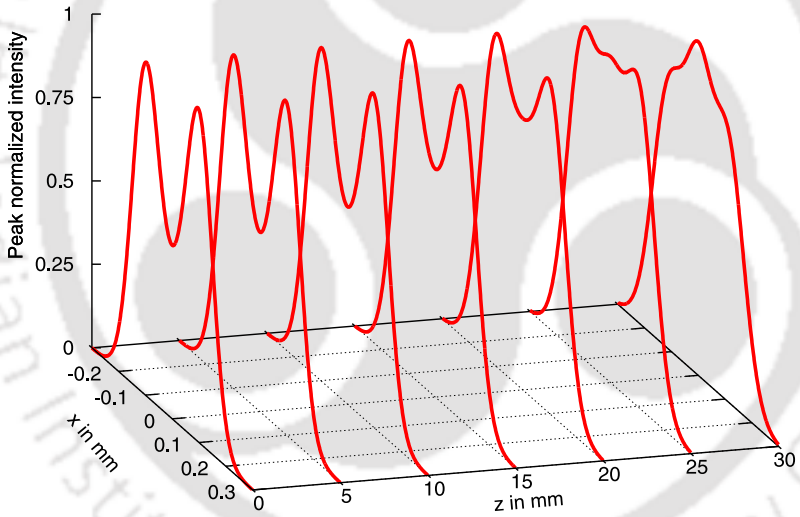

(b)

FIGURE 3.5: Spatial evolution of beam profiles. In panel (a), the spatial evolution of probe beam profile is shown against the transverse coordinate x for $y = 0$ plane at different propagation distances z. In panel (b), the peak-normalized intensity profile of the control beam is shown at different propagation distances z. The parameters are chosen as follows: $\Omega = 0.018\gamma$, $r = 0.00075\gamma$, $\Delta_1 = 0.001\gamma$. The control beam (Rayleigh limited) parameters are same as in Fig. (3.3).

We numerically integrate the paraxial wave Eqs. (3.33) and (3.34) by using a higher order split operator method (Appendix A) to study the propagation dynamics of both control and probe beams. First, we explore the cloning of Rayleigh limited control beam onto the probe beam in presence of both microwave and incoherent pump fields. For this purpose, we set $w_c = 100\ \mu$m and $a_1 = -a_2 = 0.01$ cm in the Eq. (3.35). The results for the spatial evolution of the control and the probe profiles throughout the medium are shown in Fig. 3.5. It is clear from Fig. 3.5(a) that within a very short distance, the control field structure is mapped on to the probe with central minimum reduced to zero. As a result, the finesse, which is the ratio of the spacing between peaks to the width of peaks of the transmitted probe beam at $z = 2.5$ cm, is 4 times smaller than initial control beam finesse. The optically cloned probe image at $z = 2.5$ cm is well matched with the control field envelope expression (3.35) for the parameters $w_c = 29\ \mu$m and $a1 = -a2 = 0.01$ cm.

We also find that the integrated transmission of the output probe beam at $z = 2.5$ cm is about 98%. The probe beam transmission can be changed by changing the incoherent pump field rate r. Fig. 3.5(b) depicts the intensity profile of the control beam at different propagation distances z. We find that the the shape of the control beam is gradually distorted as it propagates through the medium due to diffraction. As a consequence, control beam induced waveguide structure in the medium is modified. Accordingly the shape of the cloned beam starts experiencing diffraction after $z = 2.5$ cm propagation distance as shown in Fig. 3.5(a). Long distance diffractionless cloned image propagation can be achieved by considering tightly focused control beam [58] or self-reconstructing Bessel control beam [162].

Fig. 3.6 compares the cloning mechanism in presence and absence of both microwave and incoherent pump fields for the Rayleigh limited control field structure generated a double transparency window and a single transparency window for DDR and EIT system, respectively. It is clear from Fig. 3.6 that the double transparency windows enable to perfectly clone the control image with high resolution whereas single transparency window failed to clone the control image to the transmitted probe beam. We also notice that the DDR induced waveguide structure can support the propagation of cloned probe beam without any diffraction. In contrast, for EIT case, the transmitted probe beam suffers severe distortion due to lack of parallel waveguide like structure inside the medium. Hence EIT based mechanism has limitation to clone unresolved or just resolved control image onto probe beam without loss of generality.

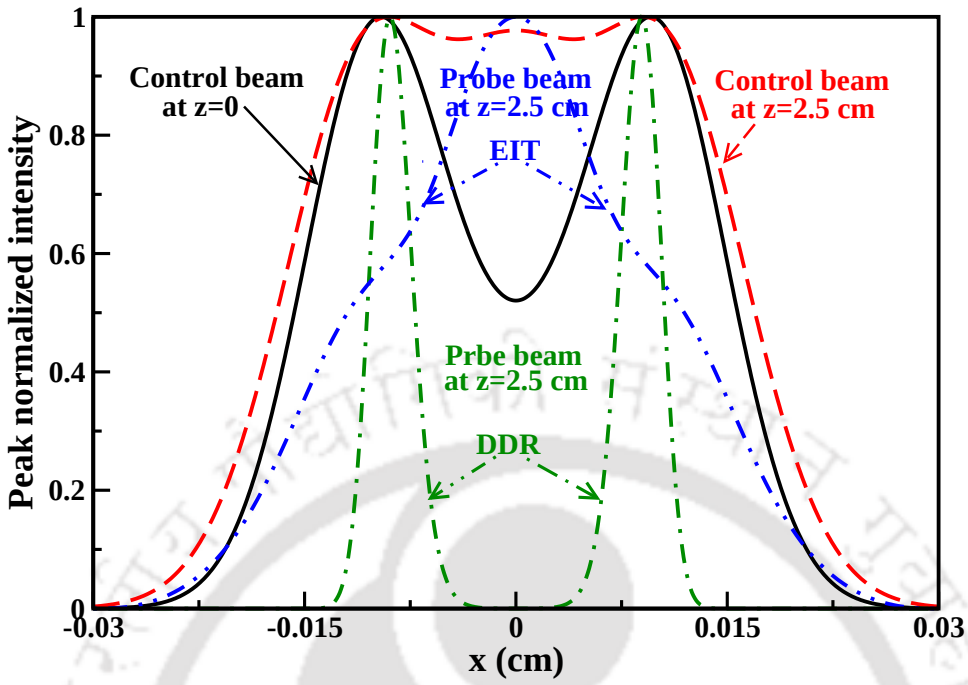

FIGURE 3.6: A comparison study of EIT and DDR with incoherent pump for cloning of the just resolved control images onto the probe beam at the output of the vapor cell with length $L = 2.5$ cm. The parameters are same as in Fig. 3.4

Next, we demonstrate how the microwave and incoherent pump fields offer the unprecedented control over the image cloning for unresolved images. For this purpose, we consider more complex structure of control beam consisting of three Gaussian peaks. Fig. 3.7 shows the radial distribution of the input Sparrow limited control beam (at z = 0) and output probe beam at z = 1 cm. As in Fig. 3.7(b) it can be seen that the cloned probe images contains three distinguishable peaks even though the control beam profile is unresolved. Surprisingly, the integrated transmission intensity of the cloned probe image is approximately 74%. Thus microwave and incoherent pump fields allow one to cloned the diffraction limited control field image onto the probe beam with improved spatial resolution and high transmission. We also verified that the resolution enhancement of cloned images can be possible even for Rayleigh limited control images with the Bessel as well as non-Gaussian shape. These studies may be useful for practical applicability such as optical microscope, quantum metrology and quantum imaging [163].

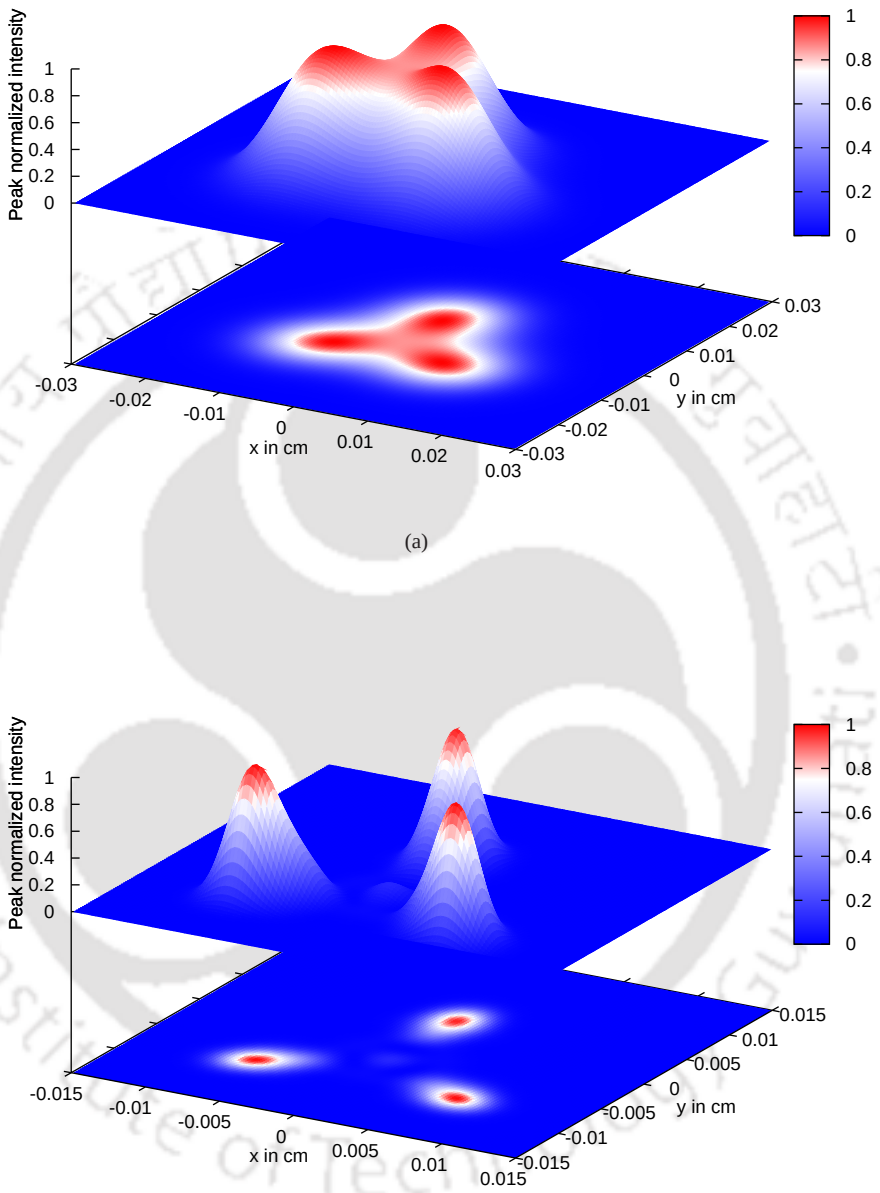

FIGURE 3.7: Picture (a) shows 3-D intensity profile of the input control beam. Picture (b) shows the transmitted probe beam at the output of a 1 cm long medium. The parameters are as in Fig. 3.5 except location of the three peaks are $(-0.009, -0.009)$, $(0.009, -0.009)$, $(0.0, 0.0066)$cm, and $\Omega = 0.02\gamma$, $r = 0.00073\gamma$.

3.2.4 Spatial optical switching

Here, we show how the propagation dynamics of the probe beam can be controlled by switching the microwave field on and off. The well resolved control beam image is being considered for this demonstration. The individual peak has width 100μm which corresponds to 4 cm Rayleigh length. The spatially dependent control field assisted atomic waveguide can protect the feature of the cloned beam in a 4 cm long medium.

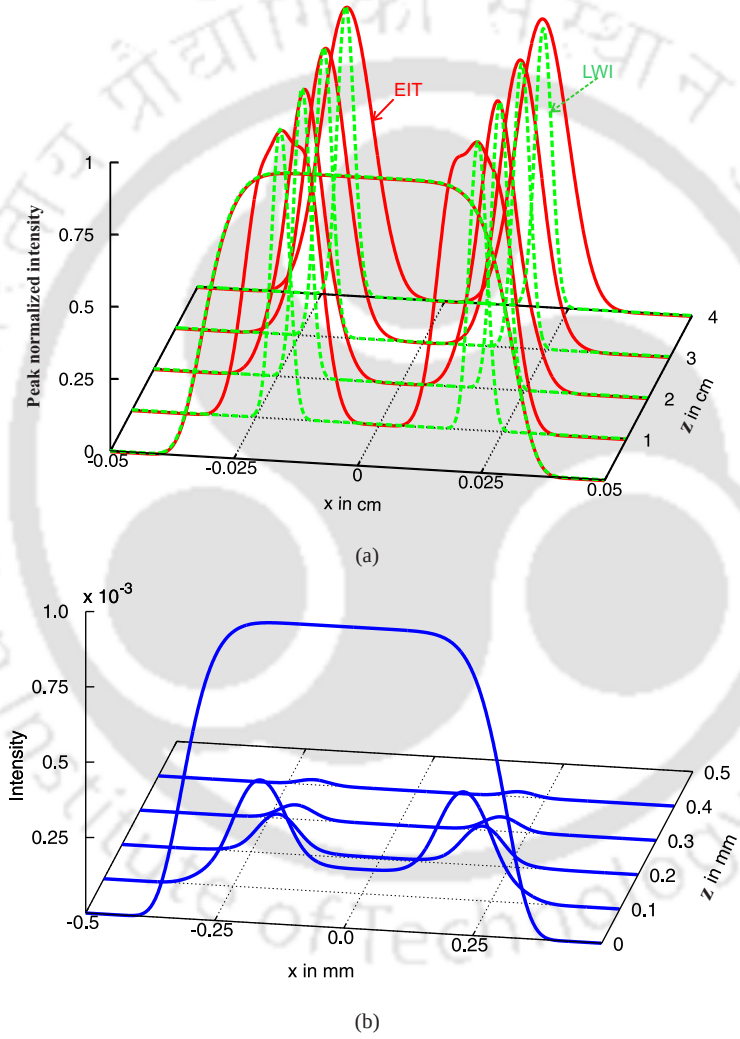

FIGURE 3.8: The intensity profile of the probe field transmission is shown against transverse axis x with $y = 0$ at different propagation distances z. Parameters used: (a) EIT case ($\Omega = 0, r = 0, \Delta_1 = -0.005\gamma$), LWI case ($\Omega = 0.01\gamma, r = 0.0001\gamma, \Delta_1 = 0.0001\gamma$), and (b) MIA case ($\Omega = 0.01\gamma, r = 0, \Delta_1 = 0.0001\gamma$).

Fig. 3.8(a) illustrates that the nondiffracting cloned probe beam propagation is possible inside the medium in both EIT as well as LWI system. Top panel shows probe beam is turned on in both EIT and LWI cases. The lower panel shows probe beam is turned off in MIA situation. The initial profile of the control field contains two well resolved Gaussian peaks with location $a_1 = -a_2 = 0.02$ cm as in Eq. (3.35). We found that the width and the transmission of the cloned beam at $z = 3$ cm are 25 μm (100 μm) and 60% (5%) for LWI (EIT) mechanism. Therefore, the precise control of finesse and the contrast of the output cloned probe beam can be achieved by application of coherent fields and incoherent pump field interacting in a four level atomic medium. Fig. 3.8(b) shows how the microwave induced absorption can be utilized to attenuate the probe beam gradually inside the medium in the absence of incoherent pump field. Thus, microwave field which connects the lower level metastable states of four level system can switch off the probe beam propagation inside the medium. This investigation can be applicable for all optical switching and logic gates [160, 164].

3.3 Chapter conclusion

In conclusion, we have revealed a scheme to improve the resolution of the cloned image based on the quantum interference effects induced by interacting dark resonances. For this purpose, we have used four levels atomic system interacting with three coherent fields and an incoherent pump field. An atomic wave-guide structure is formed inside the medium by using a spatially modulated control field. The refractive-index contrast between core and cladding of the atomic waveguide can be increased by use of sharp absorption peak associated with double dark resonances. The high contrast atomic wave-guide enables us to imprint the Rayleigh or Sparrow limited control images to probe field with high resolution. The transverse feature of control image is efficiently cast on to the probe field even though the control image suffers distortion due to the diffraction during the propagation. Our numerical result show that the propagation of high resolution cloned image is possible until the feature of the control image lost completely. We use incoherent pump field in order to increase the transmission of the cloned probe image. Finally, we have also demonstrated that spatial optical switching is possible by use of EIT, LWI and MIA mechanism. Moreover, incoherent pumping reduces the

unwanted attenuation or may result in amplification of the light in medium but it simultaneously destroys the atomic coherence. Incoherent pumping is an incoherent process causes a lasing without population inversion by transferring the populations from one level to another through spontaneous emission. Thus, the benefits of gain or suppression of absorption due to incoherent pump pays the price of dephasing of the coherences. The decrease in atomic coherence by increasing incoherent pumping results in undesirable continuous decrease in slope of dispersion curve. In contrast, the active Raman gain process is completely coherent process have the advantage to give desirable gain and wide tunability without disturbing the coherences. In a Raman gain medium, lifetime of atomic coherence is comparatively longer compared to incoherent processes. Therefore, by introducing Raman gain system, we exploit the possibility to overcome the limitations through incoherent pumping.

Chapter 4

Optical beam steering, splitting, and cloning in Raman gain medium

Optical beam guiding, deflection and cloning has attracted a great deal of attention due to its tremendous applications in optical imaging, optical switching, optical lithography, laser machining, and free-space communication technologies. The guiding and steering of an optical beam is made possible by virtue of a refractive index of the medium. Several techniques such as mechanical [165, 166], thermal [167], electrical [168], acousto-optical [169] and all optical [170–173] have been proposed to control the refractive index for beam deflection. However, all-optical methods have been paid much effort owing to many striking features such as high speed, efficiency, and quick nonlinear response time.

The nonlinear optical interactions between light and matter creates a new avenue to control over beam propagation dynamics through a medium. This is feasible as the absorptive and dispersive properties of the medium can be modified by the strength of the interactions. Such manipulation of dispersion and absorption leads to many novel phenomena including electromagnetically induced transparency (EIT). Most of the EIT-based schemes for producing beam deflection and guiding have low transmission due to presence of medium absorption [52, 53, 174]. Therefore, finding an alternative medium which displays gain with the desired variation of refractive index is a challenging task. In this context, active Raman gain (ARG) media have attracted a lot of attention [37]. Recently Zhu *et al.* [175] have theoretically studied the beam deflection in an ARG medium. They have used spatially inhomogeneous pump beam to deflect a weak probe beam. They have found that the deflection

angle is increased by an order of magnitude as compared to EIT medium. Nonetheless the probe field experiences a large amount of gain during the propagation through a Λ-type ARG medium [37, 175]. This large gain makes the probe beam propagation unstable and thus limits the practical application [176, 177]. Moreover, the input spot sizes for individual Gaussian profiles of pump and probe beams are equal to 1.4 cm and 1 mm, respectively. Hence, the diffraction spreading of such beams are not relevant since Rayleigh length is much larger than the length of the medium. Focusing laser beams into smaller spots and increasing the spatial resolution of arbitrary images is a fundamental problem in all-optical image processing [178, 179]. Distortion and absorption holds the fundamental limitation for the creation, detection, or propagation of small images. This limitation affects the applications such as efficient transfer and conversion of small images [153, 180, 181], steering [54, 182] or optical manipulation of light beams [183]. Here we address these issues by considering the propagation of diffraction-limited beams and arbitrary images through a controllable ARG medium.

In this chapter, we exploit an antiwaveguide mechanism [184] to show beam steering, splitting, and cloning of an arbitrary images in an inhomogeneously broadened medium. To facilitate these processes, we use spatial inhomogeneous pump beam to write an antiwaveguide inside the medium for copropagating probe beam. At two-photon Raman detuning condition, the refractive index and gain of the probe susceptibility are high at the peak of the Gaussian pump beam whereas at wings both are very small. The high refractive index together with gain allow to deflect the probe beam when it is launched at the wings of the pump beam. The control field parameters such as detuning and intensity can be used to control the transmission intensity and width of the deflected probe beam. Next, we reveal splitting of a single super-Gaussian probe beam into two Gaussian beams by use of two-peak pump beam structure. The bright and dark regions of the pump field profile induces a high (cladding) and low (core) refractive index of the probe field which lead to formation of an antiwaveguide structures inside the medium. More specifically, the super-Gaussian probe beam guided out from the core where it was injected. The diffraction-limited probe beam gets focus in the cladding due to the converging refractive index. We also observe that the transmitted probe beam gets the shape of the pump beam with finesse two times larger than the initial finesse of the pump beam. Further, we demonstrate the cloning of a doughnut-shaped pump beam structure onto the probe beam. Our numerical simulation shows that the cloned probe has a controllable gain with high resolution. Furthermore, our scheme can be employed for cloning the arbitrary pump images to the probe beam even though the pump images is severely distorted due to

diffraction. It follows that our findings can greatly improve the device performance on beam steering, splitting and image cloning beyond the diffraction limit.

4.1 Physical Model and Basic Equations

The schematic of the system under consideration for the generation of steering, splitting and cloning of an optical beam is illustrated in Fig. 4.1(a) where three co-propagating fields interact within the inhomogeneously broadened medium. The electrical dipole allowed transitions $|1\rangle \leftrightarrow |3\rangle$, $|3\rangle \leftrightarrow |2\rangle$, and $|2\rangle \leftrightarrow |4\rangle$ form a four-level N-type atomic system as shown in Fig. 4.1(b). The transitions $|1\rangle \leftrightarrow |2\rangle$, $|3\rangle \leftrightarrow |4\rangle$ and $|1\rangle \leftrightarrow |4\rangle$ are generally forbidden electric dipole transitions. The atomic transitions $|3\rangle \leftrightarrow |1\rangle$, $|3\rangle \leftrightarrow |2\rangle$, and $|4\rangle \leftrightarrow |2\rangle$ are driven by a pump field with frequency ω_1, a weak probe field with frequency ω_2 and a control field with frequency ω_3, respectively. This generic level configuration can be found for example in energy levels of ^{87}Rb which contain ground levels $|1\rangle = |5S_{1/2}, F = 2\rangle$, $|2\rangle = |5S_{1/2}, F = 3\rangle$ and excited levels $|3\rangle = |5P_{1/2}, F' = 2\rangle$ and $|4\rangle = |5P_{3/2}, F' = 4\rangle$, respectively [185, 186].

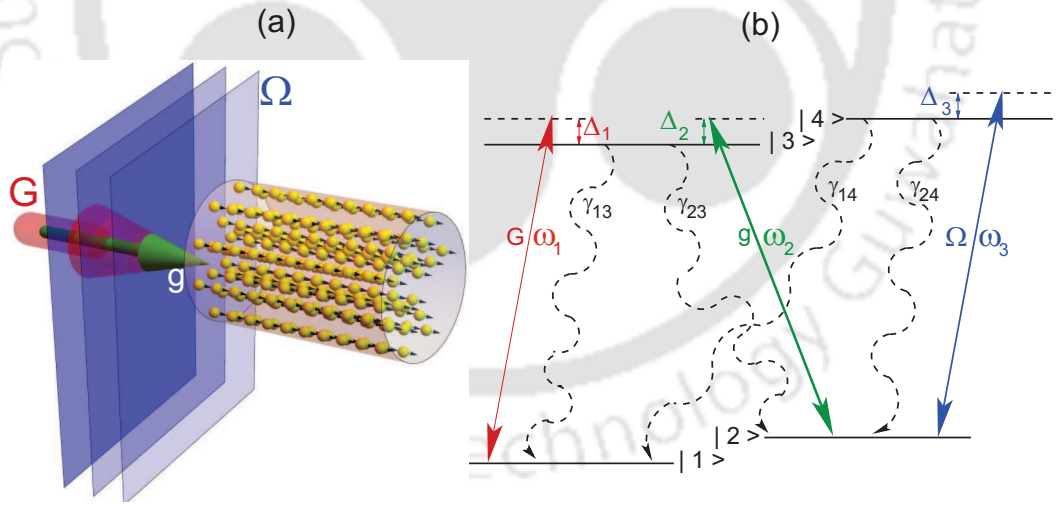

FIGURE 4.1: (a) Schematic illustration to produce steering, splitting and cloning of the optical beam. The beam shaped pump, probe and a plane wave control fields are co-propagating with the thermal ^{87}Rb atoms. (b)Energy-level diagram of a four-level ^{87}Rb atomic system in N configuration. The atomic transition $|3\rangle \leftrightarrow |1\rangle$ is coupled by a pump field of Rabi frequency G. The weak probe field of Rabi frequency g interacts with the atomic transition $|3\rangle \leftrightarrow |2\rangle$. A control field of Rabi frequency Ω connects the transition $|4\rangle \leftrightarrow |2\rangle$ to produce controllable gain of the system.

We define three co-propagating electric fields as follows:

$$\mathbf{E}_j(\mathbf{r},t) = \hat{\mathbf{e}}_j \mathcal{E}_j(\mathbf{r})\, e^{-i(\omega_j t - k_j z)} + \text{c.c.}, \tag{4.1}$$

where, $\mathcal{E}_j(\mathbf{r})$ are slowing varying envelopes, $\hat{\mathbf{e}}_j$ is the unit polarization vector, and k_j is the wave number of electric fields. The index $j \in \{1,2,3\}$ denotes the pump, probe, and control fields, respectively. Under the action of three coherent fields, the interaction Hamiltonian of the system in the dipole and rotating wave approximation is given by

$$\begin{aligned}\mathcal{H}_I/\hbar = {} & (\Delta_2 - \Delta_1 - \Delta_3)|4\rangle\langle 4| + (\Delta_2 - \Delta_1)|2\rangle\langle 2| \\ & - \Delta_1|3\rangle\langle 3| - (g|3\rangle\langle 2| + G\,|3\rangle\langle 1| + \Omega\,|4\rangle\langle 2| + \text{H.c.})\,,\end{aligned} \tag{4.2}$$

where $\Delta_1 = \omega_1 - \omega_{31}$, $\Delta_2 = \omega_2 - \omega_{32}$, $\Delta_3 = \omega_3 - \omega_{42}$ are the single-photon detunings of the pump, probe, and control fields, respectively. The atomic transition frequencies are denoted by ω_{ij}. The Rabi frequencies of pump, probe and control fields are defined as

$$G = \frac{\mathbf{d}_{13}\cdot\hat{\mathbf{e}}_1\mathcal{E}_1}{\hbar},\quad g = \frac{\mathbf{d}_{23}\cdot\hat{\mathbf{e}}_2\mathcal{E}_2}{\hbar},\ \text{and}\ \ \Omega = \frac{\mathbf{d}_{24}\cdot\hat{\mathbf{e}}_3\mathcal{E}_3}{\hbar}\,, \tag{4.3}$$

where the d_{ij} are the corresponding dipole moment matrix elements of transitions $|i\rangle \leftrightarrow |j\rangle$.

The dynamical evolution of the atomic system can be described by the Liouville equation:

$$\dot{\rho} = -\frac{i}{\hbar}[\mathcal{H}_I, \rho] + \mathcal{L}\rho\,, \tag{4.4}$$

where the Liouvillian matrix $\mathcal{L}\rho$ describes the relaxation by radiative and non-radiative decay and is defined by

$$\mathcal{L}\rho = \begin{bmatrix} \gamma_{13}\rho_{33} + \gamma_{14}\rho_{44} & -\gamma_c\rho_{12} & -\Gamma_{13}\rho_{13} & -\Gamma_{14}\rho_{14} \\ -\gamma_c\rho_{21} & \gamma_{23}\rho_{33} + \gamma_{24}\rho_{44} & -\Gamma_{23}\rho_{23} & -\Gamma_{24}\rho_{24} \\ -\Gamma_{31}\rho_{31} & -\Gamma_{32}\rho_{32} & -(\gamma_{13}+\gamma_{23})\rho_{33} & -\Gamma_{34}\rho_{34} \\ -\Gamma_{41}\rho_{41} & -\Gamma_{42}\rho_{42} & -\Gamma_{43}\rho_{43} & -(\gamma_{14}+\gamma_{24})\rho_{44} \end{bmatrix}. \tag{4.5}$$

The radiative decay rates from the excited states $|3\rangle$ and $|4\rangle$ to ground states $|1\rangle$ and $|2\rangle$ are labeled by γ_{i3} and γ_{i4}, $i \in \{1,2\}$ and the collisions dephasing rate γ_c describes redistribution of

populations between ground levels. The decay rate of the atomic coherence is defined as

$$\Gamma_{\alpha\beta} = \frac{1}{2}\left[\sum_i \gamma_{i\alpha} + \sum_i \gamma_{i\beta}\right] + \gamma_c,\ i \notin \{\alpha,\beta\}\,. \tag{4.6}$$

Substituting the interaction Hamiltonian of Eq. (4.2) and the Liouvillian matrix of Eq. (4.5) in the density matrix Eq. (4.4), the equations of motion for the four-level atomic system can be described as

$$\dot{\rho}_{11} = \gamma_{13}\rho_{33} + \gamma_{14}\rho_{44} + iG^*\rho_{31} - iG\rho_{13}\,, \tag{4.7}$$

$$\dot{\rho}_{22} = \gamma_{23}\rho_{33} + \gamma_{24}\rho_{44} + ig^*\rho_{32} - ig\rho_{23} + i\Omega^*\rho_{42} - i\Omega\rho_{24}\,, \tag{4.8}$$

$$\dot{\rho}_{21} = -\left[\gamma_c - i\Delta_R\right]\rho_{21} - iG\rho_{23} + ig^*\rho_{31} + i\Omega^*\rho_{41}\,, \tag{4.9}$$

$$\dot{\rho}_{33} = -(\gamma_{13} + \gamma_{23})\rho_{33} + iG\rho_{13} - iG^*\rho_{31} + ig\rho_{23} - ig^*\rho_{32}\,, \tag{4.10}$$

$$\dot{\rho}_{31} = -\left[\Gamma_{31} - i\Delta_1\right]\rho_{31} + ig\rho_{21} + iG(\rho_{11} - \rho_{33})\,, \tag{4.11}$$

$$\dot{\rho}_{32} = -\left[\Gamma_{32} - i\Delta_2\right]\rho_{32} + iG\rho_{12} - i\Omega\rho_{34} + ig(\rho_{22} - \rho_{33})\,, \tag{4.12}$$

$$\dot{\rho}_{34} = -\left[\Gamma_{34} - i(\Delta_2 - \Delta_3)\right]\rho_{34} + iG\rho_{14} + ig\rho_{24} - i\Omega^*\rho_{32}\,, \tag{4.13}$$

$$\dot{\rho}_{41} = -\left[\Gamma_{41} - i(\Delta_R + \Delta_3)\right]\rho_{41} + i\Omega\rho_{21} - iG\rho_{43}\,, \tag{4.14}$$

$$\dot{\rho}_{42} = -\left[\Gamma_{42} - i\Delta_3\right]\rho_{42} + i\Omega(\rho_{22} - \rho_{44}) - ig\rho_{43}\,, \tag{4.15}$$

together with population conservation condition $\rho_{11}+\rho_{22}+\rho_{33}+\rho_{44} = 1$ and two photon Raman detuning $\Delta_R = \Delta_1 - \Delta_2$. In the next section, we obtain the analytical expression for the linear susceptibility of the probe field in a compact form with assumption of equal decay rates from excited states, *i.e.*, $\gamma_{13} = \gamma_{23} = \gamma_{14} = \gamma_{24} = \gamma/2$.

4.2 Probe Susceptibility for hot atomic medium

In this section, we derive an approximate solution of linear susceptibility of the probe field in a hot atomic medium. The analytical solution of the atomic coherence ρ_{32} for the probe field can be obtained by solving the density matrix Eqs. (4.7)-(4.15) in the steady state condition.

We assume that the atoms are prepared initially in the ground state $|1\rangle$. Due to the presence of large detuning of the strong pump and weak probe fields, most of the atoms populate at their ground state $|1\rangle$ while other states $|j\rangle (j \neq 1)$, remain empty at later time. Hence the system

turns to an ARG configuration for the probe field. Since Raman gain process is basically a second-order process, we therefore expand the density matrix elements to first order in the probe field g and to second order in the pump field G but all orders in the control field Ω in the weak probe field limit. The perturbation expansion of the density matrix can be expressed as

$$\begin{aligned}\rho_{ij} &= \rho_{ij}^{(0)} + G\rho_{ij}^{(1)} + G^*\rho_{ij}^{(2)} + g\rho_{ij}^{(3)} + g^*\rho_{ij}^{(4)} + G^2\rho_{ij}^{(5)} \\ &+ |G|^2\rho_{ij}^{(6)} + G^{*2}\rho_{ij}^{(7)} + gG\rho_{ij}^{(8)} + gG^*\rho_{ij}^{(9)} \\ &+ g^*G\rho_{ij}^{(10)} + g^*G^*\rho_{ij}^{(11)} + g|G|^2\rho_{ij}^{(12)},\end{aligned} \tag{4.16}$$

where, $\rho_{ij}^{(0)}$ describes the solution in the absence of all three optical fields and $\rho_{ij}^{(k)}$ denotes the k-th order solution. Now we substitute the above expression in the Eqs. (4.7)-(4.15) and equate the coefficients of g, g^*, G^n ($n \in 1, 2$), and constant terms. As a result, we obtain a set of 12 coupled simultaneous linear algebraic equations to determine the expression of $\rho_{32}^{(12)}$. We use back substitution method to solve these algebraic equations in order to derive the probe coherence ρ_{32}. The different terms related to 12th-order contributions are given by

$$\rho_{32}^{(12)} = \frac{i(\rho_{22}^{(6)} - \rho_{33}^{(6)}) + i\rho_{12}^{(9)} - i\Omega\rho_{34}^{(12)}}{[\gamma_{32} - i\Delta_2]}, \tag{4.17}$$

$$\rho_{34}^{(12)} = \frac{i\rho_{14}^{(9)} + i\rho_{24}^{(6)} - i\Omega^*\rho_{32}^{(12)}}{[\Gamma_{34} - i(\Delta_2 - \Delta_3)]}, \tag{4.18}$$

$$\rho_{12}^{(9)} = \frac{i\rho_{32}^{(3)} - i\rho_{13}^{(2)} - i\Omega\rho_{14}^{(9)}}{[\gamma_c + i\Delta_R]}, \tag{4.19}$$

$$\rho_{14}^{(9)} = \frac{i\rho_{34}^{(1)} - i\Omega^*\rho_{12}^{(9)}}{[\Gamma_{41} + i(\Delta_R + \Delta_3)]}, \tag{4.20}$$

$$\rho_{33}^{(6)} = \frac{i(\rho_{13}^{(2)} - \rho_{31}^{(1)})}{[\gamma_{13} + \gamma_{23}]}, \tag{4.21}$$

$$\rho_{24}^{(6)} = \rho_{44}^{(6)} = \rho_{22}^{(6)} = 0, \tag{4.22}$$

$$\rho_{13}^{(2)} = \rho_{31}^{(1)} = \frac{-i}{[\Gamma_{13} + i\Delta_1]}, \tag{4.23}$$

$$\rho_{32}^{(3)} = \rho_{34}^{(1)} = 0. \tag{4.24}$$

$$\rho_{32} = A\left[\frac{2\Gamma_{31}[\Gamma_{34} - i(\Delta_2 - \Delta_3)]}{(\gamma_{13} + \gamma_{23})(\Gamma_{31}^2 + \Delta_1^2)} + \frac{[\Gamma_{34} - i(\Delta_2 - \Delta_3)][\Gamma_{41} + i(\Delta_R + \Delta_3)] - |\Omega|^2}{(\Gamma_{31} + i\Delta_1)[(\gamma_c + i\Delta_R)\{\Gamma_{41} + i(\Delta_R + \Delta_3)\} + |\Omega|^2]}\right] \tag{4.25}$$

with

$$A = \frac{-ig|G|^2}{(\gamma_{32} - i\Delta_2)\{\gamma_{34} - i(\Delta_2 - \Delta_3)\} + |\Omega|^2}\,. \tag{4.26}$$

The atomic coherence ρ_{32} will yield the probe susceptibility χ at frequency ω_2

$$\chi(\Delta_2) = \frac{\mathcal{N}|d_{32}|^2}{\hbar}\rho_{32}\,, \tag{4.27}$$

where $\mathcal{N}$ is the atomic density of the medium. The above analysis is valid for stationary atoms. While for a hot atomic system, the thermal motion of the atoms causes inhomogeneous broadening of the atomic spectra. The thermal velocity v of the atom can be included in the susceptibility expression (4.27) by introducing velocity-dependent field detunings $\Delta_j(v) = \Delta_j - k_j v,\ j \in \{1, 2, 3\}$. The term $k_j v$ is the Doppler shift experienced by an atom with a velocity component v in the direction of the beam propagation of the fields. We have assumed the wave vectors of the three fields are nearly equal ($k_j \approx k$). The negative sign in the velocity-dependent field detuning $\Delta_j(v)$ indicate that atom and field are co-propagating. The susceptibility of a hot atomic vapour system needs to be averaged over the entire velocity distribution of atoms and it is given by

$$\langle\chi\rangle = \int_{-\infty}^{\infty} \chi(kv)P(kv)d(kv)\,. \tag{4.28}$$

The velocity distribution of the atom is assumed to obey the Maxwell-Boltzmann distribution

$$P(kv)d(kv) = \frac{1}{\sqrt{2\pi\mathcal{D}^2}}\exp\left[-\frac{(kv)^2}{2\mathcal{D}^2}\right]d(kv)\,. \tag{4.29}$$

The Doppler width $\mathcal{D}$ at temperature T defined by

$$\mathcal{D} = \sqrt{\frac{k_B T\omega^2}{Mc^2}}\,, \tag{4.30}$$

where M is the atomic mass and k_B is the Boltzmann constant. Doppler broadening plays a crucial role to control the width of the absorption or gain window of the thermal media [112, 187–190]. The spectral features of window become narrower in a Doppler broadened medium as compared with the homogeneous medium. The steepness of the refractive index due to the narrowing of resonance window can be useful in many applications such as slow light,

storage of light and high resolution spectroscopy. Thus we include atomic velocity effect on the beam propagation dynamics through ARG medium by considering Doppler averaging in the susceptibility expression.

4.3 Beam propagation equations and beam profiles

The propagation of co-propagating pump and probe fields with amplitudes $\mathcal{E}_1$ and $\mathcal{E}_2$ along the z-direction are governed by Maxwell's wave equations. Under slowly varying envelope and paraxial wave approximations, the beam propagation equations for pump and probe field can be expressed in the following form

$$\frac{\partial G}{\partial z} = \frac{i}{2k_1}\left(\frac{\partial^2}{\partial x^2} + \frac{\partial^2}{\partial y^2}\right)G\,, \tag{4.31}$$

$$\frac{\partial g}{\partial z} = \frac{i}{2k_2}\left(\frac{\partial^2}{\partial x^2} + \frac{\partial^2}{\partial y^2}\right)g + 2i\pi k_1\langle\chi\rangle g\,. \tag{4.32}$$

The velocity-averaged susceptibility $\langle\chi\rangle$ is included only in the probe beam equation, whereas this effect is very negligible on the pump beam propagation under the weak probe field as been pointed in Chapter 1. The second partial derivatives in the transverse directions (x, y) represent a paraxial diffraction. The diffraction of beam or image is inevitable since its constituent plane wave components acquire different phases during its propagation. The spatially dependent refractive index of the fields can be used to suppress or even reverse due to diffraction. We use a suitable spatially dependent pump field to produce spatially dependent refractive index for the probe field. For this purpose, we choose the transverse spatial profile of the pump beam as a Laguerre-Gaussian with charge m, denoted by LGP_m. The profile of pump beam can be written as

$$\begin{aligned} G(x,y,z) =& G_0\frac{w_0}{w_z}\left(\frac{r\sqrt{2}}{w_z}\right)^m \exp\left[\frac{ikr^2}{2R_z} - \frac{r^2}{w_z^2}\right] \\ & \times \exp\left[-i(m+1)\tan^{-1}\left(\frac{z}{z_R}\right) + im\theta\right], \end{aligned} \tag{4.33}$$

where G_0 is an initial peak amplitude, m is the azimuthal index. The beam width is defined as $w_z = w_0\sqrt{1+(z/z_R)^2}$, where w_0 is the beam waist at $z = 0$, and $z_R = \pi w_0^2/\lambda$ is the Rayleigh length. The radial distance from the axis of the beam is given by $r = \sqrt{x^2+y^2}$. Note that for

the azimuthal index $m = 0$, the Laguerre-Gaussian pump (LGP_m) beam reduces to a Gaussian pump beam (GP_0).

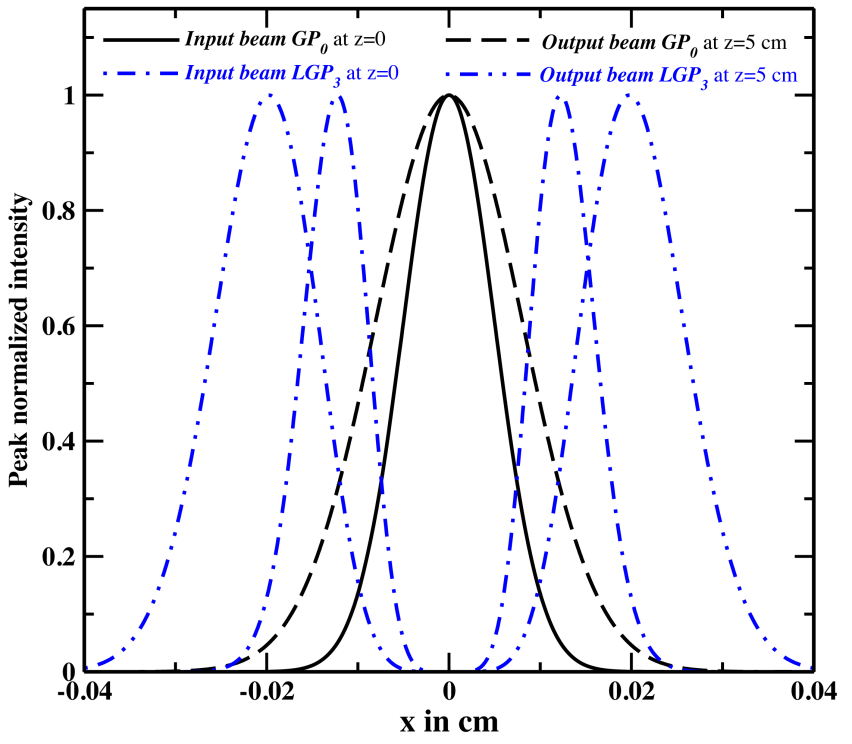

FIGURE 4.2: Pump intensities profile for two different shapes namely Gaussian (GP_0) and Laguerre-Gaussian (LGP_0) is plotted against x at $y = 0$ plane. The initial amplitude and width of profiles are $G_0 = 2\gamma$ and $w_0 = 100\ \mu$m, respectively.

Fig. 4.2 shows the intensity distribution of the pump field against radial position x at the different length of the medium. The LGP_m beam exhibits a dark spot in the centre and a bright profile in the annular region. This makes intensity profile in contrast to GP_0 beam. It is clearly shown in Fig. 4.2 that diffraction induced distortion of the pump beam profile is not severe even after 5 cm of propagation. Therefore, phase modulation imposed on the probe beam due to the spatially varying pump beam is effective throughout the length of the medium. The probe beam possesses a Gaussian profile as

$$g(x,y) = g_0 \exp\left[-\left(\frac{(x-a)^2 + y^2}{w_p^2}\right)^f\right], \tag{4.34}$$

at an entry face of the medium. The initial peak amplitude and the width of the probe field are denoted by g_0 and w_p and a is the initial location of the centre of the probe beam along the x direction. We have chosen the initial intensity of the probe beam such that it gets absorbed inside the medium without pump and control fields. The integer values of f decides the input profile of the probe beam: either a Gaussian ($f = 1$) or a super Gaussian ($f > 1$).

4.4 Results and Discussions

4.4.1 Spatial modulation of the probe field susceptibility

In order to elucidate the effect of position dependent characteristic of the pump field on the probe beam dynamics, we first numerically explore the behavior of velocity-averaged probe susceptibility under different detuning and intensity of the control field. Fig. 4.3 shows the spatial variation of probe dispersion and gain plotted against transverse axis x at $y = 0$ plane. Here two different transverse profiles of pump beam namely Gaussian (GP_0) and Laugerre-Gaussian (LGP_3) have been used.

We begin with Gaussian pump beam and study the usefulness of uniform control field Ω on the spatially modulated probe susceptibility. In absence of a control field, the position dependent refractive index of the probe is zero under two-photon Raman condition whereas the spatial gain profile of the probe field takes the shape of the pump beam profile (see black solid line in Fig. 4.3). The spatially dependent pump structure generates a probe gain profile which is one of the key components in realizing the deflection of the probe beam if it is off-centered with respect to the pump beam. In absence of the control field $\Omega = 0$, the gain profile of the probe field is 15 times larger than in case of control field $\Omega = \gamma$. This large gain can create modulation instability of system [176, 177]. Therefore a controllable gain of the medium is required to avoid the modulation instability.

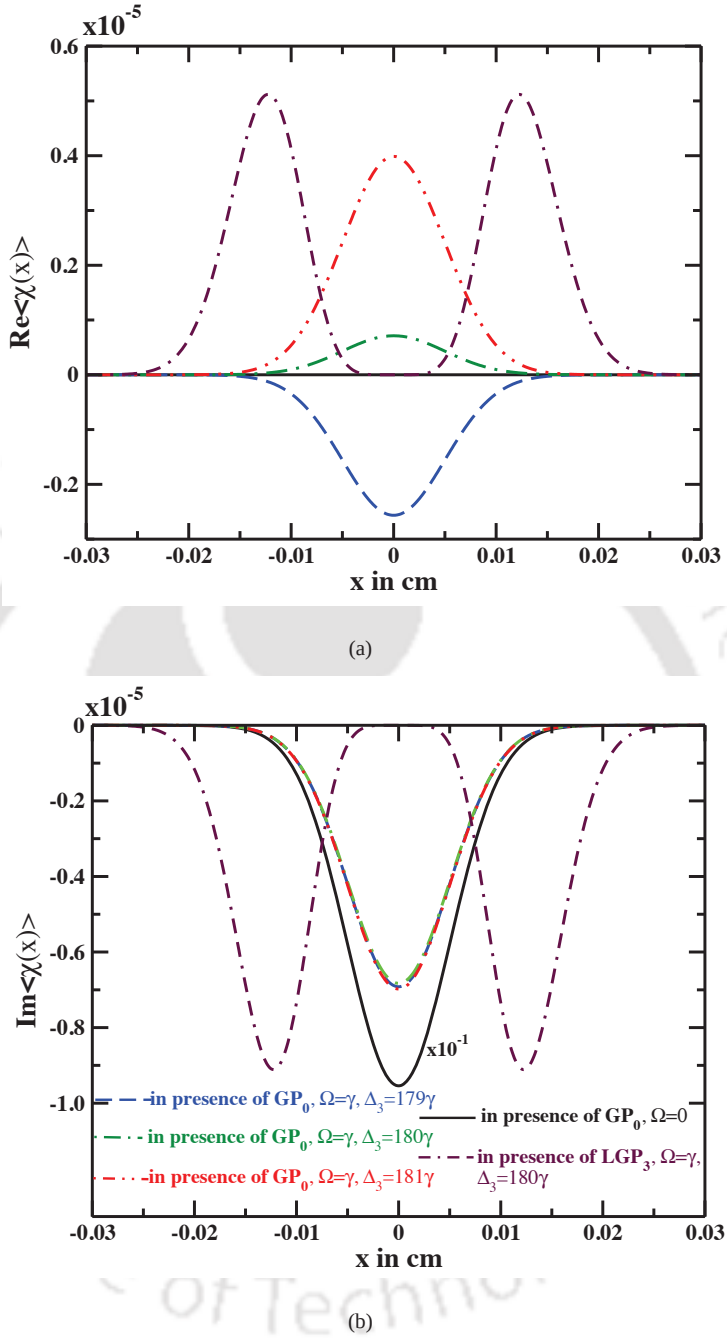

FIGURE 4.3: (a) Real and (b) imaginary part of the averaged susceptibility is plotted against the transverse co-ordinate x at $y = 0$ plane. The spatial probe gain profile (solid black line) is reduced by a factor of ten to visualise it with $\Omega(x, y) = \gamma$. The common parameters are fixed as follows: single photon detuning of pump and probe fields $\Delta_2 = \Delta_1 = 180\gamma$, Doppler width $\mathcal{D} = 140\gamma$, density $\mathcal{N} = 2.5 \times 10^{10}$ atoms/cm^3 and atomic coherence decay rate $\gamma_c = 0.01\gamma$. The other parameters are same as in Fig. 4.2.

It is clear from Fig. 4.3(b) that the position dependent probe gain can be substantially suppressed by a uniform control field with $\Omega(x,y) = \gamma$. This restricted probe gain is accompanied by a Gaussian shaped spatial refractive index. The gradient of the refractive index is dependent on the sign of the control field detuning. At red-shifted control field detuning, the slope of the spatial refractive index attains maximum at the line center and decreases gradually toward the wings. Hence, a convex lens like refractive index can be mimiced in the ARG medium for $\Delta_3 \geq \Delta_1$.

On the contrary the blue-shifted the control field detuning $\Delta_3 < \Delta_1$ can generate a concave refractive index profile onto the medium. Therefore the refractive index gradient allows us to focus or defocus the probe beam towards the center of the pump beam. As a result the probe field propagates through the gain window with narrowing or broadening, respectively. Hence a control field can prepare a gain medium with suitable spatial refractive index for encompass the probe beam deflection to a great extent.

Next we consider higher order LGP_3 mode to investigate the spatial inhomogeneous character of $\langle\chi\rangle$ in the presence of uniform control beam. The grey dot-dashed line in Fig. 4.3(a) and 4.3(b) shows the transverse variation of probe refractive index as well as gain, respectively. The position dependent refractive index and gain both increase in the bright region whereas it decreases at the dark region of the doughnut shaped pump beam. In other words, LGP_3 induces a diverging gradient index in the region $|r| \leq 0.005$ cm whereas a converging gradient index exists in regions 0.005 cm$\leq |r| \leq 0.02$ cm of the medium. Thus bright and dark regions of LGP_3 resembles a waveguide and anti waveguide structure inside the atomic medium. Fig. 4.3(a) is also show that the waveguide and anti-waveguide features are accompanied with gain and absorption, respectively. As a result, the probe beam is guided out from dark region and confined at bright region in the course of propagation inside the medium. Hence the shape of the pump beam profile can be efficiently transfered to the transmitted probe beam.

4.4.2 Numerical simulation of paraxial beams equations

We have simulated numerically the propagation Eqs. (4.31) and (4.32) for pump and probe beams by split step operator method (see Appendix A) to demonstrate the spatial susceptibility as well as diffraction effects on the beams propagation dynamics.

4.4.2.1 Optical beam steering

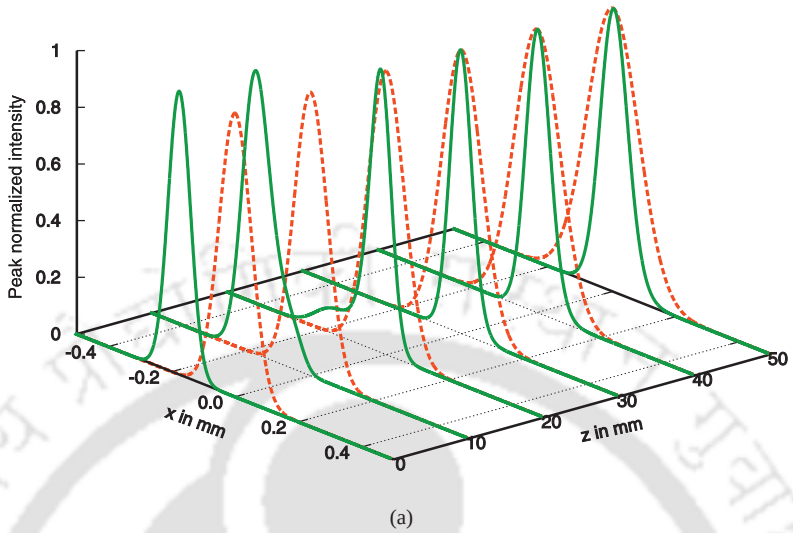

(a)

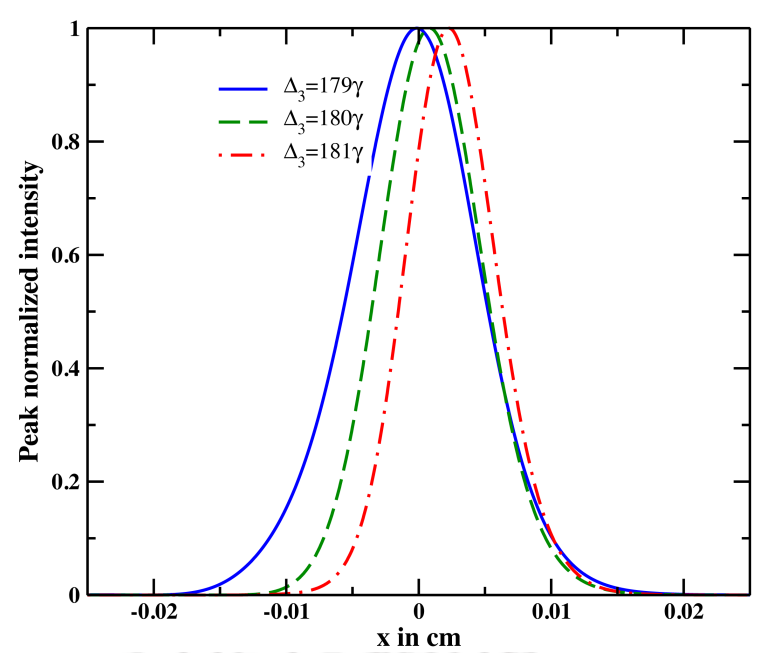

(b)

FIGURE 4.4: (a) The transverse probe beam intensity is plotted at different propagation distances within the medium. The initial amplitude, width and peak position of Gaussian probe beam are $g_0 = 10^{-3}\gamma$, $w_p = 70\ \mu$m and $a = 1.7$ mm, respectively. Single photon detuning of pump, probe and control fields are $\Delta_2 = \Delta_1 = \Delta_3 = 180\gamma$. (b) Transmitted probe beam width controlled by changing the detuning of control field at $z = 4$ cm under two photon Raman resonance condition $\Delta_2 = \Delta_1 = 180\gamma$. The other parameters are as in Fig. 4.3.

First, we study how the deflection of a probe beam can be controlled by a spatial dependence of the pump Rabi frequency. The shape and position of a probe beam is given by Eq. (4.34) at the entry face of the medium. Fig. 4.4(a) shows the spatial evolutions of the probe beam with $a = 1.7$ mm and $w_p = 70\ \mu$m when the peak of pump beam is centered at the origin $(0, 0)$ with $w_c = 100\ \mu$m. Initially the overlap area between the probe and pump beam is very negligible. The overlap area is gradually increased due to the broadening of both the beams during propagation. It is evident from this figure that after a propagation of one Rayleigh length, the probe beam progressively enters the pump region. The bright region of the pump beam tends to refract the probe beam into it and subsequently enhances the probe beam amplitude. As a result, the probe beam is focused towards the high intensity region of the pump and remains confined there. Ii is noteworthy that the probe beam gains the initial shape of the pump beam and retains this shape as it propagates along the z axis. Similarly, if the peak position of the probe beam is shifted along the positive x-direction then it can be dragged by the pump beam towards the pump line centre.

Fig. 4.4(b) exhibits the effect of control field detuning onto the propagation dynamics of a probe pulse at $z = 4$ cm. It is seen that the deflected probe beam becomes narrower at redshifted detuning as compared to a blue-shifted detuning. Therefore the sign of the detuning of the control field gives an additional flexibility to control the width of the deflected probe beam. Thus the ARG medium not only acts as an effective beam deflector but also can act like a lens with a wide focal length tunability.

4.4.2.2 Optical beam splitting

Next, we demonstrate the spatial evolution of single super-Gaussian probe as well as double Gaussian pump beam with different propagation distance z. At the entrance face of the medium, the probe beam is launched in the dark region of the double Gaussian pump beam as shown in Fig. 4.5. The position dependent pump beam creates two gain peaks together with converging refractive index in the probe susceptibility which is similar to the grey double dashed dotted line in Fig. 4.3. The gain and spatial inhomogeneity of the refractive index is accountable for this splitting of a single super-Gaussian probe beam into two Gaussian beams. The converging lens effect in the intense regions of the pump leads to focusing of the cloned probe beam towards it.

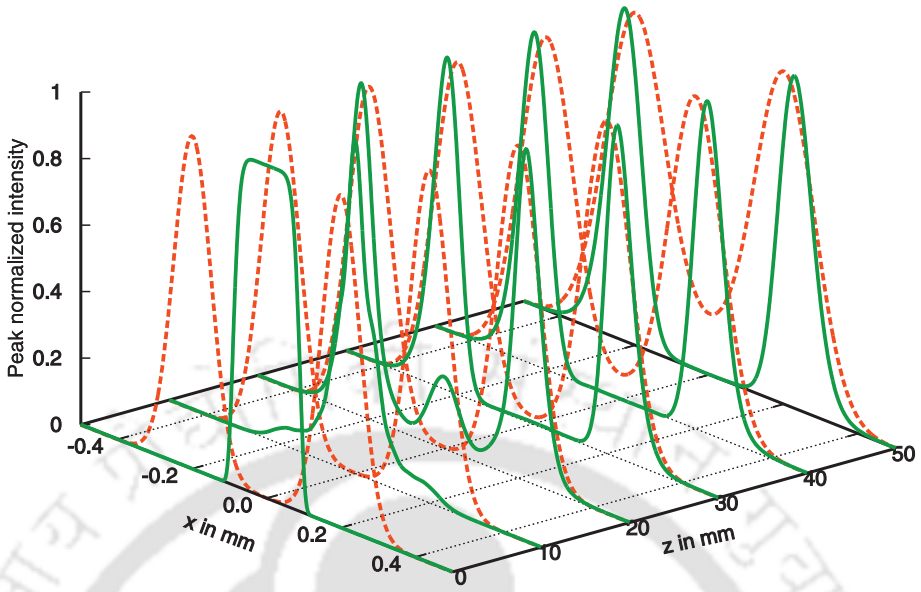

FIGURE 4.5: Propagation dynamics of single super Gaussian probe beam in presence of double Gaussian pump beam. The parameters are as in Fig. 4.4 except that the Gaussian probe beam is injected at centre $(0, 0)$ with width $w_p = 80$ μm and the double Gaussian pump beam has width 100 μm.

Therefore, the transmitted probe beam width is reduced by a factor of two as compared to the initial width of the pump beam and image become sharper as compared to original pump beam. It is also noticeable from Fig. 4.5 that the transmitted probe beam structure is preserved even though the pump beam suffers distortion due to diffraction.

4.4.2.3 Optical beam cloning

In this section, we investigate the efficient transfer of images between two co-propagating orthogonal polarized optical beams. We adopt all-optical anti-waveguide mechanism to clone the images from pump to probe beam. An all-optical anti-waveguide structure can be formed inside the medium with use of LGP_3 beam which has zero intensity at the beam center. The dark and bright regions of LGP_3 beam give rise to minimum and maximum refractive index gradient on the probe susceptibility. As a results a diverging and converging refractive index is formed in the core and cladding region of the antiwaveguide structure.

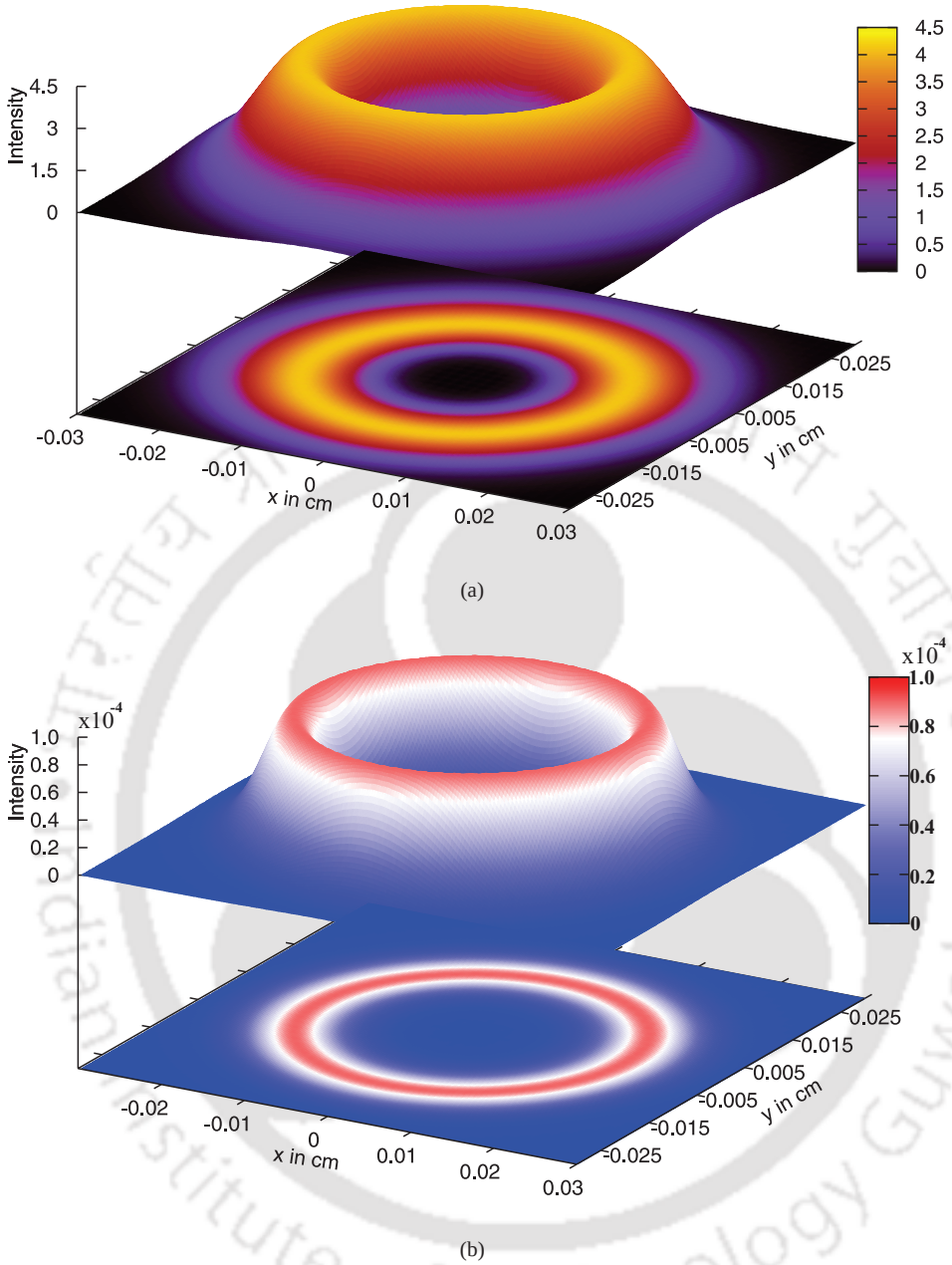

FIGURE 4.6: Image transfer from doughnut-shaped pump structure to the probe beam via anti-waveguiding mechanism. In (a), the 3D intensity profile of pump beam at the output of 5-cm-long medium. In (b), the cloned 3D probe intensity profile at the exit face of the rubidium vapour cell. The other parameters are same as in Fig. 4.4 except atomic density $\mathcal{N} = 2.5\times10^{11}$ atoms/cm^3 and ground state atomic coherence decay rate $\gamma_c = 0.001\gamma$, $G_0 = 2.5\gamma$ and $\Omega = 5\gamma$.

Thus an all-optical anti-waveguide for a probe beam is generated by the copropagating doughnut-shaped strong pump beam. In order to demonstrate the cloning mechanism in ARG medium, we take center of the dark region of the doughnut pump beam as initial location of probe beam. The diverging refractive index gradient and diffraction leads to the probe beam leaving the core region and slowly enter the high intensity regions of the pump beam. Therefore each wing of the probe beam profile experiences gain and converging gradient of refractive index in the cladding region. Thus the probe energy is guided into the annular ring of the doughnut-shaped beam and leaving a zero intensity in the dark region. Hence the transmitted probe beam profile acquires a doughnut-shaped profile as shown in Fig. 4.6(b). We have found that the transmitted structure of probe beam is twice as sharp compared to the LGP_3 beam structure. The transmitted pump beam profile is distorted severely at the output of the medium as shown in Fig. 4.6(a). The spatial evolution of probe beam at different propagation distances are similar to that in Fig. 4.5.

4.4.2.4 Arbitrary image cloning

Fig. 4.7 shows the cloning of an arbitrary images and its diffraction effects through an ARG medium. In order to elucidate the arbitrary image cloning, we consider the probe beam as a plane wave whereas the pump beam carries complex image such as three letters "ARG" structured at the entrance face of the medium. The initial pump beam structure is depicted

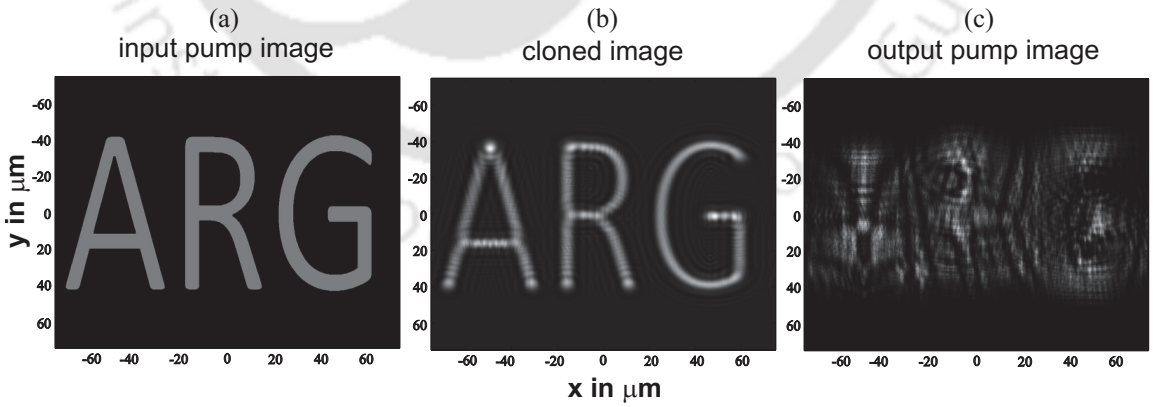

FIGURE 4.7: Arbitrary image cloning in gain medium. (a) Three letters "ARG" are imprinted on pump beam. (b) The efficiently transferred image onto the probe beam after 2 cm length of propagation inside the atomic medium. (c) The transmitted pump beam image which is completely blurred at the exit face of medium. The parameters are same as in Fig. 4.6.

in Fig. 4.7(a). The two-dimensional transverse profile of the pump beam creates gain for the probe beam wherever two-photon Raman condition is satisfied. Hence the transverse pattern of the pump beam can be efficiently transfered to the probe beam. The cloned probe beam also experiences focusing effects at the high intensity regions of the pump beam. Thus the transmitted probe beam has better resolution than the original pump beam images as can be seen in Fig. 4.7(b). Fig. 4.7(c) illustrates that the diffraction induced distortion severely affects the pump beam images and is completely distorted after a propagation of 2 cm.

4.5 Chapter conclusion

In conclusion, we have studied diffractionless steering, splitting and cloning of an optical beam in a Doppler broadened four level *N*-type Raman gain medium using a spatially inhomogeneous pump beam. The spatial pump beam profile gives rise to transverse modulation in the refractive index and gain for the probe beam. The modulated refractive index along with gain can optically form anti-waveguide structure inside the medium. The properties of antiwaveguide structure such as refractive index and gain can be controlled by the application of control field which lead to steering of the probe beam very efficiently. We further demonstrated that a single probe beam can be split into two Gaussian modes when it is injected at the centre between two Gaussian modes of pump beam. We found that the probe beam profile has acquired the shape of the pump beam and propagates without usual diffraction. We next show that the transfer of doughnut-shaped pump image onto a low power Gaussian-shaped probe beam can be possible with high resolution. Finally, by numerical simulations we have established that an arbitrary image with three letters “ARG” imprinted on pump beam can be cloned on to the transmission profile of the probe. The finesse of cloned image has increased twice as compared to the initial resolution of pump images. Thus this scheme might be useful in optical switching, optical lithography, and optical imaging processing.

Chapter 5

Conclusion and future scope

Thesis work would be summarized to highlight the major findings on diffraction management using coherent fields in optical media. We theoretically proposed the possibility of creating structures having widths smaller than those determined by the diffraction-limited images. We achieved controlled optical diffraction with high resolution via spatial modulation of the optical properties of coherent media using spatially dependent coherent fields.

We first reviewed the background of semiclassical theory of light-matter interaction relevant to the central topics of the research work. The study includes fundamentals of two-level and three-level systems along with their linear and nonlinear optical responses. Moving ahead, we derived the paraxial wave equation for a slowly varying electric field by using Maxwell's equations in a dielectric medium. With this we solved the paraxial wave equations in free space to get different standard transverse modes of the electric field.

We investigated optical cloning of arbitrary images encoded in the spatial profile of a control beam onto a probe beam via CPT and EIT resonances. Probe beam propagation has been discussed in both weak probe ($g_0 \ll G_0$) and strong probe ($g_0 \sim G_0$) field limits. Numerical simulation showed that the strong probe field can affect the propagation dynamics of control field. At red detuning of the probe field, a waveguide-like structure is formed inside the medium by applying spatial dependent control beam. This induced waveguide is accompanied with transparency window which allows one to transfer an arbitrary image of the control field onto the transmitted probe field. Interestingly, the feature size of cloned probe field structure is found to be reduced by a factor of two when compared to that of the original control field

structure. However, EIT and CPT based schemes suffer from strong absorption due to breaking of two-photon resonance condition and thus limits its practical implementation. Also, single dark state based method is unable to resolve Rayleigh- and Sparrow-limited images of control field.

To overcome these limitations, we take advantages of double dark resonances (DDR) based schemes to generate high contrast cloned images. For this purpose, we have exploited sharp spectral features of four-level atomic system interacting with three coherent fields and an incoherent pump field. Quantum interference effects induced by DDR result in high contrast feature of refractive index of medium. The sharp features of refractive index are tailored to induce high contrast atomic waveguides by spatially modulated control field. This high contrast features of an induced atomic waveguide enables us to imprint the Rayleigh- or Sparrow-limited control images to probe field with high resolution. The transverse feature of control image is efficiently mapped onto the probe even though the control image suffers severe distortion. In particular, we found that the image contrast of cloned probe enhances significantly in presence of incoherent pump due to increase in transmission.

While EIT-based schemes used in beam guiding and steering suffer from low transmission, Raman gain media overcome this limitation because of their high transmission and large tunability. Thus we studied diffraction-less steering, splitting and cloning of an optical beam in a Doppler broadened four level *N*-type Raman gain medium. This study was focused on all-optical antiwaveguiding effects inside the gain medium utilizing antiwaveguiding effects in the presence of spatially inhomogeneous pump beam. The spatial pump beam profile gives rise to transverse modulation in the refractive index as well as in gain profiles of the probe beam. This modulated refractive index along with gain can optically form antiwaveguide structure which gives rise to probe beam steering inside the medium. Further, optical beam steering, splitting and cloning are controlled by application of an extra control field. In cloning mechanism particularly, a doughnut- and an arbitrary-shaped pump image was successfully transferred onto a low power Gaussian-shaped probe beam. Interstingly, the resolution of cloned images was found to be increased twice as compared to the initial resolution of pump images.

Controlled optical diffraction and enhanced resolution by using elaborate EIT, CPT, DDR and ARG processes might find a vast variety of applications in optical switching, optical lithography, quantum metrology and quantum optical imaging.

Future Scope

There is a great interest in the field of image processing for diffraction-free propagation of multi-colored images. Problem faced with multi-colored images are that they usually get blurred and their contrast degrades rapidly while propagating through optical system or any medium. Diffraction-free propagation of multi-colored images will open a new perspective in the field of quantum information and image processing technologies. This work explores the possibility of diffraction cancellation of colored images propagating through atomic vapor or any solid state media. The simultaneous cancellation of diffraction for laser beams with different wavelengths is still a challenging task. It remains to be seen, if this proposal will be realized and used to investigate the diffraction cancellation for optical fields composed of different wavelengths.

More striking inclination in image creation and processing is to achieve subwavelength scale image resolution. Various broadening mechanisms and short life times of excited states of gaseous media limits the spatial localization of atoms upto sub-wavelength regime. Even more challenging aspect is devising a way to observe sub-wavelength structures specially in microscopy and lithography. Therefore, solid-state systems seem to be more promising than gas phase media because of their wide range of relaxation times.

However, the extremely high nonlinear properties of Rydberg atoms can fulfill the requirements for subwavelength measurement scheme. Rydberg atoms are the excited atoms having one or more electrons in high principal quantum number states. They exhibit very large electric dipole moments which leads to a high nonlinearity. Coupling constants as high as hundreds of kHz are possible in these atoms because of high electric dipole moments. Moreover, Rydberg atoms have very long spontaneous emission times so that long atom-field interactions take place. Rydberg states could persist for long periods of time without being destroyed by collisions. Rydberg atoms exhibit very large electric dipole moments and hence dipole-dipole interactions between the atoms could lead to a high nonlinearity inside the medium. This high nonlinearity can be used in terms of self-phase modulation or cross-phase modulation to control spreading of the laser beam upto sub-wavelength regime.

Appendix A

Split-step Fourier method

This appendix describes the split-step Fourier method to numerically study the beam propagation in an optical medium. It is useful to write Maxwell's wave equation in the following paraxial form

$$\frac{\partial g}{\partial z} = \frac{i}{2k_1}\nabla_\perp^2 g + 2i\pi k_1 \chi\, g\,, \tag{A.1}$$

where $\nabla_\perp^2 = \left(\partial^2/\partial x^2 + \partial^2/\partial y^2\right)$ is the usual "*transverse Laplacian operator*". This equation can not be solved analytically except for some specific cases. Thus a numerical method is needed to solve the above equation in order to see the effects of medium nonlinearity on the beam propagation dynamics. A common method that has been used to solve the Eq. (A.1) in nonlinear dispersive media is the split-step Fourier method. The basic principles behind the split-step Fourier method can be understood by rewriting the above equation in the operator form

$$\frac{\partial g}{\partial z} = (\hat{D} + \hat{S})g\,, \tag{A.2}$$

where $\hat{D} = (i/2k_1)\nabla_\perp^2$ is a differential operator that is attributed to diffraction in free-space or medium. The operator $\hat{S} = 2i\pi k\chi$, is a nonlinear operator that describes dispersion and loss (or gain) mechanisms due to the medium. The operator $\hat{S}$ is usually space dependent and referred as an inhomogeneous operator. Assuming that the operator $\hat{S}$ is z-independent, an

exact solution of the Eq. (A.2) for a small propagation distance Δz is given by

$$g(x, y; z + \Delta z) = \exp[(\hat{D} + \hat{S})\Delta z] g(x, y; z) . \tag{A.3}$$

Generally, the operators $\hat{D}$ and $\hat{S}$ act all together on g along the length of the optically written waveguide. However, for a small step Δz, we can separate out the effects of diffraction and nonlinearity and treat them independently. We thus perform the calculation for beam propagation from z to $z+\Delta z$ in two steps. The nonlinearity acts alone in the first step while keeping the diffraction operator zero, $\hat{D}$=0. In the second step, diffraction acts alone, and inhomogeneous operator is zero, $\hat{S}$=0. This method is known as split-step operator method which provides an approximate solution of beam propagation equation over a small distance Δz. The approximate solution can be obtained by applying the Baker-Campbell-Hausdorff (BCH) formula for two non-commuting operators $\hat{X}$ and $\hat{Y}$ which is given by

$$\exp(\hat{X})\exp(\hat{Y}) = \exp[\hat{X} + \hat{Y} + \frac{1}{2}[\hat{X}, \hat{Y}] + \frac{1}{12}[\hat{X}, \hat{X}, \hat{Y}] + [\hat{X}, \hat{X}, \hat{Y}] + ... \tag{A.4}$$

Applying this BCH formula in the Eq. (A.3) along with $\hat{X} = \hat{D}\Delta z$ and $\hat{Y} = \hat{S}\Delta z$, we get

$$\exp(\hat{D}\Delta z)\exp(\hat{S}\Delta z) = \exp[\hat{D}\Delta z + \hat{S}\Delta z + \frac{1}{2}[\hat{D}, \hat{S}](\Delta z)^2 + ...] , \tag{A.5}$$

where $[\hat{D}, \hat{S}] = (\hat{D}\hat{S} - \hat{S}\hat{D})$ represents the commutation of $\hat{D}$ and $\hat{S}$. Thus for accuracy up to second-order in Δz, we obtain

$$\exp[(\hat{D} + \hat{S})\Delta z] \simeq \exp(\hat{D}\Delta z)\exp(\hat{S}\Delta z) . \tag{A.6}$$

Eq. (A.6) simply indicates that the diffraction and the inhomogeneous operators can be treated independently. Therefore, we can write approximate solution of Eq. (A.3) as

$$g(x, y; z + \Delta z) = \exp(\hat{S}\Delta z)\exp(\hat{D}\Delta z) g(x, y; z) . \tag{A.7}$$

The exponential containing operator $\hat{S}$ in Eq. (A.7) is evaluated in the real space domain. In contrast, the exponential involving operator $\hat{D}$ in Eq. (A.7) can be evaluated in the Fourier

domain using free-space transfer function. Mathematically, it is expressed as

$$\exp(\hat{D}\Delta z)g = \mathcal{F}^{-1}\left\{\exp\left[\frac{-i(k_x^2+k_y^2)\Delta z}{2k_0}\right]\mathcal{F}\{g\}\right\}, \tag{A.8}$$

where $\mathcal{F}$ and $\mathcal{F}^{-1}$ denote the Fourier transform and inverse Fourier transform operations, respectively. Therefore, the algorithm for a single step in Δz can be written as

$$g(x,y;z+\Delta z) = \exp(\hat{S}\,\Delta z)\exp(\hat{D}\Delta z)g(x,y;z) \tag{A.9}$$

$$= \exp(2i\pi k\chi\Delta z)\mathcal{F}^{-1}\left\{\exp\left[\frac{-i(k_x^2+k_y^2)\Delta z}{2k_0}\right]\mathcal{F}\{g\}\right\}. \tag{A.10}$$

The accuracy of the split-step Fourier method can be further improved by repeated application of BCH formula of Eq. (A.4). For this purpose, we consider the following expansion

$$\begin{aligned}\exp(\hat{X})\exp(\hat{Y})\exp(\hat{X}) = \exp\Big(2\hat{X}+\hat{Y}+\frac{1}{6}[\hat{Y},\hat{Y},\hat{X}]-\frac{1}{6}[\hat{X},\hat{X},\hat{Y}]\\ +\frac{7}{360}[\hat{X},\hat{X},\hat{X},\hat{X},\hat{Y}]-\frac{1}{360}[\hat{Y},\hat{Y},\hat{Y},\hat{Y},\hat{X}]+\frac{1}{90}[\hat{X},\hat{Y},\hat{Y},\hat{Y},\hat{X}]\\ +\frac{1}{45}[\hat{Y},\hat{X},\hat{X},\hat{X},\hat{Y}]-\frac{1}{60}[\hat{X},\hat{X},\hat{Y},\hat{Y},\hat{X}]+\frac{1}{30}[\hat{Y},\hat{Y},\hat{X},\hat{X},\hat{Y}]+\ldots\Big).\end{aligned} \tag{A.11}$$

Substituting $\hat{X} = \hat{D}\Delta z$ and $\hat{Y} = \hat{S}\,\Delta z$ in above equation, we find that

$$\exp(\hat{D}\frac{\Delta z}{2})\exp(\hat{S}\,\Delta z)\exp(\hat{D}\frac{\Delta z}{2}) = \exp(\Delta z\alpha_1+\Delta z^3\alpha_3+\Delta z^5\alpha_5+\Delta z^7\alpha_7+\ldots), \tag{A.12}$$

where $\alpha_1 = \hat{D}+\hat{S}$, $\alpha_3 = \frac{1}{12}[\hat{S},\hat{S},\hat{D}]-\frac{1}{24}[\hat{D},\hat{D},\hat{S}]$, $\alpha_5 = [\hat{D},\hat{D},\hat{D},\hat{D},\hat{S}]+\ldots$.

In this procedure, the Eq. (A.7) is modified as

$$g(x,y;z+\Delta z) = S_3(\lambda)g(x,y;z), \tag{A.13}$$

where $S_3(\lambda)$ is third-order symmetrized split-step operator and is expressed as

$$S_3(\lambda) = \exp(\hat{D}\frac{\Delta z}{2})\exp(\hat{S}\,\Delta z)\exp(\hat{D}\frac{\Delta z}{2}). \tag{A.14}$$

This method is known as symmetrized split-step Fourier method because of the symmetric

form of the exponential operators in Eq. (A.14). The benefit of using symmetrized form is that the leading error term results in third-order in the step size Δz due to double commutator. The main difference between second-order and third-order accuracy method is that the effect of nonlinearity is included in the middle of the segment than the segment boundary. We now calculate higher-order accuracies from this third-order symmetrized split-step operator.

The fifth-order split-step operator is obtained by symmetric product of third-order split-step operator

$$S_5(\Delta z) = S_3(\omega\Delta z)S_3(\omega_0\Delta z)S_3(\omega\Delta z)\,, \tag{A.15}$$

where the middle term $S_3(\omega_0\Delta z)$ is given by

$$S_3(\omega_0\Delta z) = \exp(\omega_0\Delta z\alpha_1 + \omega_0^3\Delta z^3\alpha_3 + \omega_0^5\Delta z^5\alpha_5 + \omega_0^7\Delta z^7\alpha_7 + ...)\,. \tag{A.16}$$

While two sides terms $S_3(\omega\Delta z)$ are calculated as

$$S_3(\omega\Delta z) = \exp(\omega\Delta z\alpha_1 + \omega^3\Delta z^3\alpha_3 + \omega^5\Delta z^5\alpha_5 + \omega^7\Delta z^7\alpha_7 + ...)\,. \tag{A.17}$$

Substituting these expansions in Eq. (A.15), We get

$$S_5(\Delta z) = \exp[(\omega_0 + 2\omega)\Delta z\alpha_1 + (\omega_0^3 + 2\omega^3)\Delta z^3\alpha_3 + (\omega_0^5 + 2\omega^5)\Delta z^5\alpha_5 + (\omega_0^7 + 2\omega^7)\Delta z^7\alpha_7 + ...]\,. \tag{A.18}$$

In order to achieve fifth-order accuracy, following two conditions must be satisfied

$$\omega_0 + 2\omega = 1, \quad \text{and} \quad \omega_0^3 + 2\omega^3 = 0\,. \tag{A.19}$$

These two conditions imply that $2\omega^3 + (1 - 2\omega)^3 = 0$ which obviously has a unique real solution $\omega = 1/(2 - 2^{1/3})$. Hence, the fifth-order split-step operator can be rewritten as

$$S_5(\Delta z) = S_3(\omega\Delta z)S_3[(1 - 2\omega)\Delta z]S_3(\omega\Delta z)\,. \tag{A.20}$$

Further, the higher order accuracies can be also obtained by extending same approach of the BCH [191–193]. The seventh-order accuracy is given by

$$S_7(\lambda) = S_3(\omega_3\lambda)S_3(\omega_2\lambda)S_3(\omega_1\lambda)S_3(\omega_0\lambda)S_3(\omega_1\lambda)S_3(\omega_2\lambda)S_3(\omega_3\lambda)\,, \tag{A.21}$$

where

$$\omega_3 = 0.784513610477560 \tag{A.22}$$

$$\omega_2 = 0.235573213359357 \tag{A.23}$$

$$\omega_1 = -1.177679984178870 \tag{A.24}$$

$$\omega_0 = 1 - 2(\omega_1 + \omega_2 + \omega_3)\,. \tag{A.25}$$

Similarly, the ninth-order accuracy is given by

$$\begin{aligned} S_9(\lambda) =& S_3(\omega_7\lambda)S_3(\omega_6\lambda)S_3(\omega_5\lambda)S_3(\omega_4\lambda)S_3(\omega_3\lambda)S_3(\omega_2\lambda)S_3(\omega_1\lambda)S_3(\omega_0\lambda) \\ &\times S_3(\omega_1\lambda)S_3(\omega_2\lambda)S_3(\omega_3\lambda)S_3(\omega_4\lambda)S_3(\omega_5\lambda)S_3(\omega_6\lambda)S_3(\omega_7\lambda)\,, \end{aligned} \tag{A.26}$$

where

$$\omega_7 = 0.629030650210433 \tag{A.27}$$

$$\omega_6 = 1.369349464166871 \tag{A.28}$$

$$\omega_5 = -1.064587147891830 \tag{A.29}$$

$$\omega_4 = 1.663358099633150 \tag{A.30}$$

$$\omega_3 = -1.678969282596400 \tag{A.31}$$

$$\omega_2 = -1.559468038214470 \tag{A.32}$$

$$\omega_1 = 0.311790812418427 \tag{A.33}$$

$$\omega_0 = 1 - 2(\omega_1 + \omega_2 + \omega_3 + \omega_4 + \omega_5 + \omega_6 + \omega_7)\,. \tag{A.34}$$

We now consider a special case where inhomogeneous operator $\hat{S}$ is z-dependent within a propagation distance Δz. In this case, exponential form of solution for the operator $\hat{S}$ as in Eq. (A.3) is no longer valid. Thus, we split the Eq. (A.2) into its linear and nonlinear part and

solve them separately. The linear part is given by

$$\frac{\partial g_D}{\partial z} = \hat{D} g \,. \tag{A.35}$$

Solution of this equation can be written in the Fourier domain as follows

$$g_D(x, y; z + \Delta z) = \exp(\hat{D}\Delta z) g(x, y; z) \tag{A.36}$$

$$= \mathcal{F}^{-1} \left\{ \exp\left[\frac{-i(k_x^2 + k_y^2)\Delta z}{2k_0} \right] \mathcal{F}\{g\} \right\} . \tag{A.37}$$

The nonlinear part is given by

$$\frac{\partial g}{\partial z} = \hat{S}(z) g_D = f(S(z), g_D) \,. \tag{A.38}$$

This equation can be solved by using 4th order Runge-Kutta method. Thus the solution can be written as

$$g(x, y; z + \Delta z) = g_D(x, y; z + \Delta z) + \frac{1}{6}(\mathrm{K}_1 + 2\mathrm{K}_2 + 2\mathrm{K}_3 + \mathrm{K}_4)\Delta z \,, \tag{A.39}$$

where

$$\begin{aligned} \mathrm{K}_1 &= f(z, g_D) \\ \mathrm{K}_2 &= f(z + \Delta z/2, g_D + \mathrm{K}_1 \Delta z/2) \\ \mathrm{K}_3 &= f(z + \Delta z/2, g_D + \mathrm{K}_2 \Delta z/2) \\ \mathrm{K}_4 &= f(z + \Delta z/2, g_D + \mathrm{K}_3 \Delta z) \,. \end{aligned}$$

Bibliography

[1] F. A. Jenkins and H. E. White, *Fundamentals of Optics*, (McGraw-Hill, New York, 1976).

[2] L. Rayleigh, Philos. Mag. **8**, 261 (1879).

[3] J. M. Vigoureux and D. Courjon, Appl. Opt. **31** , 3170 (1992).

[4] G. Keiser, *Optical Fiber Communications*, (McGraw-Hill, New York, 2000).

[5] R. Y. Chiao, E. Garmire, and C. H. Townes, Phys. Rev. Lett. **13**, 479 (1964).

[6] P. L. Kelley, Phys. Rev. Lett. **15**, 1005 (1965).

[7] M. Tiemann, T. Halfmann, and T. Tschudi, Opt. Commun. **188**, 3612 (2001).

[8] J. S. Aitchison, A. M. Werner, Y. Silverberg, M. K. Oliver, J. L. Jackel, D. E. Laird, E. M. Vogelm, and P. W E. Smith, Opt. Lett. **15**, 471 (1990).

[9] G. R. Allen, S. R. Skinner, D. R. Andersen, and A. L. Smirl, Opt. Lett. **16**, 156 (1991).

[10] D. Grischkowsky, Phys. Rev. Lett. **24**, 866 (1970).

[11] E. Bjorkholm and A. Ashkin, Phys. Rev. Lett. **32**, 129 (1974).

[12] R. De La Fuenta, A. Barthelemy, and C. Froehly, Opt. Lett. **16**, 793 (1991).

[13] B. L.-Davies and Y. Xiaoping, Opt. Lett. **17**, 496 (1992).

[14] B. L.-Davies and Y. Xiaoping, Opt. Lett. **17**, 1775 (1992).

[15] M. Morin, G. Duree, and G. Salamo, Opt. Lett. **20**, 2066 (1995).

[16] D. B.-Arbiv, A. D. W.-Gordon, and H. Friedmann, Phys. Rev. A **58**, R3403 (1998).

[17] D. B.-Arbiv, A. D. W.-Gordon, and H. Friedmann, Phys. Rev. A **61**, 033806 (2000).

[18] R. W. Boyd, M.G. Raymer, P. Narum, and D. J. Harter, Phys. Rev. A **24**, 411 (1981).

[19] J. F. Valley, G. Khitrova, H. M. Gibbs J. W. Grantham, and Xu. Jianjin, Phys. Rev. Lett. **64**, 2362 (1990).

[20] R. W. Boyd, *Nonlinear Optics*, (Academic, New York, 1992).

[21] T. Hong, Phys. Rev. Lett. **90**, 1005 (2003).

[22] M. D. Lukin, Rev. Mod. Phys. **75**, 457 (2003).

[23] E. Arimondo, *Progress in Optics*, **35**, 257 (1996).

[24] M. O. Scully and M. S. Zubairy, *Quantum Optics*, (Cambridge University Press, Cambridge, England, 1997).

[25] S. E. Harris, Phys. Today **50(7)**, 36 (1997).

[26] M. Fleischhauer, and A. Imamoglu, and J. P. Marangos, Rev. Mod. Phys. **77**, 663 (2005).

[27] S. E. Harris, Phys. Rev. Lett. **62**, 1033 (1989).

[28] M. O. Scully, S. Y. Zhu, and A. Gavrielides, Phys. Rev. Lett. **62**, 2813 (1989).

[29] A. Imamolu, J. E. Field, and S. E. Harris, Phys. Rev. Lett. **66**, 1154 (1991).

[30] O. Kocharovskaya, Phys. Rep. **219**, 175 (1992).

[31] T. W. Hansch, M. D. Levenson, and A. L. Schawlow, Phys. Rev. Lett. **26**, 946 (1971).

[32] G. S. Agarwal and T. N. Dey, Laser & Photonics Reviews **3**, 287 (2009).

[33] M. O. Scully, Phys. Rev. Lett. **67**, 1855 (1991); M. Fleischhauer, C. H. Keitel, M. O. Scully, C. Su, B. T. Ulrich and S. Y. Zhu, Phys. Rev. A **47**, 1468 (1992); U. Rathe, M. Fleischhauer, Shi-Yao Zhu, T. W. Hansch and M. O. Scully, Phys. Rev. A **47**, 4994 (1993).

[34] A. S. Zibrov, M. D. Lukin, L. Hollberg, D. E. Nikonov, M. O. Scully, H. G. Robinson, and V. L. Velichansky, Phys. Rev. Lett. **76**, 3935 (1996).

[35] C. O'Brien, and O. Kocharovskaya, Phys. Rev. Lett. **107**, 137401 (2011).

[36] Z. J. Simmons, N. A. Proite, J. Miles, D. E. Sikes, and D. D. Yavuz, Phys. Rev. A **85**, 053810 (2012).

[37] G. S. Agarwal and S. Dasgupta, Phys. Rev. A **70**, 023802 (2004).

[38] L. Deng, and M. G. Payne, Phys. Rev. Lett. **98**, 253902 (2007).

[39] S. Ghosh, A. R. Bhagwat, C. K. Renshaw, S. Goh, and A. L. Gaeta, Phys. Rev. Lett. **97**, 023603 (2006).

[40] S. M. Spillane, G. S. Pati, K. Salit, M. Hall, P. Kumar, R. G. Beausoleil, and M. S. Shahriar, Phys. Rev. Lett. **100**, 233602 (2008).

[41] R. R. Moseley, S. Shepherd, D. J. Fulton, B. D. Sinclair, and M. H. Dunn, Phys. Rev. Lett. **74**, 670 (1995).

[42] R. R. Moseley, S. Shepherd, D. J. Fulton, B. D. Sinclair, and M. H. Dunn, Phys. Rev. A **53**, 408 (1996).

[43] A. Kasapi, Maneesh Jain, G. Y. Yin, and S.E. Harris, Phys. Rev. Lett. **74**, 2447 (1995).

[44] A. G. Truscott, M. E. J. Friese, N. R. Heckenberg, and H. Rubinsztein-Dunlop, Phys. Rev. Lett. **82**, 1438 (1999).

[45] R. Kapoor and G. S. Agarwal, Phys. Rev. A **61**, 053818 (2000).

[46] J.A. Andersen, M.E.J. Friese, A.G. Truscott, Z. Ficek, P.D. Drummond, N.R. Heckenberg, and H. Rubinsztein-Dunlop, Phys. Rev. A **63**, 023820 (2001).

[47] D. R. Walker, D. D. Yavuz, M. Y. Shverdin, G. Y. Yin, A. V. Sokolov, and S. E. Harris, Opt. Lett. **27**, 2094 (2002).

[48] N. A. Proite, B. E. Unks, J. T. Green, and D. D. Yavuz, Phys. Rev. A **77**, 023819 (2008).

[49] J. Cheng, S. Han, and Y. Yan, Phys. Rev. A **72**, 021801(R) (2005); J. Cheng and S. Han, Phys. Rev. A **76**, 023826 (2007).

[50] M. Vengalattore and M. Prentiss, Phys. Rev. Lett. **95**, 243601 (2005).

[51] J. Cheng and S. Han, Opt. Lett. **32**, 1162 (2007).

[52] Q. Sun, Y. V. Rostovtsev, and M. S. Zubairy, Phys. Rev. A **74**, 033819 (2006).

[53] V. A. Sautenkov, H. Li, Y. V. Rostovtsev, and M. O. Scully, Phys. Rev. A **81**, 063824 (2010).

[54] L. Zhang, T. N. Dey, and J. Evers, Phys. Rev. A **87**, 043842 (2013).

[55] M. S. Bigelow, N. N. Lepeshkin, and R. W. Boyd, Phys. Rev. Lett. **90**, 113903 (2003); M. S. Bigelow, N. N. Lepeshkin, and R. W. Boyd, Science, **301**, 200 (2003).

[56] E. Baldit, K. Bencheikh, P. Monnier, J. A. Levenson, and V. Rouget, Phys. Rev. Lett. **95**, 143601 (2005).

[57] T. N. Dey and G. S. Agarwal, Opt. Lett. **34**, 3199 (2009).

[58] P. K. Vudyasetu, D. J. Starling, and J. C. Howell, Phys. Rev. Lett. **102**, 123602 (2009).

[59] D. Kip, C. Anastassiou, E. Eugenieva, D. Christodoulides, and M. Segev, Opt. Lett. **26**, 524 (2001).

[60] O. Firstenberg, M. Shuker, N. Davidson, and A. Ron, Phys. Rev. Lett. **102**, 043601 (2009).

[61] O. Firstenberg, P. London, M. Shuker, A. Ron, and N. Davidson, Nat. Phys. **5**, 665 (2009).

[62] O. Firstenberg, M. Shuker, A. Ron, and N. Davidson, Rev. Mod. Phys. **85**, 941 (2013).

[63] L. Zhang and J. Evers, Phys. Rev. A **89**, 013817 (2014).

[64] T. N. Dey, and J. Evers, Phys. Rev. A **84**, 043842 (2011).

[65] C. Hettich, Science **298**, 385 (2002).

[66] S. W. Hell, Science **316**, 1153 (2007).

[67] M. Dyba and S. W. Hell, Phys. Rev. Lett. **88**, 163901 (2002).

[68] V. Westphal and S. W. Hell, Phys. Rev. Lett. **94**, 143903 (2005).

[69] S. Bretschneider, C. Eggeling, and S. W. Hell, Phys. Rev. Lett. **98**, 218103 (2007);

[70] J. E. Thomas, Phys. Rev. A **42**, 5652 (1990).

[71] K. D. Stokes, C. Schnurr, J. R. Gardner, M. Marable, G. R. Welch, and J. E. Thomas, Phys. Rev. Lett. **67**, 1997 (1991); J. R. Gardner,M. L. Marable, G. R. Welch, and J. E. Thomas, Phys. Rev. Lett. **70**, 3404 (1993).

[72] A. M. Herkommer, W. P. Schleich, and M. S. Zubairy, J. Mod. Opt. **44**, 2507 (1997).

[73] Q. Gulfam and J. Evers, J. Phys. B **43**, 045501 (2010).

[74] J.-T. Chang, J. Evers, M. O. Scully, and M. S. Zubairy, Phys. Rev. A **73**, 031803(R) (2006); J.-T. Chang, J. Evers, and M. S. Zubairy, Phys. Rev. A **74**, 043820 (2006).

[75] S. I. Schmid and J. Evers, Phys. Rev. A **81**, 063805 (2010).

[76] P. Storey, M. Collett, and D. F. Walls, Phys. Rev. Lett. **68**, 472 (1992); P. Storey, M. Collett, and D. Walls, Phys. Rev. A **47**, 405 (1993);

[77] R. Quadt, M. Collett, and D. F. Walls, Phys. Rev. Lett. **74**, 351 (1995).

[78] S. Kunze, K. Dieckmann, and G. Rempe, Phys. Rev. Lett. **78**, 2038 (1997).

[79] M. Holland, S. Marksteiner, P. Marte, and P. Zoller, Phys. Rev. Lett. **76**, 3683 (1996).

[80] S. Qamar, S.-Y. Zhu, and M. S. Zubairy, Phys. Rev. A **61**, 063806 (2000).

[81] A. V. Gorshkov, L. Jiang, M. Greiner, P. Zoller, and M. D. Lukin, Phys. Rev. Lett. **100**, 093005 (2008).

[82] S. Qamar, S.-Y. Zhu, and M. S. Zubairy, Opt. Commun. **176**, 409 (2000).

[83] F. Ghafoor, S.-Y. Zhu, and M. S. Zubairy, Phys. Rev. A **62**, 013811 (2000).

[84] M. Sahrai, H. Tajalli, K. T. Kapale, and M. S. Zubairy, Phys. Rev. A **72**, 013820 (2005).

[85] S. Qamar, A. Mehmood, and S. Qamar, Phys. Rev. A **79**, 033848 (2009).

[86] C. A. Mack, *Fundamental Principles of Optical Lithography: the Science of Microfabrication*, (Wiley, West Sussex, England, 2007);

[87] A. N. Boto, P. Kok, D. S. Abrams, S. L. Braunstein, C. P. Williams, and J. P. Dowling, Phys. Rev. Lett. **85**, 2733 (2000).

[88] M. DAngelo, M. V. Chekhova, and Y. Shih, Phys. Rev.Lett. **87**, 013602 (2001).

[89] M. Kiffner, J. Evers, and M. S. Zubairy, Phys. Rev. Lett. **100**, 073602 (2008).

[90] Z. Liao, M. Al-Amri, and M. S. Zubairy, Phys. Rev. Lett. **105**, 183601 (2010).

[91] P. R. Hemmer, A. Muthukrishnan, M. O. Scully, and M. S. Zubairy, Phys. Rev. Lett. **96**, 163603 (2006); Q. Sun, P. R. Hemmer, and M. S. Zubairy, Phys. Rev. A **75**, 065803 (2007).

[92] H. S. Park, S. K. Lee, and J. Y. Lee, Opt. Exp. **16**, 21982 (2008).

[93] J. D. Jackson, *Classical Electrodynamics*, (Wiley, New York, 1962).

[94] L. Allen and J. H. Eberly, *Optical resonance and two-level atoms*, (Wiley, New York, 1975).

[95] I. I. Rabi, Phys. Rev. **51**, 652 (1937).

[96] R. Louden, *The Quantum Theory of Light*, (Clarendon Press, Oxford, 1983).

[97] M.O. Scully, Phys. Rep. **219**, 191 (1992).

[98] M. Fleischhauer, C. H. Keitel, M. O. Scully, C. Su, B. T. Ulrich and S. Y. Zhu, Phys. Rev. A **46**, 1468 (1992).

[99] T. W. Hansch, M. D. Levenson, and A. L. Schawlow, Phys. Rev. Lett. **26**, 946 (1971).

[100] M. Nilsson and S. Kroll, Opt. Commun. **247**, 393 (2005).

[101] S. L. McCall and E. L. Hahn, Phys. Rev. Lett. **18**, 908 (1967); S. L. McCall and E. L. Hahn, Phys. Rev. **183**, 82 (1969).

[102] G. L. Lamb, Jr., Rev. Mod. Phys. **43**, 99 (1971).

[103] H. A. Haus, Rev. Mod. Phys. **51**, 331 (1979).

[104] M. Fleischhauer, and A. Imamoglu, and J. P. Marangos, Rev. Mod. Phys. **77**, 663 (2005).

[105] S. H. Autler and C. H. Townes, Phys. Rev. **100**, 703 (1955).

[106] S. P. Tewari and G.S. Agarwal, Phys. Rev. Lett. **56**, 1811 (1986).

[107] S. E. Harris, J. E. Field, and A. Imamoglu, Phys. Rev. Lett. **64** 1107 (1990).

[108] K.-J. Boller, A. Imamo lu, and S. E. Harris, Phys. Rev. Lett. **66**, 2593 (1991).

[109] J. E. Field, K. H. Hahn, and S. E. Harris, Phys. Rev. Lett. **67**, 3062 (1991).

[110] M. Xiao, Y. Q. Li, S. Z. Jin, and J. Gea-Banacloche, Phys. Rev. Lett. **74**, 666 (1995); Y.-Q. Li and M. Xiao, Phys. Rev. A **51**, R2703 (1995).

[111] L. V. Hau, S. E. Harris, Z. Dutton, and C. H. Behroozi, Nature Phys. **397**, 594 (1999).

[112] M. M. Kash, V. A. Sautenkov, A. S. Zibrov, L. Hollberg, G. R. Welch, M. D. Lukin, Y. Rostovtsev, E. S. Fry, and M. O. Scully, Phys. Rev. Lett. **82**, 5299 (1999).

[113] D. L. Fisher and T. Tajima, Phys. Rev. Lett. **71**, 4338 (1993).

[114] L. J. Wang, A. Kuzmich, and A. Dogariu, Nature (London) **406**, 277 (2000).

[115] M.D. Lukin and A. Imamoglu, Nature(London) **413**, 273 (2001).

[116] M. Shuker, O. Firstenberg, R. Pugatch, A. Ron, and N. Davidson, Phys. Rev. Lett. **100**, 223601 (2008).

[117] G. S. Agarwal, *Quantum Optics*, (Cambridge University Press, New York, 2013).

[118] G. Alzetta, A. Gozzini, L. Moi, and G. Orriols, Nuovo Cimento B **36**, 5 (1976); G. Alzetta and L. Moi, and G. Orriols, Nuovo Cimento B **52**, 209 (1979).

[119] G. Orriols, Nuovo Cimento A **53**, 1 (1979);

[120] E. S. Fry, X. Li, D. Nikonov, G. G. Padmabandu, M. O. Scully, A. V. Smith, F. K. Tittel, C. Wang, S. R. Wilkinson, and S. Y. Zhu, Phys. Rev. Lett. **70**, 3235 (1993).

[121] S. Schiemann, A. Kuhn, S. Steuerwald, and K. Bergmann, Phys. Rev. Lett. **71** 3637 (1993).

[122] J. E. Thomas, P. R. Hemmer, S. Ezekiel, C. C. Leiby, Jr., R. H. Picard, and C. R. Willis, Phys. Rev. Lett. **48** 867 (1982).

[123] S. Knappe, V. Shah, P. D. D. Schwindt, L. Hollberg, J. Kitching, Li-Anne Liew, and J. Moreland, Appl. Phys. Lett. **85** 1460 (2004).

[124] M. Merima, T. Lindvall, I. Tittonen, and E. Ikonen, J. Opt. Soc. Am. B **20** 273 (2003).

[125] S. Knappe, P. D. D. Schwindt, V. Shah, L. Hollberg, and J. Kitching, Opt. Exp. **13** 1249 (2005)

[126] B. A. A. Saleh and M. C. Teich, *Fundamentals of Photonics*, (John Wiley & Sons, New York, 1991).

[127] M. Born and E. Wolf, *Principles of Optics*, (Cambridge University Press, Cambridge, England, 1999).

[128] M. V. Berry and N. L. Balazs, Am. J. Phy. **47**, 264 (1979).

[129] G. A. Siviloglou, J. Broky, A. Dogariu, and D. N. Christodoulides, Phys. Rev. Lett. **99**, 213901 (2007).

[130] J. Durnin, J. J. Miceli, Jr., and J. H. Eberly, Phys. Rev. Lett. **58**, 1499 (1987).

[131] D. McGloina and K. Dholakia, Contemporary Physics **46**, 15 (2005).

[132] J. C. Gutiérrez-Vega, M. D. Iturbe-Castillo, and S. Chávez-Cerda, Opt. Lett. **25**, 1493 (2000).

[133] P. Zhang, Y. Hu, T. Li, D. Cannan, X. Yin, R. Morandotti, Z. Chen, and X. Zhang, Phys. Rev. Lett. **109**, 193901 (2012).

[134] A. E. Siegman, *Lasers*, (University Science Books, Sausalito, California, 1986).

[135] A. Y. Savchencko and B. Y. Zel'dovich, J. Opt. Soc. Am. B **13**, 273 (1996).

[136] P. A. Belanger, R. L. Lachance, and C. Pare, Opt. Lett. **17**, 793 (1992).

[137] J. Bourderionnet, A. Brignon, J. P. Huignard, A. Delboulbe, and B. Loiseaux, Opt. Lett. **26**, 1958 (2001).

[138] D. Deng, Opt. Commun. **259**, 409 (2006); D. Deng and Q. Guo, Opt. Lett. **33**, 1225 (2008).

[139] D. Yankelev, O. Firstenberg, M. Shuker, and N. Davidson, Opt. Lett. **33**, 1225 (2008).

[140] A. A. Tovar, J. Opt. Soc. Am. A **13**, 962 (1996).

[141] L. Allen, M. W. Beijerbergen, R. J. C. Spreeuw, and J. P. Woerdman, Phys. Rev. A **45**, 8185 (1992).

[142] N. R. Heckenberg, R. McDuff, C. P. Smith, H. RubinszteinDunlop, and M. J. Wegener, Opt. Quantum Electron. **24**, 5951 (1992).

[143] L. Zhao, T. Wang, and S. F. Yelin, Opt. Lett. **34**, 1930 (2009).

[144] Y.-X. Ren, M. Li, K. Huang, J.-G. Wu, H.-F. Gao, Z.-Q. Wang, and Y.-M. Li, Appl. Opt. **49**, 1838 (2010).

[145] M. Mitsunaga, M. Yamashita, and H. Inoue, Phys. Rev. A **62**, 013817 (2000).

[146] G. S. Agarwal and K. T. Kapale, J. Phys. B **39**, 3437 (2006).

[147] D. D. Yavuz and N. A. Proite, Phys. Rev. A **76**, 041802(R) (2007).

[148] K. T. Kapale and G. S. Agarwal, Opt. Lett. **35**, 2792 (2010).

[149] A. D. Greentree, D Richards, J. A. Vaccaro, A. V. Durrant, S. R. de Echaniz, D. M. Segal, and J. P. Marangos, Phys. Rev. A **67**, 023818 (2003).

[150] D. Strekalov, A. B. Matsko,L. Maleki, J. Opt. Soc. Am. B **22**, 65 (2005).

[151] A. Vudayagiri, S. P. Tewari, J. Phys. B: At. Mol. Opt. Phys. **39**, 3919 (2006).

[152] T. N. Dey and G. S. Agarwal, Phys. Rev. A **67**, 033813 (2003).

[153] H. Li, V. A. Sautenkov, M. M. Kash, A. V. Sokolov, G. R. Welch, Y. V. Rostovtsev, M. S. Zubairy, and M. O. Scully, Phys. Rev. A **78**, 013803 (2008).

[154] R. Barakat, J. Opt. Soc. Am. **52**, 276 (1962).

[155] A. J. d. Dekker and A. v. d. Bos, J. Opt. Soc. Am. A **14**, 547 (1997).

[156] M. D. Lukin, S. F. Yelin, M. Fleischhauer, and M. O. Scully, Phys. Rev. A **60**, 3225 (1999).

[157] Y. C. Chen, Y. A. Liao, H. Y. Chiu, J. J. Su, and I. A. Yu, Phys. Rev. A **64**, 053806 (2001).

[158] S. F. Yelin, V. A. Sautenkov, M. M. Kash, G. R. Welch, and M. D. Lukin, Phys. Rev. A **68**, 063801 (2003).

[159] C. Y. Ye, A. S. Zibrov, Y. V. Rostovtsev, and M. O. Scully, Phys. Rev. A **65**, 043805 (2002).

[160] H. Wang and X. Peng, J. Opt. Soc. Am. B **29**, 429 (2012).

[161] G. P. Agrawal, Phys. Rev. Lett. **64**, 2487 (1990).

[162] F. O. Fahrbach and A. Rohrbach, Nat. Commun. **3**, 632 (2012).

[163] C. A. Mack, *Fundamental Principles of Optical Lithography: the Science of Microfabrication*, (Wiley, West Sussex, England, 2007); R. T. Glasser, H. Cable, and J. P. Dowling, F. De Martini, F. Sciarrino, and C. Vitelli, Phys. Rev. A **78**, 012339 (2008); V. Giovannetti, S. Lloyd, L. Maccone, and J. H. Shapiro, Phys. Rev. A **79**, 013827 (2009).

[164] Z. Nie, H. Zheng, Y. Zhang, Y. Zhao, C. Zuo, C. Li, H. Chang, and M. Xiao, Opt. Exp. **18**, 899 (2010).

[165] I. Cindrich, Appl. Opt. **6**, 1531 (1967).

[166] D. H. McMahon, A. R. Franklin, and J. B. Thaxter, Appl. Opt. **8**, 399 (1969).

[167] W. B. Jackson, N. M. Amer, A. C. Boccara, and D. Fournier, Appl. Opt. **20**, 1333 (1981).

[168] J. D. Zook, Appl. Opt. **13**, 875 (1974).

[169] R. W. Dixon, J. Appl. Phys. **38**, 5149 (1967).

[170] G. P. Agrawal, Phys. Rev. Lett. **64**, 2487 (1990).

[171] A. T. Ryan and G. P. Agrawal, Opt. Lett. **18**, 1795 (1993).

[172] Y. Li, D. Y. Chen, L. Yang, and R. R. Alfano, Opt. Lett. **16**, 438 (1991).

[173] A. J. Stentz, M. Kauranen, J. J. Maki, G. P. Agrawal, and R. W. Boyd, Opt. Lett. **17**, 19 (1992).

[174] D. L. Zhou, L. Zhou, R. Q. Wang, S. Yi, and C. P. Sun, Phys. Rev. A **76**, 055801 (2007).

[175] C. Zhu, L. Deng, and E. W. Hagley, Phys. Rev. A **88**, 013841 (2013).

[176] G. P. Agrawal, Phys. Rev. Lett. **59**, 880(1987).

[177] G. P. Agrawal, J. Opt. Soc. Am. B **7**, 1072 (1990).

[178] E. Lantz, Nat. Photon. **2**, 71 (2008).

[179] B. E. Cohen, Nature **467**, 407 (2010).

[180] D. Ding, Z. Zhou and B. Shi, Opt. Lett. **39**, 240 (2014).

[181] M. Cao, L. Zhang,Y. Yu,F. Ye, D. Wei, W. Guo,S. Zhang, H. Gao, and F. Li, Opt. Lett. **39**, 2723 (2014).

[182] H. Wang, and X. Peng, J. Opt. Soc. Am. B **29**, 429 (2005).

[183] L. Zhang, and J. Evers, Phys. Rev. A **89**, 013817 (2014).

[184] D. B.-Arbiv, A. D. W.-Gordon, and H. Friedmann, Phys. Rev. A **63**, 031801(R) (2001).

[185] M. Yan, E. G. Rickey, and Y. Zhu, Phys. Rev. A **64**, 041801(R) (2001).

[186] R. B. Li, L. Deng, and E. W. Hagley, Phys. Rev. Lett. **110**, 113902 (2013).

[187] G. Vemuri, G. S. Agarwal, and B. D. Nageswara Rao, Phys. Rev. A **53**, 2842 (1996).

[188] O. Kocharovskaya, Y. Rostovtsev, and M. O. Scully, Phys. Rev. Lett. **86** 628 (2001).

[189] A. Javan, O. Kocharovskaya, H. Lee, and M. O. Scully, Phys. Rev. A **66**, 013805 (2002).

[190] Y. Peng, Y. Niu, L. Zhang, A. Yang, L. Jiang, and S. Gong, Opt. Lett. **37**, 3333 (2012).

[191] A. D. Bandrauk, H. Shen, Journal of Physics A: Mathematical and General **27**, 7747 (1994).

[192] H. Yoshida, Phys. Lett. **150A**, 162 (1990).

[193] M. Suzuki, Phys. Lett. **146A**, 319 (1990); M. Suzuki, Phys. Lett. **165A**, 387 (1992).

Publications

Journal

1. O. N. Verma, L. Zhang, J. Evers, and T. N. Dey, *Optical cloning of arbitrary images beyond the diffraction limits*, Phys. Rev. A **88**, 013810 (2013).

2. O. N. Verma and T. N. Dey, *Enhancement of image resolution beyond the diffraction-limit by double dark resonances*, Phys. Rev. A **89**, 033830 (2014).

3. O. N. Verma and T. N. Dey, *Steering, Splitting and Cloning of Optical Beam in a Coherently Driven Raman Gain System*, (communicated in Phys. Rev. A).

Vita

Mr. Onkar Nath Verma, born in Uttar Pradesh, India did his B.Sc. with Physics and Mathematics as main subjects in 2007 from Ewing Christian College Allahabad and M.Sc. in Physics in 2009 from Allahabad University, Uttar Pradesh. He joined IIT Guwahati for Ph.D. in 2009. He was awarded Junior Research Fellowship in 2009 and Senior Research Fellowship in 2011 by MHRD, India.